

THE DYNAMICS AND COLD GAS CONTENT OF LUMINOUS INFRARED
GALAXY MERGERS IN THE LOCAL UNIVERSE

George Collins Privon
Eagle, Idaho

B.S., Rochester Institute of Technology, 2006

M.S., University of Virginia, 2009

M.S., Rochester Institute of Technology, 2009

A Dissertation Presented to the Graduate
Faculty of the University of Virginia
in Candidacy for the Degree of
Doctor of Philosophy

Department of Astronomy

University of Virginia
August, 2014

Aaron S. Evans

John E. Hibbard

D. Mark Whittle

Robert Davis

Joshua E. Barnes

©Copyright by
George Collins Privon
All rights reserved
August, 2014

Abstract

Luminous Infrared Galaxies (LIRGs; $10^{11} \leq L_{\text{IR}}[8 - 1000 \mu\text{m}]/L_{\odot} < 10^{12}$) and Ultraluminous Infrared Galaxies (ULIRGS; $L_{\text{IR}}[8 - 1000 \mu\text{m}]/L_{\odot} \geq 10^{12}$) are the most extreme star forming systems in the local universe, both in terms of their absolute star formation rates—ten to several hundred times that of “normal” galaxies—and their star formation rate densities. Many U/LIRGs are interacting or merging disk galaxies undergoing enhanced star formation and/or nuclear activity, likely triggered as the objects transform into massive S0 and elliptical merger remnants. The LIRG population also contains a significant number of apparently isolated disk galaxies which are undergoing enhanced star formation, providing a window on secular galaxy evolution.

This work examines nearby U/LIRGs chosen from the Great Observatories All-sky LIRG Survey (GOALS), an infrared flux and luminosity selected sample. The proximity of these systems enables high spatial resolution study of active galactic nuclei (AGN) and extreme star formation in these objects. New maps of the neutral hydrogen (HI) emission are presented for systems morphologically classified in the optical and mid-infrared as non-merging or pre-merger systems. The results of this study suggests that some infrared-selected galaxies may be minor mergers or interactions which are being viewed so soon after first pass that the stellar disk has not yet been significantly disturbed.

Galaxy mergers appear to drive much of the enhanced activity observed in U/LIRGs; understanding the merger state of these systems provides a context for observations of star formation and AGN properties. In order to constrain the merger stage, dynamical models for a sample of nine systems were matched to the observed kinematics and morphology as obtained from optical imaging and interferometric HI maps. The

resulting models are used not only to constrain the merger stage, but also the encounter geometry of the precursor. Based on these dynamical models a new merger stage classification is presented, which re-scales objects to a common timeline is used to place the observations in context. Applications of this dynamical merger stage to the study of star formation rates and indicators of AGN activity are presented.

Finally, newly obtained measurements of the galaxy-integrated 1–0 rotational transitions of hydrogen cyanide (HCN) and formylium (HCO^+) in a sample of U/LIRGs are used to investigate the ratio of HCN (1–0) to HCO^+ (1–0) and its dependence on mid-infrared indicators of AGN strength. In contrast to previous claims, it is demonstrated that high values of this ratio are not uniquely linked to the presence of an AGN, but can be achieved in systems dominated by star formation. This suggests the excitation of these high critical density molecular gas tracers is determined by the complex interplay of radiation field, gas density, and gas column.

Acknowledgements

I owe a debt of gratitude to many people for their assistance and support over the course of my work on this dissertation. My colleagues in the Astronomy Department at the University of Virginia have provided an excellent working environment while also providing opportunities for simulating formal and informal discussion. The staff at the National Radio Astronomy Observatory maintain a welcoming atmosphere and I have had many pleasant interactions with them.

The staff and telescope operators at the IRAM 30m Radiotelescope, the Westerbork Synthesis Radio Telescope, the Karl G. Jansky Very Large Array, and the Giant Metrewave Radio Telescope provided great support and assistance for observations which are presented in this dissertation.

Larry “Doc Nez” Neznanski was instrumental in my developing a love for physics through my time in high school—my fond memories of physics led to a change of major which put me on the course I now follow. During the final two years of my undergraduate program and my first year of graduate school Stefi Baum, Chris O’Dea, David Axon, and Andy Robinson provided me with excellent advice, guidance, and support. Joe Mazarella, Lee Armus, and Steve Lord hosted me for a 7-month stay at the Infrared Processing and Analysis Center and provided helpful input on many aspects of this dissertation.

During my time as a graduate student, I have been fortunate to have friends who continue to make the journey a fun and memorable one. I enjoyed many conversations with Vivian U on galaxies, radio astronomy, and the best desserts in Waimea. Andre Wong has provided great companionship during various outings in the mountains. I deeply appreciate my friendship with David Whelan, the many conversations we have had on almost every imaginable topic, and our varied outings in the Virginia

countryside and challenging volcano hikes. Michael Eisenbrown has been a great friend, reminding me through our adventures in the mountains that a break can return one to astronomy with a refreshed perspective. Long live the Crack o' Noon Club!

The members of my committee made many helpful suggestions over the past four years of work on this dissertation. Mark Whittle provided much appreciated critical comments on the proposed work which helped me examine the aims and assumptions as I started on this project. John Hibbard's perennial willingness to discuss galaxy evolution anytime I might poke my head in this office resulted in many stimulating and helpful conversations. I benefited greatly from Josh Barnes's hospitality at the Institute for Astronomy and from his instruction on N -body simulations and models of galaxy mergers.

Thank you to Aaron Evans for advising me on this dissertation and through several years of my graduate career. I appreciate both the encouragement and freedom to devise and develop my own projects and scientific ideas.

Finally, and most importantly, thank you to my family for their encouragement and support over the years. Granddadd Chew gave me my start in astronomy, showing me Halley's Comet at the age of two. He, Grandmama, Grandpa, and Grandma have always been supportive of my endeavors. My parents, Chris and Keron, my brothers, Peter and Chris II, and Kelly Hondula have been a constant source of love, support, and encouragement.

Table of contents

Abstract	ii
Acknowledgements	iv
List of Figures	x
List of Tables	xi
1 Introduction	1
1.1 Luminous Infrared Galaxies and the Evolution of Galaxy Mergers . . .	2
1.2 Studying the Effect of Galaxy Interactions	5
1.2.1 The Great Observatories All-sky LIRG Survey	6
1.2.2 Observations of the Cold Interstellar Medium	7
1.2.3 Matched Numerical Simulations	9
1.3 Contributions	10
2 GOALS: A Survey of H I in Luminous Infrared Galaxies	11
2.1 Introduction	11
2.2 Sample Selection	12
2.3 Observations and Data Reduction	13
2.3.1 Observations	13
2.3.2 Data Reduction	20
2.4 Summary	22
3 GOALS: H I Observations of Luminous Infrared Galaxies with Un- perturbed Stellar Morphologies	23
3.1 Introduction	23
3.2 Sample Selection	24
3.3 Results	25
3.3.1 Individual Source Notes	27
3.4 Triggers of Activity in LIRGs	31
3.4.1 On Determinations of the (Minor) Merger Rate	33
3.4.2 Dynamical Modeling	34

3.5	Conclusions	34
4	Dynamical Modeling of Galaxy Mergers using Identikit	41
4.1	Introduction	41
4.2	The Sample and Data	43
4.2.1	NGC 5257/8	46
4.2.2	The Mice	47
4.2.3	Antennae	48
4.2.4	NGC 2623	49
4.3	Matching of Dynamical Models	51
4.3.1	Test Particle Simulations	52
4.3.2	Data Visualization	54
4.3.3	Identikit Matching	55
4.3.4	Verification With Self-Consistent Simulations	57
4.4	Results and Discussion	59
4.4.1	NGC 5257/8	62
4.4.2	The Mice	66
4.4.3	Antennae	69
4.4.4	NGC 2623	73
4.4.5	Future Work	75
4.5	Summary	77
5	Dynamical Modeling of Galaxy Mergers Using Identikit. II: Star Formation, Active Galactic Nuclei, and Merger Stage Classification	84
5.1	Introduction	84
5.2	The Sample and Data	85
5.3	Matching of Dynamical Models	86
5.4	Modeling Results	88
5.4.1	Mrk 273	89
5.4.2	IC 883	90
5.4.3	NGC 3256	93
5.4.4	NGC 34	96
5.4.5	NGC 1614	100
5.4.6	Non-modeled systems	103
5.5	Discussion	105
5.5.1	Merger Stage Classification	105
5.5.2	General Properties of the Encounters	113
5.5.3	Activity as a Function of Merger Stage	116
5.5.4	Comments on the Matching Process	118
5.6	Summary	119

6	The Utility of HCN (1–0) and HCO⁺ (1–0) as tracers of high-density gas in Local Luminous Infrared Galaxies	122
6.1	Introduction	122
6.2	Data	124
6.3	HCN (1–0) as a Tracer of AGN Activity	125
6.3.1	Potential Distance Effects	129
6.4	A SFR – L _{HCN (1-0)} Relation for U/LIRGs	129
6.4.1	Future Observations	131
6.5	Conclusions	133
7	Summary	134
7.1	Galaxy Interactions	134
7.2	Tracers of Dense Gas	136

List of Figures

1.1	Prograde vs. Retrograde Interactions	4
3.1	H I observations of NGC 2388	36
3.2	H I observations of NGC 2322	36
3.3	H I observations of NGC 0317B	37
3.4	H I observations of IRAS05083+2441	37
3.5	H I observations of NGC 3221	38
3.6	H I observations of NGC 6701	39
3.7	H I observations of CGCG 141-034	40
3.8	H I observations of CGCG 142-034	40
4.1	Orbital evolution of NGC 5257/8, The Mice, the Antennae, and NGC 2623	61
4.2	Dynamical model for NGC 5257/8	64
4.3	Simulated morphological evolution of NGC 5257/8	65
4.4	Comparison of the optical morphology of NGC 5257/8 with the dynamical model	79
4.5	Dynamical model for The Mice	80
4.6	Dynamical model for the Antennae	81
4.7	Dynamical model for NGC 2623	82
4.8	Simulated morphological evolution of NGC 2623	83
5.1	Dynamical model for Mrk 273	91
5.2	Simulated morphological evolution for Mrk 273	92
5.3	Dynamical model for IC 883	94
5.4	Simulated morphological evolution for IC 883	95
5.5	Dynamical model for NGC 3256	97
5.6	Simulated morphological evolution for NGC 3256	98
5.7	Preliminary dynamical model for NGC 32	99
5.8	Preliminary dynamical model for NGC 1614	102
5.9	Wide-field morphological and kinematic data for NGC 6240	106
5.10	Orbital evolution of Mrk 273, IC 883, and NGC 3256	107
5.11	Dynamical merger stage classification example	111

5.12	Comparison of morphological and dynamical merger stage classification schemes	114
5.13	Comparison of the modeled nuclear separation with the measured (projected) nuclear separation	114
5.14	Distribution of projected nuclear separations for random viewing directions	117
5.15	sSFR as a function of dynamical merger stage	117
5.16	AGN contribution to the mid-infrared as a function of dynamical merger stage	121
6.1	$L'_{\text{HCO}^+ (1-0)} / L'_{\text{HCO}^+ (1-0)}$ versus $L_{\text{IR}}[8 - 1000 \mu\text{m}]$	126
6.2	$L'_{\text{HCN} (1-0)} / L'_{\text{HCO}^+ (1-0)}$ versus various mid-infrared AGN tracers	128
6.3	$L'_{\text{HCN} (1-0)} / L'_{\text{HCO}^+ (1-0)}$ versus luminosity distance	130
6.4	$L'_{\text{HCN} (1-0)}$ versus L_{IR}	132

List of Tables

2.1	HI Observing Parameters	16
2.2	HI Sample source Properties	17
2.2	HI Sample source Properties	18
2.3	HI Data Cube Properties	19
2.3	HI Data Cube Properties	21
3.1	HI Data Cube Properties for Systems with Undisturbed Stellar Morphologies	26
3.2	Measured HI Properties	28
4.1	Dynamical Modeling Sample Description	45
4.2	Dynamical models derived from Identikit matching	60
4.3	Comparison of dynamical models for the Mice	68
4.4	Comparison of dynamical models for the Antennae	72
5.1	Dynamical Modeling Sample Description, Pt. II	87
5.2	HI Data Used in Modeling	107
5.3	Dynamical models derived from Identikit matching, Pt. II	108
5.4	Merger Stages of Modeled Systems	111

Chapter 1

Introduction

Our Galaxy and the galaxies surrounding us are thought to be built up from the hierarchical agglomeration of smaller galaxies, themselves tracing their ancestry back to the collapse of the first over-densities in the Universe, seeded by the inhomogeneities of quantum fluctuations (e.g., Spergel et al. 2003). This accumulation of material into larger and larger structures occurs in part via interactions between and eventual mergers of galaxies embedded in dark matter halos (Toomre & Toomre 1972; Toomre 1977; Barnes 1992).

While the bulk of the growth of massive galaxies occurred earlier in the life of the Universe (e.g., Cowie et al. 2004; Nelan et al. 2005), vestiges of this hierarchical formation are still visible in the nearby universe, as massive galaxies undergo interactions and mergers. The proximity of nearby massive merging systems provides an excellent opportunity to study the effects of galaxy interactions in great detail. This dissertation focuses on observations and numerical simulations of an infrared-selected sample of local starbursting galaxy systems, many of which are experiencing major mergers (Armus et al. 2009).

1.1 Luminous Infrared Galaxies and the Evolution of Galaxy Mergers

The Infrared Astronomy Satellite (IRAS; Neugebauer et al. 1984), launched in 1983, provided the first unbiased infrared survey of the sky—at 12, 25, 60, and 100 μm —and detected a population of galaxies whose infrared emission dominates their overall energy output (Soifer et al. 1986). At high luminosities, in excess of $10^{11} L_{\odot}$, these infrared-selected systems outnumber optically selected systems. The Ultraluminous Infrared Galaxies (ULIRGs, $L_{\text{IR}}[8 - 1000 \mu m] \geq 10^{12} L_{\odot}$) are observed to be primarily merging or post-merger systems, while the Luminous Infrared Galaxies (LIRGs, $10^{11} \leq L_{\text{IR}}/L_{\odot} < 10^{12}$) are a mix of merging and non-interacting galaxies (Armus et al. 1987). The infrared luminosity of these systems results from the absorption of ultraviolet and optical light emitted by star formation and Active Galactic Nuclei (AGN) by dust grains, followed by the re-radiation of the energy as infrared radiation.

At low-redshifts, U/LIRGs are an interesting phase in galaxy evolution, consisting of galaxies undergoing enhanced and dust-enshrouded star formation. Two and a half decades ago, an evolutionary link was proposed, linking disk galaxies, ULIRGs, Quasars, and elliptical galaxies (Sanders et al. 1988), building on the idea of merger-induced “furnace stoking” proposed by Toomre & Toomre (1972) and the transformation of disk galaxies into ellipticals discussed by Toomre (1977). In this scenario, pairs of disk galaxies undergo interactions and mergers caused by their mutual gravitation attraction overcoming the expansion of the Universe. Gravitational torques driven by the interaction cause gas to lose angular momentum, fueling a nuclear starburst and accretion onto the supermassive black hole(s) (SMBHs; Toomre & Toomre 1972; Barnes & Hernquist 1991; Mihos & Hernquist 1994b; Barnes & Hernquist 1996;

Hopkins & Quataert 2010). Both the enhanced star formation and SMBH activity contribute to the significant infrared luminosity observed in these systems. As this nuclear activity progresses, feedback from the star formation and/or AGN activity removes the gas via outflows (e.g., Haehnelt et al. 1998; Silk & Rees 1998; Di Matteo et al. 2005; Rupke & Veilleux 2011), self-regulating the nuclear activity. This feedback can also remove the material obscuring the accreting SMBH, giving rise to an optically visible quasar (Sanders et al. 1988; Hopkins et al. 2008). Once the encounter has progressed to the point of the nuclei merging, the systems undergo (partial) violent relaxation, potentially transforming the system into an elliptical galaxy (Barnes 1992) if nuclear star formation boosts the central phase space density (Kormendy & Sanders 1992). The next phase of evolution is calmer; the tidal materials raised off the disk eventually apocenter and fall back onto the merger remnant (e.g., Hibbard & Mihos 1995), fueling low levels of star formation. Absent a new source of gas to support further star formation, such as accretion from the intergalactic medium, the stellar population ages and the system completes its transformation to a red elliptical or lenticular galaxy.

In a galaxy interaction, the encounter geometry of disk galaxies is broadly separated in two configurations, defined by the relative alignment of the angular momentum vector of the disk and the orbital angular momentum vector of the two galaxies: galaxies with their disk angular momentum vector aligned with that of the orbit are said to be undergoing a prograde interaction, while those whose disk angular momentum is anti-aligned with the orbital angular momentum vector experience retrograde interactions. This distinction is important because galaxies respond differently to prograde and retrograde interactions (e.g., Figure 1.1; Toomre & Toomre 1972). The encounter geometry of a disk is generally specified using the angle, i , between the disk

angular momentum vector and the orbital angular momentum vector, where $i = 0^\circ$ is a perfectly prograde interaction and $i = 180^\circ$ is a perfectly retrograde encounter.

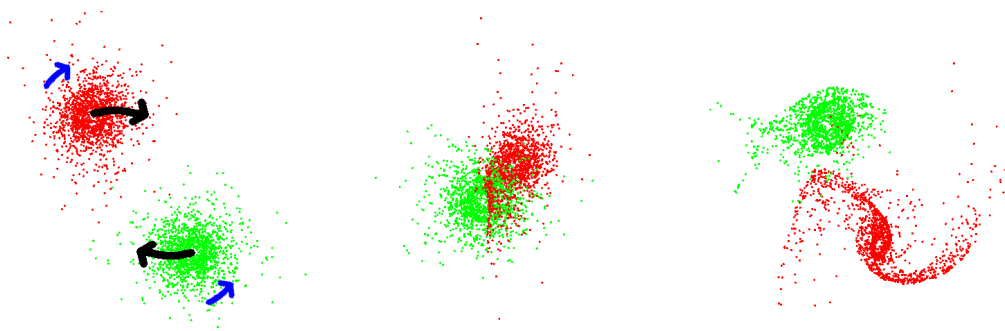


Fig. 1.1.— Demonstration of the tidal response of a galaxy disk and the dependence on the alignment between the disk angular momentum and the orbital angular momentum. In this figure the red points are a disk experiencing a perfectly prograde interaction ($i = 0^\circ$) and the green points are a disk experiencing a perfectly retrograde interaction ($i = 180^\circ$). The left panel shows the two galaxies 0.5 time units before their first pericentric passage. The black arrows mark the rough orbital motion of the two galaxies (the orbital angular momentum vector is pointing into the page), and the blue arrows mark the rotation of the individual galaxies. The center panel shows the two galaxies at their pericentric passage (approximately 3 disk scale lengths) and the right panel shows the two galaxies 0.5 time units after their close pass. Note the prominent tidal tail and bridge associated with the prograde galaxy compared to the more subtle response of the retrograde galaxy.

The difference in response between prograde and retrograde encounters is due to the duration of the tidal force experienced by a star over the course of the interaction. In a prograde encounter, the disk rotation causes stars on the near and far sides of the disk to remain in regions of high tidal field strengths for an extended period of time, resulting in a relatively strong, quasi-resonant interaction (Toomre & Toomre 1972; D’Onghia et al. 2010). More precisely, this quasi-resonance occurs when the disk spin frequency is comparable to the orbital frequency of the companion galaxy. This gives rise to the prominent tidal tails and bridges seen in many merging systems (e.g., The Mice and the Antennae; Vorontsov-Vel’Iaminov 1958; Duncan 1923). In

retrograde encounters, the rotation of the disk results in stars spending significantly less time in regions where they experience strong tidal forces, reducing the resulting effect on a galaxy.

1.2 Studying the Effect of Galaxy Interactions

Interactions provide an excellent laboratory for understanding galaxy formation and evolution. The extreme star formation observed in these systems enables tests of star formation models at high densities and radiation fields. These star formation rates cause a rapid build-up in the stellar mass of galaxies making these systems ideal for studying the origin and maintenance of the observed correlations between SMBH mass and the host galaxy properties (e.g., Ferrarese & Merritt 2000; Gebhardt et al. 2000; Gültekin et al. 2009). Finally, the growth and influence of the SMBH black hole can be studied via diagnostics of the AGN activity (e.g., Kim et al. 1995; Iwasawa et al. 2011; Petric et al. 2011; Stierwalt et al. 2013) and observations of outflows (e.g., Armus et al. 1987; Rupke & Veilleux 2011; Mazzarella et al. 2012; Aalto et al. 2012; Westmoquette et al. 2012; Rupke & Veilleux 2013; González-Alfonso et al. 2014; Hill & Zakamska 2014).

This dissertation pursues the question of merger-driven star formation activity by presenting both observations and numerical simulations of ongoing mergers in the local universe. The samples of galaxies in this dissertation are drawn from the Great Observatories All-sky LIRG Survey (GOALS; Armus et al. 2009, ; further described in Sec 1.2.1); GOALS is a complete sample of IRAS-detected galaxies with infrared luminosities $L_{\text{IR}}[8 - 1000 \mu\text{m}], \geq 10^{11} L_{\odot}$ and $60 \mu\text{m}$ flux density $F_{60\mu\text{m}}, > 5.24 \text{ Jy}$. The observations presented here are focused on the neutral atomic and cold molecular ISM (Sec 1.2.2); neutral hydrogen 21 cm observations (HI) are used to probe the

morphology and kinematics of a sample of U/LIRGs while observations of rotational transitions of the molecules HCN and HCO⁺ are used to probe the excitation of the dense ($n > 10^3 \text{ cm}^{-3}$) molecular gas. The numerical work in this dissertation centers on understanding the global evolution of individual systems by matching dynamical models to the ongoing mergers being experienced by each system (Section 1.2.3).

1.2.1 The Great Observatories All-sky LIRG Survey

The dust reprocessing which accounts for the prodigious infrared luminosity of U/LIRGS also obscures our view of the activity at ultraviolet and optical wavelengths—studying the extreme activity in these systems requires a multi-wavelength approach. The Great Observatories All-sky LIRG Survey (GOALS; Armus et al. 2009) is a complete sample of U/LIRGs in the Revised Bright Galaxy Survey (RBGS; Sanders et al. 2003). The 202 systems included span a range of interaction types and stages, from early-stage interactions to post-merger systems; some apparently non-interacting systems are also contained in the sample (e.g., Stierwalt et al. 2013). These systems include the observed range of optical nuclear diagnostic classifications, including star formation dominated, AGN dominated, and LINER systems (e.g., Kim et al. 1995).

GOALS consists of dedicated multi-wavelength observing campaigns with the NASA Great Observatories (the Hubble Space Telescope, Spitzer Space Telescope, Galaxy Evolution Explorer, and the Chandra X-ray Observatory) and various ground-based facilities. These observations include continuum observations from radio through X-ray frequencies, as well as spectral line observations of important tracers of the atomic, molecular, and ionized interstellar medium (ISM). In addition to constraining the amount, distribution, and conditions of the ISM, these observations also provide information about the level and influence of star formation and AGN in

these systems.

With two exceptions, the galaxies in this dissertation are drawn from the GOALS sample. The particular choice of objects is described in the individual Chapters. Where relevant, existing multi-wavelength data from GOALS was incorporated into the analysis.

1.2.2 Observations of the Cold Interstellar Medium

Neutral Hydrogen

Hydrogen is the most abundant element in the Universe and is the fuel for the fusion powering main sequence stars (Bethe 1939). The distribution and amount of HI in galaxies provides important information on the dynamics of both quiescent (e.g., Roberts 1976; Rubin et al. 1978; Martinsson et al. 2013) and merging galaxies (e.g., van der Hulst 1979; Hibbard & van Gorkom 1996; Hibbard & Yun 1999) as well as the distribution of the neutral atomic ISM (e.g., Bosma 1981). HI is often extended beyond the optical radius of galaxies, making it a sensitive probe of interactions between galaxies (Yun et al. 1994).

This dissertation includes a survey of the HI emission in a subset of the systems from GOALS, conducted to map the distribution of HI and obtain large-scale kinematic information. The focus in Chapter 3 is to use these observations to search for evidence of ongoing interactions in GOALS LIRGs which do not appear to be undergoing a major merger and to study LIRG pairs identified as pre-interaction to see if their extended HI shows evidence for interaction. Previously obtained HI observations of ongoing mergers are also used to constrain dynamical models of their encounters (Section 1.2.3, Chapters 4 and 5).

Putative Tracers of High-Density Molecular Gas

There is overwhelming evidence that stars form in and from clouds of molecular hydrogen (e.g., Bigiel et al. 2008). Star formation occurs in the inner regions of clouds, where densities can exceed 10^8 cm^{-3} . The carbon monoxide (CO) molecule has long been used to trace the molecular interstellar medium of galaxies, including in the U/LIRG population (e.g., Sanders & Mirabel 1985; Tinney et al. 1990). With a relatively low critical density ($\approx 2 \times 10^3 \text{ cm}^{-3}$), the lowest rotational transition, CO (1–0), traces the bulk of the molecular gas, including gas which is not directly forming new stars. The rotational transitions of the HCN and HCO⁺ molecules—which have significantly higher critical densities than CO—appear to be more linearly correlated with the star formation rates (as inferred from L_{IR} ; Gao & Solomon 2004).

However, the emission from HCN can be affected by a number of factors, including infrared pumping (Aalto et al. 1995), high densities and columns (Meijerink et al. 2007), and an incident X-ray flux (Lepp & Dalgarno 1996). These phenomena, all of which are likely to be present in U/LIRGs, can influence the emission from HCN and HCO⁺, limiting their utility as tracers of dense gas. Several previous studies have claimed a link between AGN and enhanced HCN (1–0) and HCN (4–3) emission (e.g., Graciá-Carpio et al. 2006; Kohno et al. 2003; Imanishi et al. 2006), and have suggested that HCN cannot be used to directly trace star formation and the dense gas associated with it.

In Chapter 6, a study of the galaxy-integrated HCN (1–0) and HCO⁺ (1–0) emission in a sample of U/LIRGs is presented, comparing the emission in these rotational transitions with the star formation and AGN properties derived from mid-infrared observations. This attempt to understand the origin of the emission of these putative high-density tracers is important for studies attempting to ascertain the properties

of the cold, dense phase of the ISM. With an understanding of the excitation of these transitions, these observations can be used as constraints on models of galaxy evolution—a successful model should reproduce the properties of the ISM, in addition to the observed star formation properties.

1.2.3 Matched Numerical Simulations

Much of the understanding of merger-driven activity has come from qualitative comparisons between simulations and observations, which has resulted in a robust paradigm for galaxy evolution. However, the details are still uncertain, particularly regarding star formation on galaxy scales. One path towards progress is to make detailed comparisons between simulations and observations, and thus provide constraints on the models by requiring they successfully match the observations.

Galaxy mergers offer a unique opportunity to perform this detailed comparison: the dynamical interaction can trigger higher star formation rates in a more compact volume. This enables a test of star formation models in more extreme conditions. Individual galaxy mergers can be modeled to “age date” and obtain the initial encounter parameters for the system (e.g., Toomre & Toomre 1972; Hibbard & Mihos 1995). Using the derived merger stage, observations can be placed in the context of the ongoing dynamical activity, elucidating the modulation of star formation and AGN by the ongoing merger. Knowledge of the encounter parameters of each merger can be used to run detailed hydrodynamic simulations matched to that system; these simulations can be used to test star formation models by comparing the simulation predictions with the detailed observations of that system (e.g., Barnes 2004; Karl et al. 2013).

The recent development of the Identikit modeling tool (Barnes & Hibbard 2009;

Barnes 2011) has enabled, for the first time, relatively rapid matching of dynamical models to the observed kinematics and morphology of ongoing mergers. This enables the detailed comparison of models and simulations to move beyond studies of single systems, enabling a statistically meaningful test of galaxy evolution models. In Chapters 4 and 5, dynamical models are matched to the morphology and kinematics of nine systems to obtain their encounter parameters and time since first encounter. The results of this modeling are used in conjunction with a newly developed dynamical merger stage classification to put observations on a rigorously determined merger timeline.

1.3 Contributions

The work presented here was performed primarily by the author, but others made valuable contributions, without which this project could not have succeeded. In particular, Chapters 4 and 5 benefited from data provided by J. Hibbard. J. Barnes generously provided tutelage in the use of the Identikit modeling tool and the Zeno simulation environment. The two aforementioned collaborators also provided very useful feedback on and suggestions for in-progress dynamical models. Chapter 4 has appeared in the *Astrophysical Journal*, and the co-authors listed at the start of the Chapter all provided helpful feedback on the manuscript. François Schweizer provided helpful comments on a draft version of Chapter 4. Many of the HI observations in Chapter 3 were scheduled and performed by the staff at ASTRON (Netherlands Institute for Radio Astronomy). The millimeter observations presented in Chapter 6 were performed by the author, Aaron Evans, Kazushi Iwasawa, and Rubén Herrero-Illana.

Chapter 2

GOALS: A Survey of H I in Luminous Infrared Galaxies

2.1 Introduction

Neutral hydrogen (H I, $\nu_{rest} = 1420.40575177$ MHz) is a major component of late-type galaxies, accounting for 5-40% of a galaxy's baryonic mass, depending on its type and stellar mass (e.g., Catinella et al. 2010). While H₂ is most directly linked to the ongoing star formation (e.g., Bigiel et al. 2008; Leroy et al. 2012), H I is the ultimate reservoir of fuel for star formation. Measurements of the total H I mass then provide an estimate (modulo accretion from the circum-galactic medium) of the mass available to eventually form new stars.

H I observations of isolated or non-interacting galaxies show that many systems have gas disks which extend significantly beyond the stellar disks (e.g., Bosma 1981), making H I a sensitive probe of tidal interactions (e.g., Yun et al. 1994). Additionally, H I observations provide kinematic information out to large distances, thus allowing the dynamics of disk galaxies and their halo properties (e.g., Martinsson et al. 2013)

or their interaction history to be constrained (e.g., Hibbard & van Gorkom 1996).

U/LIRGs are observed to be primarily interacting or ongoing mergers of pairs of gas rich galaxies. HI mapping observations of U/LIRGs, for which there is relatively little data published to date, can provide high velocity resolution kinematic information for tidal features, which can be matched with dynamical models and used to constrain the orbits and initial encounter geometry of each system (e.g., van der Hulst 1979; Mihos et al. 1993; Gilbert & Sellwood 1994; Hibbard & Mihos 1995; Barnes 2004; Barnes & Hibbard 2009; Barnes 2011; Karl et al. 2010; Privon et al. 2013, Chapters 4 and 5). Systems with elevated star formation rates that have unperturbed stellar morphologies, may bear the signature of an early stage encounter or flyby interactions and minor mergers in their HI kinematics and/or morphology. These observations may then discriminate between scenarios where elevated star formation rates in apparently isolated galaxies are the product of secular evolution versus galaxy-galaxy interactions (Chapter 3).

This Chapter summarizes a HI survey of 44 U/LIRGs. The sample is described in Section 2.2, followed by a discussion of the observations and data reduction in Section 2.3. Where appropriate and unless otherwise noted, computed values assume the WMAP-3 cosmology: $H_0=73 \text{ km s}^{-1} \text{ Mpc}^{-1}$, $\Omega_\Lambda = 0.73$, and $\Omega_m = 0.27$ (Spergel et al. 2007).

2.2 Sample Selection

A sample of 44 U/LIRGs was selected from the Great Observatories All-Sky LIRG Survey (GOALS; Armus et al. 2009). GOALS is a flux and luminosity limited subset of the IRAS revised bright galaxy sample (Sanders et al. 2003), selected on the basis of IRAS observations to have $F_{60 \mu m} > 5.24 \text{ Jy}$ and to have $L_{\text{IR}} [8\text{--}1000 \mu m]$

$\geq 10^{11} L_{\odot}$. This sample contains the most vigorously star forming systems in the local universe—their proximity enables the study of this phenomenon at high spatial resolution. The majority of the sources lie within a declination range of $> +20^{\circ}$ and are within 100 Mpc. The distance criteria ensures the best possible chance of detected extended HI tidal emission associated with merging galaxies. The declination cut was made to ensure reasonable synthesized beam sizes in the North–South direction for observations made with the East–West Westerbork Synthesis Radio Telescope array. For sources close to the celestial equator, an East–West array samples Fourier space in primarily one direction, resulting in poor angular resolution in the orthogonal direction; the declination cut ensures reasonable North–South resolution in the final observations.

2.3 Observations and Data Reduction

In this Section, we summarize the observations on each telescope and describe the general setup for each system. Observational parameters are listed in Table 2.1. Additionally, we outline the steps taken to calibrate and image the raw data.

2.3.1 Observations

Observations of 44 sources (Table 2.2) were carried out with the Very Large Array¹ (VLA; in both pre-WIDAR and WIDAR Open Share Risk Observing (OSRO) phases), the Westerbork Synthesis Radio Telescope² (WSRT), and the Giant Metrewave Radio Telescope (GMRT) in dedicated projects to map the HI emission in a

¹The National Radio Astronomy Observatory is a facility of the National Science Foundation operated under cooperative agreement by Associated Universities, Inc.

²The Westerbork Synthesis Radio Telescope is operated by the ASTRON (Netherlands Institute for Radio Astronomy) with support from the Netherlands Foundation for Scientific Research (NWO).

sample of U/LIRGs. We briefly describe observations done with the specific arrays below.

Very Large Array

Prior to the WIDAR upgrade, a sample of U/LIRGs was observed in the VLA's C- and D-array configurations, with the data from both configurations combined during imaging. Bandwidths were typically 8 MHz with 64 channels. Following the upgrade to the WIDAR correlator, observations were obtained in OSRO mode for EVLA observations (Project codes AP580 and 10B-203). An 8 MHz bandwidth was used with 256 channels. Observing blocks were started and completed with observations of a bright flux calibrator (3C 48, 3C 147, or 3C 286). Observations of a bandpass calibrator and phase calibrator were performed periodically to track changes to the system and atmosphere, though the latter generally has minimal effect at 1.4 GHz. Most systems were observed in the C-array configuration, while some were also observed in D-array for better recovery of extended flux.

Westerbork Synthesis Radio Telescope

WSRT observations (Project codes R10A/009, R11A/012, and R11B/011) were performed using a 20 MHz bandwidth and 1024 channels, resulting in a native channel width of 19.5 kHz. The flux calibrator observed at the start of each run was also used for phase and bandpass calibrations. No other phase calibration observations were performed. If necessary, phase solutions are obtained using self-calibration on line-free channels. Observations were performed in sessions of up to 12h, to ensure good imaging fidelity by maximizing the sampling of spatial frequencies. The more distant sources were observed in 2x12h tracks in order to obtain better sensitivity.

The WSRT “maxi-short” configuration was used, without the antenna RT5, which was unavailable due to instrument development and testing.

Giant Metrewave Radio Telescope

GMRT observations (Project code 18_011) were undertaken using the GMRT Software Backend (GSB) correlator. A 16 MHz bandwidth was used with with 512 channels, resulting in a channel width of 31.25 kHz or 6.6 km s^{-1} at 1420 MHz. In addition to observations of a flux calibrator at the start and end of each session, a phase calibrator near the target was observed every 30-40 minutes to track variations in phase introduced by the system electronics.

Table 2.1. H I Observing Parameters

Telescope	BW (MHz)	N_{chan}	Ch. Width (kHz)
Very Large Array (pre-WIDAR)	8	64	125
Very Large Array (WIDAR)	16	256	62.5
Westerbork Synthesis Radio Telescope	20	1024	19.5
Giant Meterwave Radio Telescope	16	512	31.25

Note. — General configuration information for the H I observations, including the bandwidth, number of channels, and raw channel width.

Table 2.2. HI Sample source Properties

Object	RA	Dec	$\log(L_{\text{IR}}/L_{\odot})$	Merger Stage
Arp 220	15:34:57.3	+23:30:11.7	12.21	d
Mrk 273	13:44:42.2	+55:53:13.2	12.14	d
IRASF23365+3604	23:39:01.3	+36:21:10.2	12.13	d
II Zw 096	20:57:24.0	+17:07:35.1	11.87	c
NGC 6240	16:52:58.9	+02:24:03.7	11.85	d
IRAS21101+5810	21:11:29.3	+58:23:07.6	11.75	c
VV 114	01:07:47.6	-17:30:25.4	11.71	c
IC 883	13:20:35.4	+34:08:22.1	11.67	d
NGC 695	01:51:14.2	+22:34:56.4	11.63	N
NGC 1614	04:33:59.8	-08:34:43.1	11.60	d
IRAS05223+1908	05:25:16.7	+19:10:48.0	11.59	N
II Zw 035	01:44:30.5	+17:06:08.7	11.56	a
NGC 2623	08:38:24.1	+25:45:17.4	11.54	d
IC 5298	23:16:00.7	+25:33:24.4	11.54	N
Mrk 266	13:38:17.7	+48:16:32.9	11.49	b
ESO 507-G070	13:02:52.4	-23:55:18.3	11.49	d
MCG+12-02-001	00:54:03.9	+73:05:06.0	11.44	c
Mrk331	23:51:26.7	+20:35:10.1	11.41	a
MCG+08-11-002	05:40:43.7	+49:41:41.3	11.41	d
NGC7771	23:51:04.0	+20:09:02.0	11.34	N/c/a ^a
NGC0828	02:10:09.5	+39:11:24.6	11.31	d
UGC3608	06:57:34.4	+46:24:10.7	11.30	b
UGC12150	22:41:12.2	+34:14:56.9	11.29	N
IRASF03217+4022	03:25:05.4	+40:33:32.3	11.28	d
NGC2342	07:09:18.1	+20:38:09.5	11.25	a
NGC2388	07:28:53.4	+33:49:08.9	11.23	a
IRAS05083+2441	05:11:25.9	+24:45:18.0	11.21	N

Table 2.2—Continued

Object	RA	Dec	$\log(L_{\text{IR}}/L_{\odot})$	Merger Stage
UGC3351	05:45:48.2	+58:42:03.1	11.22	a
ESO 557-G002	06:31:45.7	-17:38:44.8	11.19	a
IC860	13:15:03.5	+24:37:08.0	11.17	N
CGCG141-034	17:56:56.6	+24:01:01.8	11.13	N
CGCG142-034	18:16:33.8	+22:06:38.9	11.11	a
IRASF02437+2122	02:46:39.1	+21:35:10.1	11.11	c
NGC0317B	00:57:40.4	+43:47:32.1	11.11	a
IRAS04271+3849	04:30:33.1	+38:55:48.0	11.06	d
MCG+04-48-002	20:28:35.1	+25:44:00.2	11.06	a
IRAS08339+6517	08:38:23.2	+65:07:14.5	11.05	N
NGC6701	18:43:12.5	+60:39:11.9	11.05	N
UGC11041	17:54:51.9	+34:46:34.0	11.04	N
UGC3410	06:13:58.8	+80:28:35.2	11.04	a
NGC1961	05:42:04.7	+69:22:43.1	11.02	d
NGC6052	16:05:13.1	+20:32:35.6	11.02	c
NGC7752/3	13:58:33.6	+37:27:13.2	11.01	b
NGC 3221	10:22:20.3	+21:34:22.1	11.00	N

^aThe individual sources W, S, and N, were assigned merger stages of N, c, and a, respectively.

Note. — Col 2 – $L_{\text{IR}}[8 - 1000 \mu\text{m}]$ is taken from Sanders et al. (2003), where the Mould et al. (2000) attractor model was used with $H_0 = 75 \text{ km s}^{-1} \text{ Mpc}^{-1}$, $\Omega_M = 0.3$, and $\Omega_\Lambda = 0.7$. Col 3 – The merger stage is taken from Stierwalt et al. (2013) and is based on visual inspection of IRAC $3.6 \mu\text{m}$ imaging. From their Section 2.5: “ ‘N’ for non-mergers (no sign of merger activity or massive neighbors), ‘a’ for pre-mergers (galaxy pairs prior to a first encounter), ‘b’ for early-stage mergers (post-first-encounter with galaxy disks still symmetric and in tact but with signs of tidal tails), ‘c’ for mid-stage mergers (showing amorphous disks, tidal tails, and other signs of merger activity), or ‘d’ for late-stage mergers (two nuclei in a common envelope)”.

Table 2.3. HI Data Cube Properties

Object	Final RMS mJy beam ⁻¹ ch ⁻¹	Beam (arcsec [, ° PA])
Very Large Array		
II Zw 096	0.36	17.34
Arp 220	0.22	19.57 × 18.41, 74.77
IC 883	0.41	16.99 × 15.81, -62.58
Mrk 273	0.22	16.06 × 14.29, 68.81
NGC 1614	0.48	15.00 × 10.00, -83.00
NGC 2623	0.34	16.13 × 15.34, -3.60
VV 114	0.46	21.05 × 16.74, 1.14
NGC 6240	0.27	21.66 × 20.53, 24.76
NGC 3221	2.0	25.06 × 16.91, -66.17
Mrk 266	1.0	23.85 × 17.54, 89.63
IC 5298	0.021	21.34 × 18.24, 59.38
NGC 695	0.42	19.82 × 17.42, 16.55
Westerbork Synthesis Radio Telescope		
CGCG141-034	0.31	55.83 × 19.34, -175.16
CGCG142-034	0.88	56.29 × 21.21, -0.03
IC860	26	63.17 × 19.13, -172.07
IIIZw035
IRAS04271+3849	0.7	36.05 × 21.65, -0.13
IRAS05083+2441	0.73	51.33 × 21.11, -0.81
IRAS05223+1908	1.6	88.04 × 20.17, 164.70
IRAS08339+6517	2.9	24.01 × 22.39, -0.13
IRAS21101+5810	1.4	24.92 × 22.13, 0.08
IRASF02437+2122	1.8	55.69 × 17.96, -179.85
IRASF03217+4022	1.5	36.05 × 19.80, -175.96
IRASF23365+3604	3.1	36.86 × 24.87, -8.42

2.3.2 Data Reduction

The data were calibrated with the Common Astronomy Software Application (CASA; McMullin et al. 2007) using standard techniques (Taylor et al. 1999). The process was done as uniformly as possible across the instruments. After an initial flagging of shadowed antennas and the bandpass edges, the data were manually inspected for radio frequency interference in both the time and frequency domains. After excising RFI-affected data, the flux-density scale was set for the flux calibrator used in each observation. Next the bandpass was calibrated, using either the primary calibrator or a bandpass calibrator. For WSRT observations, a phase calibration was obtained for the primary calibrator and applied to the target visibilities. For VLA and GMRT observations, the flux scale from the primary calibrator and bandpass were transferred to the phase calibrator and solutions were then obtained for the phase calibrator on a per scan basis. These phase solutions were then transferred to the target visibilities.

After calibration, the data were reinspected for low-level issues and flagged if necessary. If data were flagged on the calibrator observations, the calibrations were repeated. If bright off-axis sources caused artifacts near the sources of interest—most commonly in the WSRT observations due to the regular spacing of dishes in the “maxi-short” configuration—the data were “peeled” (e.g., Noordam 2004) in the following manner: the phase center was shifted to the location of the offending source. An image was cleaned in order to create a model of the off-axis source and the modeled visibilities were then subtracted from the dataset. Finally, the phase center was shifted back to the original phase center. For observations with multiple off-axis sources, this process was repeated for each individual source. Generally, the contamination was significantly reduced, but it could not be completely removed in some cases and artifacts from this are visible in the images.

Table 2.3—Continued

Object	Final RMS mJy beam ⁻¹ ch ⁻¹	Beam (arcsec [, ° PA])
MCG+04-48-002	1.3	49.29 × 20.84, -0.03
MCG+08-11-002	1.3	43.48 × 19.65, -28.04
MCG+12-02-001	0.9	26.77 × 18.89, 11.14
Mrk331	0.19	79.29 × 18.57, 1.12
NGC0317B	0.15	32.48 × 22.58, -0.02
NGC0828	0.36	34.25 × 22.42, -0.04
NGC1961	0.76	23.87 × 22.78, -0.19
NGC2342	0.77	59.22 × 21.01, -0.16
NGC2388	0.44	42.37 × 23.43, -0.02
NGC6052	2.8	59.11 × 22.63, -179.95
NGC6701	0.86	24.51 × 22.19, 0.13
NGC7752/3	0.75	45.98 × 21.02, -180
NGC7771	1.8	66.27 × 18.67, 2.94
UGC11041	1.88	49.37 × 21.51, 1.08
UGC12150	1.1	40.51 × 21.35, -0.08
UGC3351	0.8	27.17 × 21.28, -0.07
UGC3410	1.5	22.36 × 22.18, -0.41
UGC3608	1.2	30.95 × 22.09, -2.67
Giant Metrewave Radio Telescope		
ESO 557-G002
ESO 507-G070	1.2	7.97 × 6.3, 30.40

Note. — Properties of the image cubes from these observations. Systems without listed cube properties were observed but were not imaged. See text for details. Col 1 – object name, Col 2 – RMS of the cube, Col 3 – Size of the synthesized Gaussian beam. Sources without tabulated values were observed but not imaged due to corrupted data.

2.4 Summary

This H I survey of U/LIRGs is the largest such survey yet undertaken. These observations will be used to study the large-scale distribution and kinematics of the neutral atomic medium in interacting systems. As a demonstration, in Chapter 3 a subset of these observations are used to study the origin of the enhanced star formation in LIRGs which have unperturbed stellar morphologies as determined from their mid-infrared morphology.

Acknowledgements

G.C.P. was supported by NSF grants AST 1109475 and 02-06262, and by a Visiting Graduate Research Fellowship at the Infrared Processing and Analysis Center / Caltech. This work was supported in part by National Science Foundation Grant No. PHYS-1066293 and the hospitality of the Aspen Center for Physics.

The author thanks the staff at ASTRON/WSRT for assistance in planning and carrying out the WSRT observations, and the staff of the GMRT who have made the GMRT observations possible. GMRT is run by the National Centre for Radio Astrophysics of the Tata Institute of Fundamental Research.

Chapter 3

GOALS: H I Observations of Luminous Infrared Galaxies with Unperturbed Stellar Morphologies

3.1 Introduction

H I observations of isolated or non-interacting galaxies show that many systems have gas disks which extend significantly beyond the stellar disks (e.g., Bosma 1981), making H I a sensitive probe of tidal interactions (e.g., Yun et al. 1994). Additionally, H I observations provide kinematic information out to large distances, thus allowing the dynamics of disk galaxies and their halo properties (e.g., Martinsson et al. 2013) or their interaction history to be constrained (e.g., Hibbard & van Gorkom 1996).

Infrared-selected galaxies are known to have enhanced star formation rates (e.g., Soifer et al. 1986). While many of these systems are clearly interacting systems (e.g., Armus et al. 1987), many show no obvious signs of interaction in their stellar morphologies (Armus et al. 1987; Stierwalt et al. 2013). Is the origin of the activity

in these systems due to early-stage interactions which have not yet influenced the stellar distribution or have secular processes led to an increase in the star formation of these systems?

This study is focused on interferometric H I observations of a sample of eight Luminous Infrared Galaxies (LIRGs; $L_{\text{IR}}[8-1000 \mu\text{m}] \geq 10^{11} L_{\odot}$) which have unperturbed stellar morphologies, i.e., they show no optical or mid-infrared evidence of being involved in an ongoing major merger event (Stierwalt et al. 2013). These objects are drawn from the larger study of 44 U/LIRGs described in Chapter 2.

The sample and data reduction are described in Section 3.2, then the results of this H I survey are shown in Section 3.3, followed by a discussion on the implications of the observed H I properties of systems classified by their optical or mid-infrared morphology as not (yet) being involved in a major merger in Section 3.4. Where appropriate and unless otherwise noted, computed values assume the WMAP-3 cosmology: $H_0=73 \text{ km s}^{-1} \text{ Mpc}^{-1}$, $\Omega_{\Lambda} = 0.73$, and $\Omega_m = 0.27$ (Spergel et al. 2007).

3.2 Sample Selection

These eight LIRGs are taken from the larger sample of 44 U/LIRGs from the Great Observatories All-Sky LIRG Survey (GOALS; Armus et al. 2009), described in Chapter 2. GOALS is a flux and luminosity limited subset of the IRAS revised bright galaxy sample (Sanders et al. 2003), selected on the basis of IRAS observations to have $F_{60 \mu\text{m}} > 5.24 \text{ Jy}$ and to have $L_{\text{IR}} [8-1000 \mu\text{m}] \geq 10^{11} L_{\odot}$. The eight sources were selected on the basis of having mid-infrared morphologies consistent with an unperturbed stellar disk. These H I observations are used to search for evidence of galaxy interactions as a trigger for the enhanced star formation occurring in these systems. The observations and data reduction are described in Chapter 2 and Table

3.1 summarizes the data cubes used for this study.

In order to isolate the HI emission, the continuum emission was determined from the line-free channels and subtracted from the data in the visibilities plane. The calibrated and continuum-subtracted data were deconvolved using the CLEAN algorithm and imaged using natural weighting to optimize sensitivity. Total intensity and intensity-weighted velocity maps were created from the resulting data cubes. Total intensity maps were made using pixels with values $> 2\sigma$ in the cube, while velocity field maps were created by masking out regions which were $< 2\sigma$ in the total intensity map. The total intensity map were computed using:

$$M_{intensity}(x, y) = \Delta v \sum_k^N S_\nu(x, y, \nu_k) \quad (3.1)$$

While the intensity-weighted velocity field was computed using:

$$M_v(x, y) = \frac{\sum_k^N v_k S_\nu(x, y, \nu_k)}{\sum_k^N S_\nu(x, y, \nu_k)}, \quad (3.2)$$

where the value for a pixel location (x, y) is computed over N frequency channels, using the flux density (S_ν), the channel velocity (v_k), the channel frequency (ν_k), and the velocity width of a channel (Δv).

Final properties of the data sets for each object are given in Table 2.3. Systems without values listed were not imaged due to corrupted data.

3.3 Results

Table 3.2 is a compilation of the measured HI masses and other galaxy properties, for the eight systems in our sample. The total flux was measured from integrated

Table 3.1. HI Data Cube Properties for Systems with Undisturbed Stellar Mophologies

Object	Final RMS mJy beam ⁻¹ ch ⁻¹	Beam (arcsec [, ° PA])
CGCG 141-034	0.31	55.83 × 19.34, -175.16
CGCG 142-034	0.88	56.29 × 21.21, -0.03
IRAS 05083+2441	0.73	51.33 × 21.11, -0.81
NGC 0317B	0.15	32.48 × 22.58, -0.02
NGC 2342	0.77	59.22 × 21.01, -0.16
NGC 2388	0.44	42.37 × 23.43, -0.02
NGC 3221	2.0	25.06 × 16.91, -66.17
NGC 6701	0.86	24.51 × 22.19, 0.13

Note. — Properties of the image cubes from these observations. Systems without listed cube properties were observed but were not imaged. See text for details. Col 1 – object name, Col 2 – RMS of the cube, Col 3 – Size of the synthesized Gaussian beam. Sources without tabulated values were observed but not imaged due to corrupted data.

intensity maps and HI masses were computed using the flux density (S_ν) measured from the total intensity map, the velocity width of a channel (Δv), the luminosity distance (D_L) and the standard formula (Roberts & Haynes 1994):

$$\frac{M_{HI}}{M_\odot} = 2.36 \times 10^5 \left(\frac{D_L}{\text{Mpc}} \right)^2 \sum \frac{S(\nu)}{\text{Jy}} \frac{\Delta v}{\text{km s}^{-1}}. \quad (3.3)$$

3.3.1 Individual Source Notes

For the remainder of this paper, we focus on the eight systems classified by Stierwalt et al. (2013) as non-interacting or pre-interaction for which we have good observations.

NGC 2388 This system, appearing to be relatively undisturbed in the optical, shows obvious tidal features in HI emission, including two tails and bridge material (Figure 3.1). The HI morphology and kinematics are consistent with an early stage, ongoing prograde–prograde tidal interaction between NGC 2388 and NGC 2389. The total HI mass of the NGC 2388/9 system is $1.7 \times 10^{10} M_\odot$, with roughly two-thirds of that emission confined to the galaxies and the remainder in bridge and tail material. HI emission is also detected at similar redshift from two nearby companions, GALEX-ASC J072927.38+335411.0 ($cz \approx 4080 \text{ km s}^{-1}$, $M_{HI} = 4 \times 10^8 M_\odot$, 84 kpc projected separation from NGC 2389) and GALEXASC J072911.71+335653.1 ($cz \approx 3925 \text{ km s}^{-1}$, $M_{HI} = 3 \times 10^8 M_\odot$, 88 kpc projected separation). The HI in the companions is consistent with regular rotation and they do not appear to be directly involved in the ongoing encounter of NGC 2388/9.

Stierwalt et al. (2013) identify this system as “pre-merger”, based on its mid-infrared morphology. However, the clear presence of a tidal tail and bridge in the HI is consistent with the system having already experienced first pass. That the

Table 3.2. Measured HI Properties

Object	M_K	$\log_{10}((L_{\text{IR}}/L_{\odot}))$	D_L Mpc	Morph	HI Flux Jy km s^{-1}	HI Mass $\times 10^9 M_{\odot}$
NGC 2342	-24.73 ± 0.03	11.31	78.0	S pec	31.4 ± 2.7	$40. \pm 3$
NGC 2388	-24.26 ± 0.15	11.28	62.1	S?	22.8 ± 2.6	$17. \pm 0.1$
NGC 0317B	-23.44 ± 0.18	11.19	77.8	SB?	5.0 ± 0.6	6 ± 0.1
IRAS 05083+2441	-23.91 ± 0.15	11.26	99.2	S	4.8 ± 2.8	$10. \pm 6$
NGC 3221	-25.10 ± 0.15	11.09	65.7	SB(s)cd	36 ± 7.1	32 ± 6.3
NGC 6701	-24.56 ± 0.15	11.12	62.4	(R')SB(s)a	7.8 ± 2.5	5.3 ± 1.7
CGCG 141-034 ^a	-23.96 ± 0.15	11.20	93.4	...	< 0.06	< 0.09
CGCG 142-034	-24.40 ± 0.15	11.18	88.1	...	7.8 ± 4.17	$10. \pm 0.5$

Note. — Compilation of source properties from the literature and HI properties from this work. Col 1 – Source name, Col 2 – Absolute K-band magnitude from 2MASS (Skrutskie et al. 2006), Col 3 – L_{IR} from Armus et al. (2009), Col 4 – D_L from Armus et al. (2009), Col 5 – Morphological type from RC3 (de Vaucouleurs et al. 1991), Col 6 – Integrated HI flux, Col 7 – HI mass.

^aWhile CGCG 141-034 was not detected in, a nearby companion was. See text for details.

stellar distribution is relatively unperturbed is consistent with the stars having a smaller scale-length than the H I and the system being viewed soon enough after first pass that the extended H I has responded to tidal effects but the stars, deeper in the potential well, have not.

NGC 2342 NGC 2341 and 2342 are both embedded in a common H I envelope (Figure 3.2). The H I coincident with both disks is consistent with rotation, but the larger-scale envelope shows little coherent velocity structure, though the channel maps hint at the presence of a tidal tail to the South. The rotation sense of both disks is similar, suggestive of a prograde-retrograde encounter. The total H I mass is $4 \times 10^{10} M_{\odot}$. At a nearby position, H I is detected in emission, though there does not appear to be a cataloged optical counterpart ($cz \approx 5290 \text{ km s}^{-1}$, $M_{HI} = 8 \times 10^7 M_{\odot}$, 07h08m51.5s +20d35m47s). Visual inspection of DSS2 imaging shows faint optical emission, consistent with a dwarf galaxy.

This system was classified by Stierwalt et al. (2013) as a “pre-merger”. That the galaxies are in a common envelope of H I and show tentative evidence for a gaseous tidal tail suggests the system has already experienced first pericentric pass.

NGC 0317B At optical wavelengths, NGC 0317B shows a disturbed morphology, with a strong 2-arm spiral pattern and a faint umbrella structure to the Southeast. It appears to also be interacting with NGC 0317A. The H I emission is spatially coincident with both the disk and the umbrella and perhaps a tidal tail to the North of NGC 0317A (Figure 3.3). To the South, UGC 00594 is detected in H I and is connected to NGC 317B by a bridge of H I. It is unclear if the H I spatially coincident with the umbrella structure is part of the bridge or directly associated with the umbrella. The total system has an H I mass of $6 \times 10^9 M_{\odot}$.

The morphology and H I kinematics suggest an ongoing interaction between NGC 0317B, NGC 0317A, and UGC 00594. The interaction between NGC 317B and NGC 317A appears to have gone beyond first pass, as the data show a H I tail to the North of NGC 317A. The elongated and loosely wound spiral arms in NGC 317B are consistent with the appearance of disks immediately following first pass (see Barnes 1992). The interaction between the NGC 317A/B system and UGC 00594 is also likely beyond first pass, owing to the presence of bridge material. Due to the unknown true separations and relative velocities, it isn't clear in which order the interactions have occurred, or if the enhanced star formation was triggered by one or both of the interactions.

IRAS 05083+2441 H I emission is detected on the main body of this galaxy and its companion, 2MASX J05112888+2445593. A tidal feature is seen extending to the Northeast, consistent with an ongoing tidal interaction (Figure 3.4). The total H I mass is $10^{10} M_{\odot}$. The bulk of the H I emission appears to be centered on 2MASX J05112888+2445593, but assigning masses to the individual systems is problematic at the resolution of these data.

NGC 3221 The H I observations show emission from a relatively undisturbed massive disk galaxy (Figure 3.5), with an extension to the south that appears to be a tidal tail or stream. The H I data are consistent with an edge-on disk experiencing a minor merger or interaction, the debris of which is visible to the southern edge of the disk. There is no evidence for significant tidal debris out of the plane, suggesting that NGC 3221 is experiencing a nearly perfectly prograde interaction (i.e., the orbital plane of the interloper is close to NGC 3221's disk plane) or that the mass of the interloper is too low to cause significant tidal disturbance to the more massive galaxy. The total

H I mass is $3.2 \times 10^{10} M_{\odot}$. to the more massive galaxy

NGC 6701 This system appears to be the product of a low-mass interaction. The H I on NGC 6701 appears to be a regularly rotating disk (Figure 3.6). The two-armed spiral may have been created or enhanced by the interloping galaxy, 2MASX J18423638+6038480, which has associated H I emission and possibly a faint tidal tail stretching to the West or a lopsided H I disk. The total H I mass of the system is $5.3 \times 10^9 M_{\odot}$, with 70% of the mass residing in NGC 6701.

CGCG141-034 No H I emission is detected on the main body of this system (Figure 3.7), with an upper limit of $9 \times 10^7 M_{\odot}$. However, H I is detected to the South, coincident with GALEXASC J175656.23+235838.4. The nearby object has a total H I mass of $4.5 \times 10^8 M_{\odot}$ at $cz \approx 5840 \text{ km s}^{-1}$ and $\sim 55 \text{ kpc}$ projected separation. The H I is slightly elongated perpendicular to the major axis of the beam and curves towards CGCG 141-034. While signal-to-noise is somewhat low, the emission coincident with GALEXASC J175656.23+235838.4 is tentatively interpreted as bridge material due to a recent flyby, suggesting the star formation in CGCG 141-034 may be due to gas accreted from the interloper as part of the interaction.

CGCG142-034 Faint H I emission is detected on the main bodies of both galaxies, but there is no obvious detection of tidal features (Figure 3.8), due to low signal-to-noise of these observations. The total H I mass is $10^{10} M_{\odot}$.

3.4 Triggers of Activity in LIRGs

Due to the nature of this sample, there is a mix of merging systems and non-interacting systems. These non-interacting systems may have been perturbed recently by a flyby,

have accreted a minor satellite, or might have a slightly unstable disk with higher gas fractions. Any of these possibilities could result in factors of 5–100 increase star formation activity over a galaxy’s quiescent state (e.g., Mihos et al. 1992; Mihos & Hernquist 1994a; Draper & Ballantyne 2012). Due to the frequent occurrence of H I disks which exceed the diameter of stellar disks, these data provide a more sensitive probe to past tidal perturbations. Of the systems in our sample, only 1 system (NGC 6701, see Figure 3.6) appears to be a relatively non-disturbed system in H I, although the H I emission is off-center in 2MASX J18423638+6038480, which would be consistent with an ongoing interaction.

The systems which look relatively undisturbed in the optical yet show signs of interaction in H I can easily be understood as being early-stage galaxy interactions, where the two galaxies are likely just past their first pericenter pass. Their identification as LIRGs suggests somewhat enhanced star formation perhaps due to the strong tidal interactions they are experiencing. This is consistent with predictions from some numerical simulations (e.g., Mihos & Hernquist 1994b) which predict the onset of enhanced star formation should quickly follow first pass.

It is possible the enhanced star formation in these systems is from episodic IGM accretion rather than the early-stage interaction. In this scenario, while the systems are clearly undergoing an interaction, the enhanced star formation is not causally related to the interaction but is a chance event. At present, we are unable to distinguish between these two scenarios, however all three of the morphologically identified “pre-merger” systems show evidence for ongoing tidal interactions, making an interaction trigger more consistent with the available data.

Four systems detected in this H I survey were identified by Stierwalt et al. (2013) as being non-merger systems (NGC 3221, NGC 6701, CGCG 141-034, and IRAS05083+2441).

Of the four, both NGC 3221 and IRAS05083+2441 show evidence for an ongoing high mass ratio interaction—both in the form of a bridge connecting the two involved galaxies and tidal tails. The evidence for interaction in CGCG 141-034 is somewhat circumstantial, but the presence of a nearby companion with disturbed HI morphology is suggestive. Similarly, while no bridge or tidal tails are seen in NGC 6701, the off-center HI distribution in 2MASX J18423638+6038480 is consistent with a retrograde passage, though isolated galaxies often show HI asymmetries (Bosma 1981), so the asymmetry may be a red herring in the case of this particular system.

Three systems (NGC 2342, NGC 2388, NGC 0317B) were classified by Stierwalt et al. (2013) as “pre-mergers” based on their mid-infrared morphology, but show clear evidence for ongoing interactions in the observed HI distribution. This suggests the LIRG activity in these systems is the result of the tidal interactions rather than secular processes.

3.4.1 On Determinations of the (Minor) Merger Rate

For a point of comparison with these infrared-selected systems, it would make for interesting future work to study a sample of less luminous disk systems to identify the frequency of such minor mergers. This could help answer interesting questions in galaxy evolution: is there a certain type of interaction necessary to trigger a LIRG event? and for systems which are LIRGs, how much time will they spend in this state of elevated activity? Some effort has been devoted to determining the rate of minor-mergers (e.g., Lotz et al. 2011) using various criteria such as the galaxy asymmetry and $G - M_{20}$. It would be a useful exercise to apply these methods to the systems identified here as minor mergers to ensure they would be identified as such. Future large-area HI surveys with WSRT/Apertif, MeeRKAT, and ASKAP

will provide opportunities to determine merger rates using a more sensitive probe of galaxy interactions.

3.4.2 Dynamical Modeling

Several of the observations presented here provide excellent opportunities for dynamical modeling of the 2D kinematics. The major merger systems (e.g., NGC 2388/9, NGC 2341/2) appear to be shortly after first pericenter pass (earlier than The Mice or NGC 5257/8; Barnes 2004; Privon et al. 2013); modeling these systems may provide an opportunity to study how quickly star formation respond to tidal encounters during the tens of Myr immediately following a close passage, providing some constraints on star formation models.

Modeling of the minor merger candidates would provide information on the character of encounters which sufficiently perturb a galaxy and induce significant amounts of star formation (Mihos et al. 1992, G. C. Privon et al. *in prep*). The longevity of such enhanced events is also interesting – coupled with the merger rate, this could constrain the effect of minor mergers on the build-up of stellar mass in galaxies.

3.5 Conclusions

Using new HI observations of nearby LIRGs selected from the GOALS sample, the interaction states of LIRGs with unperturbed stellar morphologies are examined. All of the systems presented here with high signal-to-noise HI observations which were morphologically classified in the optical or mid-infrared as non-interacting or pre-interaction systems show evidence for ongoing tidal interaction—via the presence of tidal tails and bridges. Aside from demonstrating the utility of HI in diagnosing merger activity, the observations provide an alternate perspective on the classification

of these particular systems, diminishing the number of LIRGs in the local universe whose activity could plausibly be caused by secular processes or accretion from the IGM. Additionally, these observations emphasize the role minor mergers and interactions play in triggering star formation in galaxies.

Acknowledgements

G.C.P. was supported by NSF grants AST 1109475 and 02-06262, and by a Visiting Graduate Research Fellowship at the Infrared Processing and Analysis Center / Caltech. This work was supported in part by National Science Foundation Grant No. PHYS-1066293 and the hospitality of the Aspen Center for Physics.

The author thanks the staff at ASTRON/WSRT for assistance in planning and carrying out the WSRT observations, and the staff of the GMRT who have made the GMRT observations possible. GMRT is run by the National Centre for Radio Astrophysics of the Tata Institute of Fundamental Research.

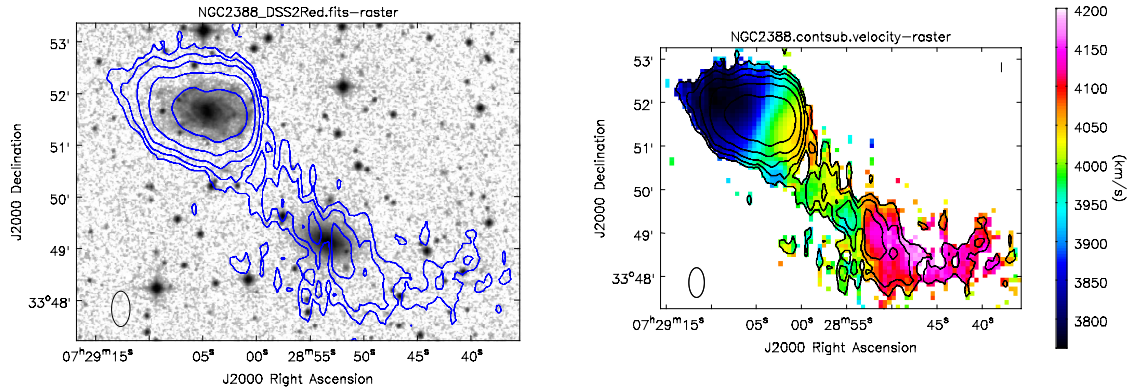


Fig. 3.1.— WSRT data on NGC 2388/9. Left: H I contours (beginning at $0.08 \text{ Jy beam}^{-1} \text{ km s}^{-1}$ and increasing by factors of 2) on a DSS2 Red image. Right: Intensity-weighted velocity map of the H I emission (colorscale) with H I total-intensity contours in black (same scaling as left panel).

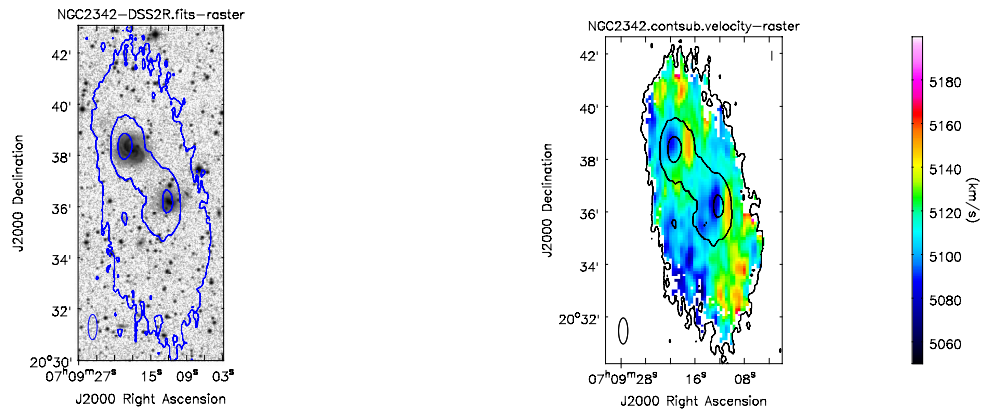


Fig. 3.2.— WSRT data on NGC 2341/2. Left: H I contours (beginning at $0.05 \text{ Jy beam}^{-1} \text{ km s}^{-1}$ and increasing by factors of 2) on a DSS2 Red image. Right: Intensity-weighted velocity map of the H I emission (colorscale) with H I total-intensity contours in black (same scaling as left panel).

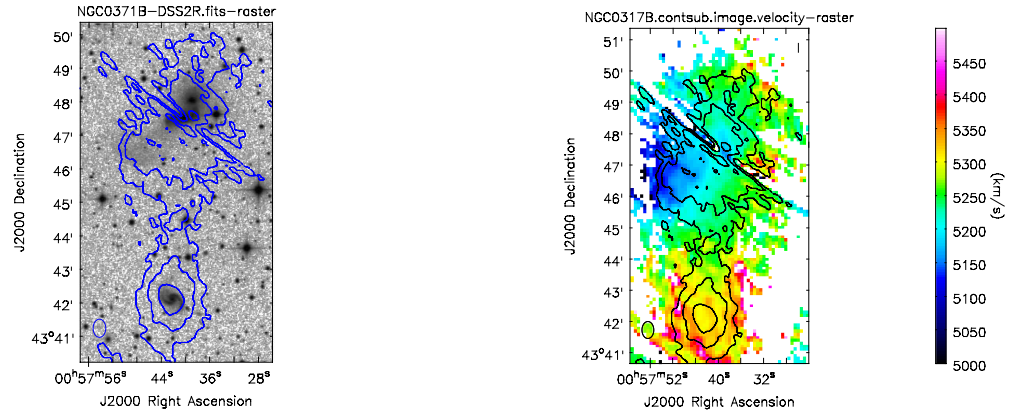


Fig. 3.3.— WSRT data on NGC0317B. Left: H I contours (beginning at $0.025 \text{ Jy beam}^{-1} \text{ km s}^{-1}$ and increasing by factors of 2) on a DSS2 Red image. Right: Intensity-weighted velocity map of the H I emission (colorscale) with H I total-intensity contours in black (same scaling as left panel). An incompletely removed grating ring from a nearby source is the cause of the near-linear feature with a PA of 45° East of North.

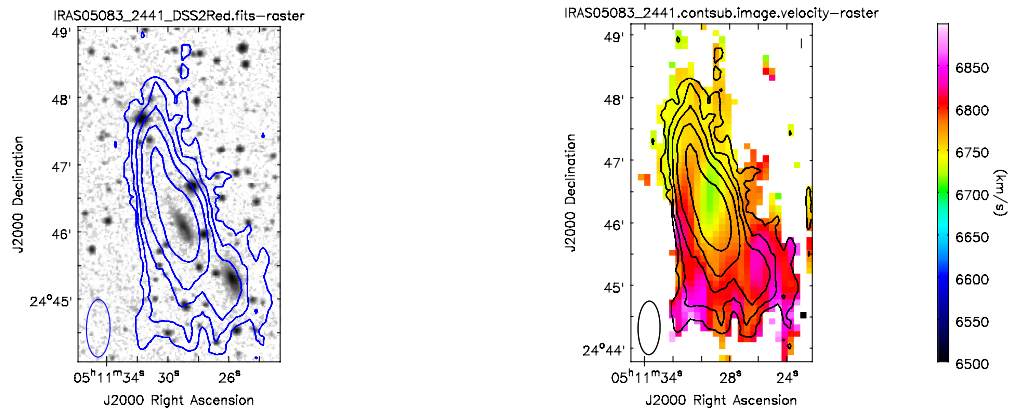


Fig. 3.4.— WSRT data on IRAS05083+2441. Left: H I contours (beginning at $0.05 \text{ Jy beam}^{-1} \text{ km s}^{-1}$ and increasing by factors of 2) on a DSS2 Red image. Right: Intensity-weighted velocity map of the H I emission (colorscale) with H I total-intensity contours in black (same scaling as left panel).

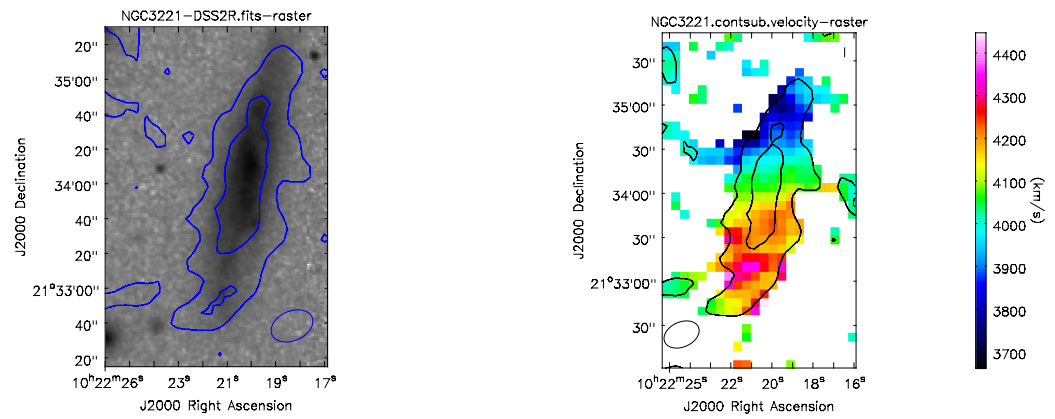


Fig. 3.5.— VLA data on NGC 3221. Left: H I contours (beginning at $1.2 \text{ Jy beam}^{-1} \text{ km s}^{-1}$ and increasing by factors of 2) on a DSS2 Red image. Right: Intensity-weighted velocity map of the H I emission (colorscale) with H I total-intensity contours in black (same scaling as left panel).

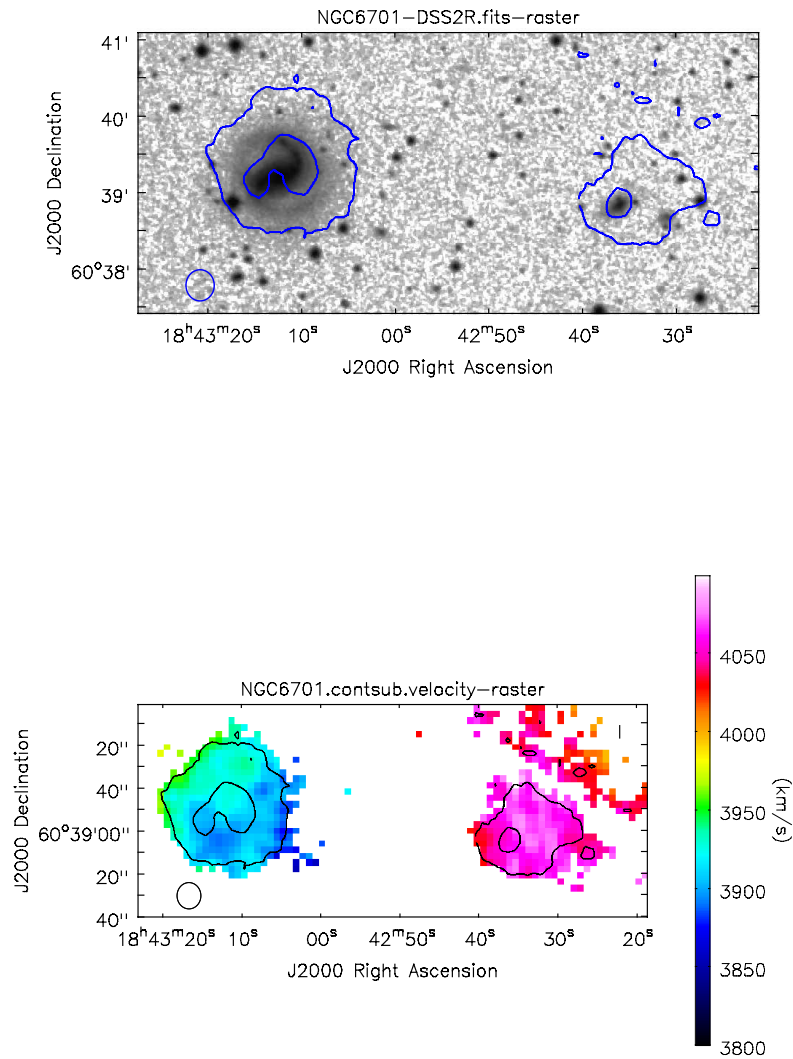


Fig. 3.6.— WSRT data on NGC6701. Left: HI contours (beginning at $0.08 \text{ Jy beam}^{-1} \text{ km s}^{-1}$ and increasing by factors of 2) on a DSS2 Red image. Right: Intensity-weighted velocity map of the HI emission (colorscale) with HI total-intensity contours in black (same scaling as left panel). The orange/red mottling to the Northwest is a data artifact which has not been fully calibrated out.

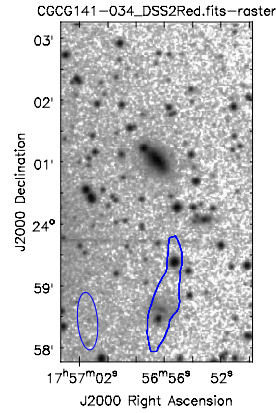


Fig. 3.7.— WSRT data on CGCG 141-034. Left: H I contour ($0.07 \text{ Jy beam}^{-1} \text{ km s}^{-1}$) on a DSS2 Red image. No velocity field is presented due to low signal-to-noise of the H I emission.

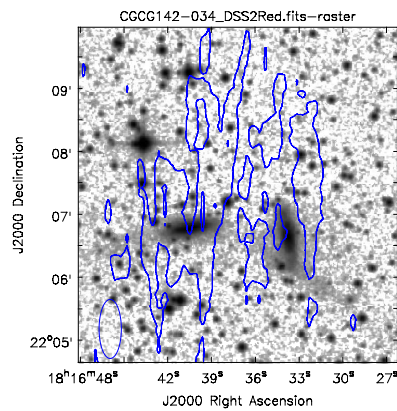


Fig. 3.8.— WSRT data on CGCG 142-034. Left: H I contours (beginning at $0.12 \text{ Jy beam}^{-1} \text{ km s}^{-1}$ and increasing by factors of 2) on a DSS2 Red image. No velocity field is presented due to low signal-to-noise of the H I emission.

Chapter 4

Dynamical Modeling of Galaxy Mergers using Identikit¹

4.1 Introduction

There is increasingly strong evidence that galaxy mergers are an important aspect of galaxy evolution. This evidence includes the hierarchical formation of structure observed in Λ CDM cosmological simulations (e.g., Springel et al. 2005; Boylan-Kolchin et al. 2009; Angulo et al. 2012), as well as direct observations of high redshift systems with morphological irregularities consistent with merging or interacting systems (e.g., Engel et al. 2010; Busmann et al. 2012). As is observed at high-redshift, the most extreme star-forming systems and many of the most luminous active galactic nuclei (AGN) in the local Universe are associated with mergers (e.g., Sanders et al. 1988; Bahcall et al. 1995). Galaxy mergers can redistribute existing stars as well as trigger the formation of new stars through compression of gas clouds and the resulting

¹Published in the *Astrophysical Journal* as “Dynamical Modeling of Galaxy Mergers Using Identikit”, Volume 771, Article id. 120, with the following authors: G. C. Privon, J. E. Barnes, A. S. Evans, J. E. Hibbard, M. S. Yun, J. M. Mazzeella, L. Armus, and J. Surace.

increased gas density.

Numerical models for merging systems were first convincingly demonstrated by Toomre & Toomre (1972, hereafter TT72) and have been updated in subsequent decades. Historically, finding an accurate dynamical model has been a very time consuming process, owing to the need for iterative matching of self-consistent simulations. This difficulty has severely limited the number of systems with dynamical models. For a relatively recent summary of systems with dynamical models, see Barnes & Hibbard (2009, table 2. Hereafter BH09).

Identikit (BH09) utilizes a novel approach to simplify matching of dynamical models to mergers. This method, described in detail in Section 4.3, utilizes hybrid test particle & N-body simulations and a data visualization technique which allow rapid exploration of the parameter space for galaxy mergers. This will allow a sample of galaxy mergers with dynamical models to be assembled. Such a sample could be paired with detailed simulations incorporating gas physics, star formation, and feedback to enable a comparison of the observed star formation and AGN properties in mergers with the characterization of those phenomena in simulations. This can test and lead to an improved understanding of the sub-grid physics necessary to most accurately incorporate this physical activity in numerical models.

At a minimum, a dynamical model² of a merger should reproduce the morphology and kinematics of the system. For the majority of systems modeled to date, this primarily means matching the tidal features formed during close passage of two galaxies with dynamically cold components. For prograde passages (disk spins aligned with the

²Here, we take “dynamical model” to include the minimum number of geometric and orbital parameters necessary to specify a galactic encounter. This includes the orbital parameters (mass ratio, orbital eccentricity, and pericentric separation), disk orientations relative to the orbital plane, and factors which relate to the observations (time of viewing, viewing angles, and scalings to physical units). With this definition, prescriptions for gas physics, star formation, AGN activity, etc. can be paired with a dynamical model to study/predict the appropriate phenomenon.



angular momentum of the orbit), quasi-resonant tidal interactions create tails (TT72; D’Onghia et al. 2010) such as those seen in the Antennae, The Mice, and other systems (Arp 1966; Schweizer 1982; Hibbard et al. 2001; Hibbard & van Gorkom 1996). These tails, once created, evolve ballistically and are relatively unaffected by the later evolution of the main galaxy bodies. Thus they provide the best constraints on the initial conditions of the encounter.

An ensemble of dynamical models of mergers can enable a study of merger driven activity constrained in more detail than a statistical comparison of data and simulations. The difficulty of arriving at dynamical models for mergers has thus far precluded the assembly of a large sample of observationally-matched dynamical models. The aim of this paper is to demonstrate the feasibility of obtaining dynamical models with the Identikit technique.

The paper is organized as follows: we begin by describing the sample of mergers in Section 4.2. In Section 4.3 the Identikit hybrid and self-consistent simulations are described, and the results of matching the simulations to observations with Identikit are given in Section 4.4. We use a cosmology with $H_o = 73 \text{ km s}^{-1} \text{ Mpc}^{-1}$, $\Omega_M = 0.27$, and $\Omega_{vac} = 0.73$, unless otherwise noted.

4.2 The Sample and Data

The four galaxy mergers in this initial sample are NGC 5257/8, The Mice, Antennae, and NGC 2623. They were selected on the basis of having prominent tidal tails, indicative of prograde encounters (hence easier to match to simulations³) and also

³In their study of simulated mergers BH09 found that simulated prograde and retrograde encounters were modeled with similar success rates. Also, preliminary work on expanding this sample to retrograde encounters shows observed retrograde systems can be successfully modeled using this technique (Privon et al. *in prep*).



on the availability of high quality optical imaging and HI observations. The detailed morphological and kinematic information from these data is critical in matching a dynamical model to each system using Identikit. The systems appear to span a range of merger phases, based on their optical morphology. Additionally they exhibit a range in infrared luminosity and therefore star formation rates (e.g., Sanders et al. 2003; Kennicutt 1998).

All four systems are well studied mergers. NGC 5257/8 and NGC 2623 are part of the Great Observatories All-sky LIRG Survey (GOALS, Armus et al. 2009), which consists of imaging and spectroscopy on all LIRGs in the IRAS Revised Bright Galaxy Sample (RBGS, Sanders et al. 2003) from radio wavelengths through X-rays. Where appropriate we leverage this detailed dataset to assist in the development and interpretation of our models. The other two systems, The Mice and the Antennae, are also well studied systems with a wealth of existing data.

NGC 5257/8 and NGC 2623 do not have previously published dynamical models while The Mice and the Antennae have existing dynamical models (see Sections 4.2.2 and 4.2.3). The aim of this paper is not to determine the “best” of competing dynamical models, rather it is to demonstrate the feasibility of Identikit in obtaining valid models.

For all sources, redshifts were retrieved from NED, D_L was obtained from NED’s “cosmology corrected quantities”, and L_{IR} was computed using D_L , the IRAS fluxes from NED’s photometric database, and the prescription in Sanders & Mirabel (1996, Table 1). Some properties of these objects are summarized in Table 4.1. A comparison of L_{IR} determined by SED fitting versus estimates from IRAS fluxes by U et al. (2012) found both methods to provide similar results.

In the following subsections we describe the properties of the systems in our sam-



Table 4.1. Dynamical Modeling Sample Description

Source	Other Names	z	D_L Mpc	L_{IR} $\times 10^{11} L_\odot$
NGC 5257/8	Arp 240, VV 55, IRAS F13373+010	0.0225	98.3	3.9
The Mice	NGC 4676A/B, Arp 242, VV 224, IRAS 12437+3059	0.022049	96	0.79
Antennae	NGC 4038/9, Arp 244, VV 245, IRAS 11593-1835	0.005688	28.4	1.1
NGC 2623	Arp 243, VV 79, IRAS 08354+2555	0.018509	80.6	3.6

Note. — Col 1: Source name as used in this paper. Col 2: Other names used in the literature. Col 3: redshift obtained from NED. Col 4: Luminosity distance from NED’s Cosmology-Corrected Quantities. Col 5: Infrared luminosity from IRAS observations. See text for details.

ple based on previous studies. The dynamical models presented here utilize the H I observations and optical imaging. Other data sets and results are included as context for the merger-driven activity in each system.

4.2.1 NGC 5257/8

The pair NGC 5257 and NGC 5258 both show clear evidence for tidal distortion, with tidal tails and enhanced spiral features visible in stellar light. Neither nucleus shows evidence for the presence of a strong AGN. Photometric estimates and SED modeling of the system provide stellar mass estimates of $1 - 3 \times 10^{11} M_{\odot}$ (Howell et al. 2010; U et al. 2012).

HST ACS imaging of NGC 5257/8 was obtained as part of the GOALS observing program (pid10592 PI: Evans; Evans et al. in prep) in the F435W and F814W filters. Over 800 star clusters are visible in the image (Vavilkin et al. in prep). The majority of these clusters are in the main body and spiral arms, but there are also clusters in the more extended tidal features. Using GALEX UV observations in combination with the FIR luminosity, Howell et al. (2010) find total SFRs of 35.6 and 36.0 $M_{\odot} \text{ yr}^{-1}$ for NGC 5257 and 5258, respectively.

Spitzer imaging of the system shows the dominant source of infrared emission to be off-nuclear, in sharp contrast to the general behavior of LIRGs where activity is frequently concentrated in the nucleus (Haan et al. 2011). These star forming regions lie coincident with the spiral arms which are likely enhanced by the tidal interaction. This may be leading to enhanced compression of the gas, beyond that typically occurring in spiral arms. Independent of the dynamical modeling, this system affords an opportunity to study extreme star formation in a region of the galaxy where influence from an AGN can be reliably ruled out.



Iono et al. (2005) presented VLA HI observations, mapping the distribution of the atomic gas in the main bodies and the tails. The system has a total HI mass of $M_{\text{HI}} = 3.3 \times 10^{10} M_{\odot}$. The tidal tail in NGC 5257 is relatively short in projection, suggesting a weak tidal coupling (i.e., not a strongly prograde encounter) or a tidal disturbance predominantly along the line of sight. The weak HI emission here may be due to a geometry for the system in which the HI in the tail has been ionized by star formation in the disk of the galaxy (e.g., the base of the northern tail in the Antennae: Hibbard et al. (2001)). The prominence of the tidal tail in NGC 5258 is suggestive of a prograde interaction. The eastern tail has a greater extent in HI than in starlight. This suggests the HI in the tail was initially less tightly bound, i.e., in an extended disk of the type often seen in non-interacting disk galaxies.

The system has no previously published dynamical models. For input constraints to Identikit, we use the HI observations from Iono et al. (2005) and the HST/ACS F814W images from Evans et al. (in prep). The HI observations have an angular resolution of $\sim 20''$ (9.1 kpc, FWHM) and a velocity resolution of 11 km s^{-1} . The HST image has a resolution of $0.05''$.

4.2.2 The Mice

The Mice is a well known interacting galaxy pair. The system received its name from the prominent tails which result in the system resembling two “playing mice” (Vorontsov-Vel’Iaminov 1958). These prominent tidal tails suggest a prograde interaction. The straightness of the northern tail is consistent with the spin vector of the northern galaxy being near the plane of the sky. The relative length of the tidal tails suggests the galaxies are of roughly equal mass.

HST/NICMOS imaging of the component galaxies shows both have compact nuclei



(Rossa et al. 2007). A comparison of NGC 4676A and NGC 4676B with HST/WFPC2 imaging is consistent with NGC 4676A being of a slightly later Hubble type than NGC 4676B (Laine et al. 2003).

Using Keck’s multi-object spectrograph, Chien et al. (2007) observed 12 optically visible star clusters in the Mice, selected from HST/ACS imaging of the system (de Grijs et al. 2003). The observed clusters were predominantly young (< 10 Myr), but 2 of the clusters had ages ~ 170 Myr.

This merger system has been the subject of many dynamical studies (e.g., TT72; Mihos et al. 1993; Gilbert & Sellwood 1994; Sotnikova & Reshetnikov 1998; Barnes 2004). The existing models have orbital parameters and disk inclinations which are in agreement with each other.

For our model matching we utilize HI data and a deep optical R-band image from Hibbard & van Gorkom (1996). The HI data has a resolution of $20''$ (8.9 kpc) and a velocity resolution of 43.1 km s^{-1} . The total HI mass in the system is $7.5 \times 10^9 M_{\odot}$. The optical image was taken in $1.9''$ seeing; this resolution is sufficient for our analysis.

4.2.3 Antennae

The Antennae consists of two distinct galaxies (NGC 4038 and NGC 4039), each with long tidal tails which cross close to their respective disks. The “overlap region” of the disks contains most of the molecular gas (Wilson et al. 2000) and is the primary source of the far-infrared luminosity (Mirabel et al. 1998; Xu et al. 2000), though it is not clear if the activity in this region is due to physical contact between the two disks or if they are seen as overlapping in projection. Neither nucleus has evidence for a strong AGN. As with the previous systems, the tidal tails suggest prograde



interactions for both disks.

The Antennae has been the subject of many papers which analyze its dynamical properties (e.g., TT72, van der Hulst 1979; Mahoney et al. 1987; Barnes 1988; Mihos et al. 1993; Karl et al. 2010). These various models generally reproduce the morphology and/or the kinematics of the large scale features. The more detailed hydrodynamic model of Karl et al. (2010) appears to match the smaller scale features as well as providing a natural explanation for the “overlap region” as a region of physical contact between the disks. However, this model occupies a different region of parameter space when compared to previous efforts. We discuss the differences between our derived model and previously published models in Sections 4.4.2 and 4.4.3.

HI and an optical R-band image presented in Hibbard et al. (2001) were used to constrain the dynamical model. The HI observations were taken with the VLA and cover the system at an angular resolution of approximately $10''$ (1.3 kpc) and a velocity resolution of 5.21 km s^{-1} . The optical image has $1''$ seeing.

4.2.4 NGC 2623

NGC 2623 is, by visual inspection, a late stage merger. HST/ACS images of the system show a single nucleus and prominent 20 – 25 kpc tidal tails extending to the East and West (Evans et al. 2008). The stellar mass of the system is estimated at $6 \times 10^{10} M_{\odot}$ and $\sim 2 \times 10^{10} M_{\odot}$ based on photometric and SED estimates, respectively (Howell et al. 2010; U et al. 2012).

The merger remnant has ~ 100 unresolved star clusters (Evans et al. 2008). Assuming negligible to moderate extinction, the HST/ACS two filter broadband photometry of the clusters is consistent with ages of 1 – 100 Myr. Rothberg et al. (2007)



give an alternate estimate for the age range of 100–250 Myr, using an additional filter in the analysis. Detailed spectroscopy of 18 clusters by Chien (2009) found cluster ages between 3–250 Myr, with most of the observed clusters younger than 100 Myr. The overall star formation rate in the system is $\sim 70 M_{\odot} \text{ yr}^{-1}$ (Howell et al. 2010).

The merger core hosts an AGN as determined from the hard X-ray spectrum (Maiolino et al. 2003; Evans et al. 2008) and the presence of the [Ne V] 14.3 μm line (Evans et al. 2008; Petric et al. 2011). However the energetics of the system are dominated by star formation. Lonsdale et al. (1993) detected a high brightness temperature ($T > 10^7 \text{ K}$) radio core consistent with an AGN, but contributing less than 10% of the total radio flux. This suggests the bulk of the radio flux is associated with star formation.

We utilize HI observations obtained with the VLA in both the D and C array configurations (Hibbard & Yun 1996), providing an angular resolution of 16'' (6 kpc). The HI shows a double tail morphology, with somewhat more emission from the western tail. The line of sight velocity of the Eastern tail increases monotonically from the middle of the tail to the end. In contrast, the Western tail velocity initially decreases with increasing radius. This tail then loops around in both position and velocity, curving towards the North and back around East, as well as reversing the line of sight velocity.

We have measured the flux of the HI emission as: $0.71 \text{ Jy km s}^{-1}$. At $D_L = 80.6 \text{ Mpc}$ and taking into account the fact that we are missing flux due to HI absorption against the radio continuum, this corresponds to $M_{\text{HI}} > 2.3 \times 10^8 M_{\odot}$.

The HI absorption is seen against the radio continuum which likely originates from the strong star formation in the system. At this resolution the absorption is unresolved, and the radio continuum may be smaller than the 16'' beam. The absorp-

tion occurs almost the entire 450 km s^{-1} bandwidth of the VLA observations, which agrees with single-dish HI observations with the GBT (Frayser et al. *in prep*). Taking the NVSS flux of 95.7 mJy (Condon et al. 1998) we estimate the total absorbing column: $N_{\text{H}} = 3.6 \times 10^{21} \text{ cm}^{-2}$ (for a covering factor of 1 and a spin temperature $T_{\text{spin}} = 100 \text{ K}$).

Optically, the main body of the galaxy appears to have only a single nucleus (Evans et al. 2008; Haan et al. 2011), implying that higher resolution is required to resolve the nuclei of the progenitor galaxies, or the nuclei have already coalesced. In this case, one might expect the most tightly bound portions of the tails (at the smallest radii) to have reached apocenter and begun falling back into the system. Unfortunately, due to the strong absorption in the center, we are unable to use HI to probe for the existence of a velocity reversal at small distances which would suggest infall. Deep optical spectra of the tails to determine the kinematic properties using stellar absorption lines would be an interesting confirmation of this.

To complement the HI data with constraints on the stellar distribution, we utilize the HST/ACS F814W image from Evans et al. (2008).

4.3 Matching of Dynamical Models

Specifying a model of a disk-disk galaxy merger requires a minimum of 16 parameters. These include orbital parameters, galaxy disk inclinations, the viewing direction, and scalings to physical units. The orbital parameters are: mass ratio of the two galaxies (μ), pericentric separation of the idealized Keplerian orbit of point masses⁴ (p), and the eccentricity of the orbit (e). The orientation of each disk is specified by two angles,

⁴The model galaxies are initially set on a Keplerian orbit, but will deviate from this orbit shortly before first pericenter passage.



the angle between the normal of the orbital plane and the unit vector of the disk’s angular momentum (inclination, i), and the longitudinal orientation of the angular momentum unit vector⁵ (argument of periaapse, ω). For an illustration of these angles, see TT72 Figure 6a.

The above parameters are sufficient to describe the dynamical evolution of the system. To specify an observation, additional parameters must be given, including: three angles corresponding to the viewing angle of the merger ($\theta_X, \theta_Y, \theta_Z$), a length scaling (\mathcal{L}), a velocity scaling (\mathcal{V}), and the time of viewing⁶ (t). \mathcal{L} and \mathcal{V} are then used to determine the mass scaling factor \mathcal{M} for the system: $\mathcal{M} \propto \mathcal{V}^2 L$. These scaling factors can also be used to arrive at a time scaling factor to convert the simulation time into physical units ($\mathcal{T} \propto \mathcal{L}/\mathcal{V}$). The final three parameters are the location of the system’s center of mass (X, Y, z).

Identikit (BH09; Barnes 2011) combines the use of hybrid self-consistent halos and test particle disk simulations (described in Subsection 4.3.1) with a visualization technique (described in Subsection 4.3.2) to facilitate rapid comparison of seven dimensional models ($x, y, z, v_x, v_y, v_z, t$) with three dimensional data (α, δ, v_z). Here we limit ourselves to the “Identikit 1” technique of BH09, which relies on manual investigation of parameter space.

4.3.1 Test Particle Simulations

Identikit simulations are created by first selecting values for μ, r_{peri} , and e . Then self-consistent galaxy models consisting of a spherical dark matter halo (NFW pro-

⁵We define ω for the idealized Keplerian orbit, where the angle is the longitudinal argument relative to the line of nodes at pericenter. Due to the more rapid orbital decay of the extended mass distribution, pericenter will occur earlier than in the idealized case. This will cause the true ω value to differ slightly from the Keplerian approximation.

⁶We set the idealized Keplerian orbit to have first pericenter passage at $t = 2$ time units.



file, Navarro et al. 1996), spherical bulge (Hernquist profile, Hernquist 1990), and a “spherical” disk are generated using the Zeno software package⁷. These “live” N-body galaxies are then populated with spherical swarms of massless test particles on circular orbits, representing all possible disk orientations. For details of the construction of these simulations see BH09.

These hybrid N-body and test particle models are placed on an orbit corresponding to p and e , and then evolved using standard numerical techniques (a treecode, e.g., Barnes & Hut 1986). The positions and velocities of the test particles, which respond to the changing potential defined by the massive components, are saved at many snapshots throughout the observations. After the fact, specific disk orientations (i, ω) can be extracted by selecting only those test particles with the appropriate initial angular momentum vectors.

By running simulations with different values of (μ, p, e) , a large grid of models can be stored. Test particle disks from these simulations can then be loaded on demand from within the Identikit interface and compared to data.

In general, matching simulations to data is made easier by the existence of tidal tails, which evolve ballistically once created and therefore retain memory of the initial encounter passage. Their global morphology and kinematics are not strongly modified by self-gravity and so should be well-matched by test-particles. In contrast, strong spiral arms and other self-gravitating features will not be well reproduced by the test particles.

⁷<http://www.ifa.hawaii.edu/faculty/barnes/zeno/> and <http://www.ifa.hawaii.edu/faculty/barnes/software.html>



4.3.2 Data Visualization

A key aspect of Identikit is the interface to display position and velocity information derived from data cubes simultaneously with results from simulations. The standard view is a 4 panel display (e.g., Figure 1 of BH09, Figure 4.2 of this paper), showing the sky view ($\alpha - \delta$, top left), two position-velocity views ($v-\alpha$ & $\delta-v$, bottom left and top right), and a “top down” view ($\alpha-z$, bottom right).

The subset of test particles from a specific instance (t, μ, e, p ’s, ω ’s) of a hybrid simulation is loaded from the grid of models described in Section 4.3.1 and overlaid on the sky-plane and position-velocity diagrams. Identikit can move through a grid of pre-computed models, stepping through time, pericentric separation and mass ratio. Disk orientations can be changed with the display updating in real-time. Scalings and the viewing direction can also be changed in real-time to match the data.

The data constraints are provided via three of the four panels described above. The source of these constraints may vary according to the available data. We generally employ sky-plane visualizations using deep optical images overlaid with contours of the H I. The H I and stellar tails may not be co-spatial for reasons including: different scale lengths of the stellar and gaseous disks in the progenitors, ionization effects (e.g., Hibbard et al. 2001), or dissipation from an extended gas disk (Mihos 2001). Using both H I and starlight ensures the effect of the tidal interaction is accurately visualized. We utilize red optical filters in order to avoid being biased by young stellar populations. Extinction is generally low in the tails so the extended morphology is relatively unbiased by the use of optical images. The resolution of the H I is the limiting factor in terms of kinematic constraints but is sufficient for model matching. The higher resolution optical images are not degraded to the resolution of the H I, as they may provide additional posterior constraints on the match (e.g., the width of



the tidal tails, the match of self-gravitating features such as spiral arms).

The position-velocity diagrams were created using projections of the HI data cube, taken along either the α or the δ axes. An image with the maximum voxel value along the specified axis was used. This method tends to provide a more complete view of the spatial distribution of the emission, as faint emission isn't averaged together with noise. A consequence of this is that the projections don't represent the total emission at that point in $\alpha - \delta - v$ space. Therefore, comparing the data value in a given location of a projection with the density of simulation particles in that same region is not a reliable metric for evaluating the accuracy of a match.

4.3.3 Identikit Matching

Before matching in Identikit, the available parameter space was constrained as much as possible using a priori information. The general disk orientations (prograde vs. retrograde) can be guessed at using the length and prominence of tidal features. For the orbit, $e \sim 1$ is assumed based on cosmological considerations: the galaxies should have a high-eccentricity orbit with a period comparable to the Hubble Time. As noted above, the mass ratio μ can be estimated from the relative luminosities of each galaxy, if they are still separable, or from the relative length of the tidal tails. For this work, we limited ourselves to $\mu = 1$ or $\mu = 2$ mass ratios.

With rough parameter estimates for each source, the data projections were loaded into Identikit and test particles with a specific initial angular momentum overplotted (with that initial angular momentum corresponding to a requested initial disk orientation). Disk orientations, time since pericenter, viewing angles and length/velocity scalings were varied until an acceptable match to the morphological and velocity information were obtained. Typically, approximate disk orientations were established and



then the viewing angles explored until a near match of the tidal features is obtained. The match is then refined by alternately improving the disk angles and the viewing angles. Finally, length and velocity scalings were adjusted to obtain a suitable match to the velocity and spatial extents. These matches were determined by eye and were judged on the basis of having test particles in regions of the data projections where there is either stellar emission or H I emission. The presence of test particles in regions without emission is not always an issue as emission could be missing due to effects not included in our simulations (e.g., ionization of the gas).

Despite the lack of a dissipational component in the hybrid simulations, matching these test particles to the kinematics of gas is still valid in the tails. This is because gas in the tails does not experience significant dissipation as it moves outwards.

A mass scaling (\mathcal{M}) can be derived from the velocity and length scalings, which allows one to estimate the dynamical mass of the system⁸. The dynamical masses estimated from these simulations should be considered a lower limit to the true dynamical mass of a system. Lower values of the dynamical mass would be inconsistent with the velocity width and sizes observed in the objects. Due to the logarithmic dependence of the gravitational potential on the halo mass, increasing the halo mass would not significantly alter the velocity and length scalings. In other words, once the minimum mass threshold is reached, the sensitivity of these scalings to the dynamical mass is reduced.

For evaluation of test particle matches, the most weight is given to the extended tidal features. As these evolve ballistically after the initial passage, self-gravity should be relatively unimportant and will be suitably matched by test particles. Features such as spiral arms, which require self-gravity, will not be reproduced by these mass-

⁸Estimates of the baryonic mass require simulations with a self-consistent treatment of the disk (e.g. Section 4.3.4).



less test particles. As a result, mis-matches in the main bodies of the galaxy between the observations and the hybrid N-body and test particle simulations are to expected. Indeed, taking the parameters from an Identikit match and re-simulating them with a self-gravitating disk is a useful discriminant between models, particularly in systems lacking prominent tidal features.

BH09 tested Identikit by matching 36 simulated mergers without prior knowledge of a subset of the parameters (the mass model, mass ratio, and orbital eccentricity were fixed, all other parameters were randomly chosen as described in the paper). The viewing directions and spin orientations were typically recovered to within 12° and 18° , respectively. The time since pericenter was also well-recovered, with no obvious biases in the determination of that parameter. The determination of the pericentric separation, while not showing an offset, did show the largest scatter. The determination of the pericentric separation is likely uncertain by a factor of two. The only parameter which shows a noticeable bias in the best fit values compared to the true values is the velocity scaling. However, this is easily explained by the lack of velocity dispersion in the test-particle method. The test-particle disks, which initially have zero velocity dispersion, are being used to match tails formed from disks with a non-zero velocity dispersion. The velocity scaling determined by test-particle matching would thus be inflated to compensate for this.

4.3.4 Verification With Self-Consistent Simulations

After matching a dynamical model using Identikit, self-consistent simulations were carried out to verify the solution, refine the model parameters, and ensure self-gravitating features are matched. All simulations were carried out using the Zeno software.



Model galaxies were created with a NFW dark matter halo and spherical bulge. In contrast with the Identikit method, a disk of gravitating particles was inserted with the specified (i, ω) values. Our N-body simulations used 64k particles per galaxy: 8k bulge particles, 24k disk particles, and 32k dark matter halo particles. Eighty per-cent of the mass is in a dark matter halo and the remaining twenty per-cent is baryons (the bulge and the disk). These galaxy models were placed on initially Keplerian orbits with e and p values taken from the Identikit solution, then evolved using a treecode. All galaxies use the same mass model: a scale length of $\alpha^{-1} = 1/12$ for the exponential disk, bulge scale length of $a_b = 0.02$, and halo scale length of $a_h = 0.25$. The circular velocity at 3 disk scale lengths is approximately 1.26. These lengths and velocities can be converted to physical units using the scalings derived for each model. For the details of the construction of our N-body realizations see Appendix B of BH09.

Once the system has been evolved numerically, particles in the self-gravitating disks were loaded into the Identikit visualization system and compared with the same data projections used to constrain the test particle model. Minor adjustments were sometimes necessary, typically with the pericentric separation of the first passage. A model was considered sufficiently accurate if the self-consistent simulation reproduced the morphology and kinematics of the extended tidal features.

Based on the comparison of Identikit matches to simulated mergers by BH09, we are confident that a visually good Identikit match should also provide angles which are reasonably close to the true values. In practice, the disk angles derived with test particles accurately reproduce the tidal features in self-consistent realizations of the merger, with minor ($< 10^\circ$) adjustments sometimes necessary.

The baryonic mass of the galaxy can be estimated from the inclusion of the self-



gravitating disk. The disks in our model galaxies are marginally unstable to bar formation and therefore are near the upper envelope of possible disk masses. Correspondingly, the baryonic masses given in the results are near the maximum plausible value for these mass models. The dynamical mass is a lower-limit, as with the test-particle simulations. The integrated mass-to-light ratio of the system is therefore a lower limit.

The models presented here are intended to reproduce the morphology and kinematics of the large scale structure, which they appear to successfully achieve. While these systems include gas, we have not included any dissipational component in the simulations. Such a component is necessary for studying the hydrodynamics of the system but its omission here should not affect the global fit, as the large scale features and orbital decay are not strongly affected by the inclusion of gas (Barnes & Hernquist 1996).

4.4 Results and Discussion

Dynamical models were successfully matched to the four systems selected. In all systems the prominent tidal features are traced back to prograde encounters, as was expected. Parameters for dynamical matches and scalings to physical units determined by Identikit and refined by subsequent self-consistent simulations are given in Table 4.2. All four systems are found to be consistent with equal-mass encounters ($\mu = 1$). The orbital decay of the systems are shown in Figure 4.1. The modeling results for individual objects are discussed in the following subsections.

Assigning uncertainties to the model parameters in Table 4.2 is somewhat subjective as the model fits are essentially qualitative and done by eye. We note there may be systematic uncertainties due to mismatches between our mass models and the true



Table 4.2. Dynamical models derived from Identikit matching

System	e	p	μ	(i_1, ω_1)	(i_2, ω_2)	t	$(\theta_X, \theta_Y, \theta_Z)$	\mathcal{L} (kpc)	\mathcal{V} (km s ⁻¹)	M_{dyn} ($\times 10^{11} M_\odot$)	t_{now} (Myr)	Δt_{merge} (Myr)
NGC 5257/8	1	0.625	1	(85°, 65°)	(15°, 340°)	3.38	(126°, -3°, 63°)	34	204	9	230	1200
The Mice	1	0.375	1	(15°, 325°)	(25°, 200°)	2.75	(78°, -44°, -130°)	39.5	165	6.6	175	775
Antennae	1	0.25	1	(65°, 345°)	(70°, 95°)	5.62	(-20°, 283°, -5°)	19.7	265	8	260	70
NGC 2623	1	0.125	1	(30°, 330°)	(25°, 110°)	5.88	(-30°, 15°, -50°)	6.9	123	0.6	220	-80

Note. — e – orbital eccentricity, p – pericentric separation (simulation units), μ – mass ratio, (i_1, ω_1) (i_2, ω_2) – disk orientations (see text for description), t – time of best match (simulation units, see text for description), $(\theta_X, \theta_Y, \theta_Z)$ – viewing angle relative to the orbit plane, \mathcal{L} – length scaling factor, \mathcal{V} – velocity scaling factor, M_{dyn} – estimate of the dynamical mass, t_{now} – time since first pericenter passage, Δt_{merge} – time until coalescence based on the assumed mass model.

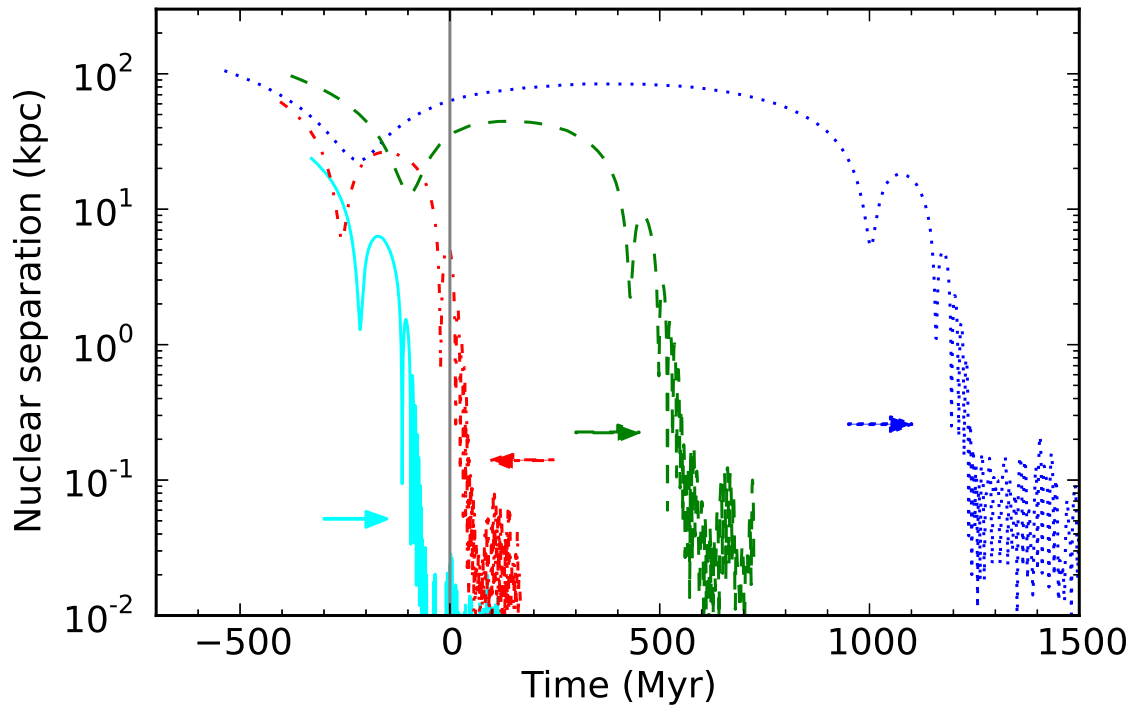


Fig. 4.1.— True nuclear separation as a function of time for NGC 5257/8 (dotted blue line), The Mice (dashed green), Antennae (dash-dot red), and NGC 2623 (solid cyan). Time of zero is the current viewing time (solid gray vertical line). The time since first passages for these systems is 175 – 260 Myr (see Table 4.2). Colored arrows mark the smoothing length in kpc for the corresponding system; this is effectively the spatial resolution of our simulations and the behavior of the curves on length scales smaller than the smoothing length is not reliable.



construction of these galaxies. Additionally, these parameters are correlated, often in nonintuitive ways. For example, selecting a later viewing time is generally compensated for with a larger pericentric separation and a change in scale factors. This will also require a modification of the viewing direction to produce the same kinematic and morphological signature. Despite these difficulties, there typically appears to be a single region of parameter space which provides a unique match. Uncertainties on the parameter values were quantified by modifying the parameters from the values in Table 4.2. Values within the range of uncertainties quoted here did not significantly degrade the fit. The vector directions of the disk spins should be accurate to within 15° ; further deviations result in significant morphological and kinematic discrepancies with observations. Similarly the viewing direction appears to have a range of 20° while still providing acceptable results. As noted above, the pericentric separation is anti-correlated with the viewing time; a factor of 2 uncertainty in p is reasonable. Once the scaling factors are included to express the time in physical units, the time since first pericenter remains relatively stable, with acceptable matches lying within a $\pm 15\%$ range. The mass ratio μ was fixed at 1, but we estimate it could vary by up to 50% for the systems modeled here.

Visualizations of the evolution of these dynamical models are available with the digital article⁹ and will also be made available through NED via object name searches.

4.4.1 NGC 5257/8

As would be inferred from visual inspection, NGC 5257/8 is an early stage merger between two massive spiral galaxies (Figures 4.2 and 4.3). The disk spin axis of NGC 5257 is nearly perpendicular to the orbital plane while the disk spin axis of NGC 5258

⁹URL to be provided by ApJ



is only moderately inclined. The best-fit disk inclinations are (85° , 65°). The system is viewed $t_{now} \sim 220$ Myr after first pericentric passage. The galaxies are approaching apocenter but have not yet reached the point of greatest separation.

The model scaling factors suggest that the total system has baryonic mass $\sim 1.8 \times 10^{11} M_\odot$ and dynamical mass of $M_{dyn} \sim 9 \times 10^{11} M_\odot$. The baryonic mass determined here is consistent with estimates from photometry and SED fitting. The disks have scale lengths of 2.8 kpc and a circular velocity of 257 km s^{-1} at 3 disk scale lengths¹⁰. The idealized Keplerian orbit is a somewhat wide passage of $p\mathcal{L} = r_{peri} = 21$ kpc (Figure 4.1).

This dynamical model reproduces the kinematics of the tidal features, particularly the eastern tidal tail. Simulating this model with a self-gravitating disk shows that this encounter geometry is additionally able to reproduce the spiral structure seen in NGC 5258, and to a lesser degree of accuracy, the spiral structure in NGC 5257 (Figure 4.4). These spiral features are generally not evident in the hybrid simulations, so they provide an extra test of a model's validity.

Roughly 30 clusters have been age dated in NGC 5257/8 using optical and UV colors obtained from HST imaging. The clusters can be broken into two populations: older, unembedded clusters whose ages are less than or equal to 240 Myr and a group of clusters with uncertain ages due to unknown reddening (Manning et al. in prep). The upper envelope of ages is similar to the first pericenter passage, suggesting these clusters were formed while the gas experienced its strongest response to tidal forces. The second population of clusters has uncertain ages, but for modest amounts of extinction ($A_V \leq 2$) these clusters would have ages of a few Myr. These are likely associated with ongoing gas compression. The clusters are predominantly located along

¹⁰This circular velocity is the value if the disk were entirely rotation supported. These disks are partially dispersion supported, so the actual circular velocity is slightly lower.



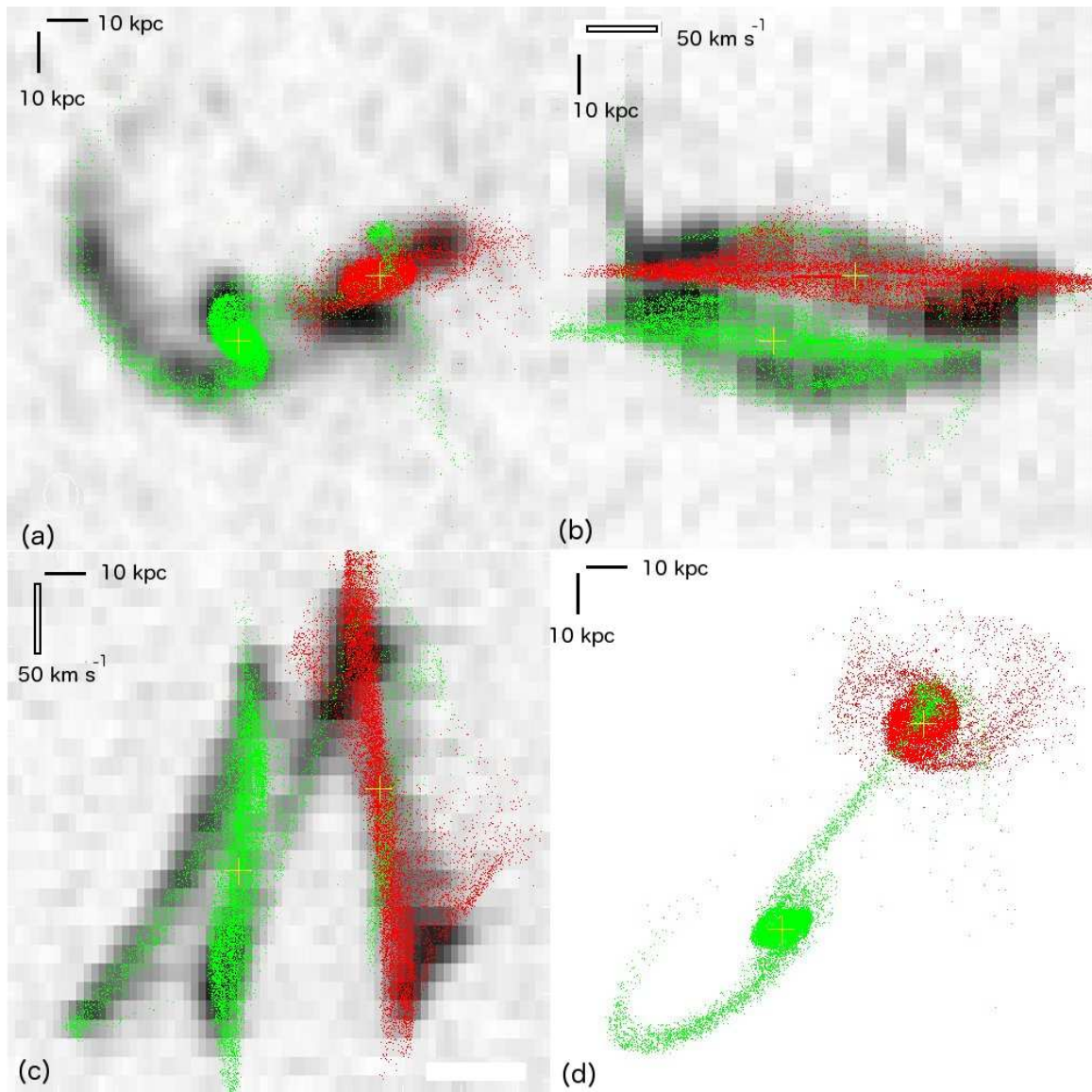


Fig. 4.2.— Identikit visualization of a self-consistent model for NGC 5257/8, matched to the system. (a): sky view of the system (α - δ), (b) PV diagram (v - δ), (c): PV diagram (α - v), and (d) “top-down” view (α , z). The sky view covers 133 kpc on a side and the velocity range is 650 km s⁻¹. In the relevant panels, the solid bar is 10 kpc and the box is 50 km s⁻¹. The HI data is shown in grayscale, with the darker pixels corresponding to higher peak values along a vector through the data cube. Red and green points show collisionless baryonic particles from N-body realizations representing the galaxies NGC 5257 and NGC 5258, respectively. The yellow crosses represent the nuclei of each N-body realization.



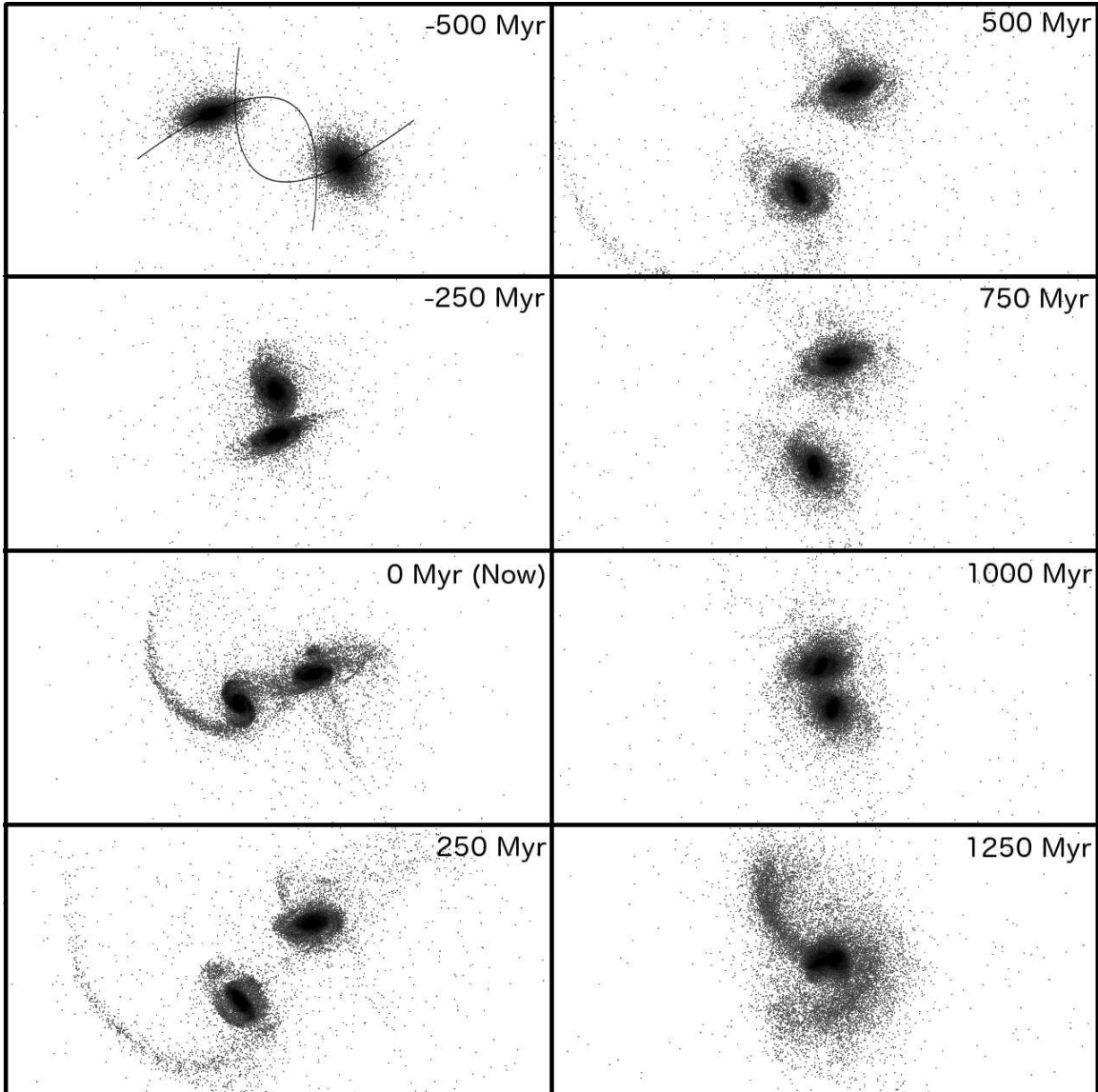


Fig. 4.3.— Snapshots of the evolution of NGC5257/8 as a function of time based on the dynamical model presented here and shown in the sky plane. The stellar distribution is shown in grayscale in 375 kpc by 240 kpc boxes. The lines in the upper-left panel show the initial Keplerian orbit projected onto the sky plane. The times shown are relative to now (see Figure 4.1).



the spiral arms in both galaxies, which have been enhanced by the tidal interaction. The close agreement of the cluster ages with the first passage and the distribution of clusters may be an interesting constraint on star formation prescriptions.

The dynamical model presented here has some minor deficiencies. For one, the short tail associated with NGC 5257 shows a greater extent in the model than is observed. This could be remedied with a smaller disk scale length. The tail associated with NGC 5258 is longer in HI than in starlight, suggesting the gas and stellar disks have different scale lengths. A more accurate mass model may also reduce the “spray” of material in this match. Such investigation of mass models would make for interesting future work.

4.4.2 The Mice

Our best match to this system has two prograde disks, both with small tilts relative to the orbital plane ($i = 15^\circ$ and 25° for NGC 4676A and NGC 4676B, respectively; Figure 4.5). The initial passage was $r_{peri} = 15$ kpc. The two galaxies have just passed for the first time and are still moving towards apocenter. The system is viewed $t_{now} = 175$ Myr after first passage and the orbital plane is viewed $\sim 20^\circ$ degrees from edge on. This, coupled with the inclination of NGC 4647A explains the northern tail’s straight appearance.

The system has baryonic mass $1.3 \times 10^{11} M_\odot$ and dynamical mass of $M_{dyn} \sim 6.6 \times 10^{11} M_\odot$. The disks have scale lengths of 3.3 kpc and circular velocities of 208 km s^{-1} at 3 disk scale lengths. The similar length of the HI and stellar tails suggests scale lengths for the gas and stellar disks are somewhat similar, though this interpretation for NGC 4676A is complicated by projection effects (the tail is seen edge on).



The observed morphology and kinematics are well matched by our dynamical model, particularly the straightness of the Northern tail and the curvature of the Southern tail. Additionally, the galaxy centers are consistent with both the nuclear positions as measured from 2MASS and the range of systemic velocities obtained from NED. Our model features some bridge material which has penetrated the disks; such material is hinted at in the deep optical images, however these features are not coincident between the model and the data. This may reflect a mass model discrepancy or be an indication that the galaxy inclinations are too low.

Comparison with Previous Models

The Mice has several previously published dynamical models. For convenience, some of the parameters from these models have been compiled in Table 4.3.

The initial model of this system by TT72 placed the orbital plane of the $e = 0.6$ orbit roughly parallel to our line of sight with a low inclination (15°) for NGC 4676A and a larger but still prograde inclination (60°) for NGC 4676B. This configuration was able to reproduce the morphology of the tails as well as the sense of the rotation velocity for the main bodies of the galaxies.

Gilbert & Sellwood (1994) built on the TT72 model by incorporating a self-consistently treated dark matter halo, finding a plausible match to the system only by assuming a $e = 1$ orbit. The disk inclinations were similar to those in TT72, but a suitable match required more time elapsed since first pericenter passage.

The TT72 model was later revised by Mihos et al. (1993) to study the effects of star formation in this system. The same disk inclinations and orbit ($e = 0.6$) were used, but match the system at an earlier time. Mihos et al. (1993) noted this has the effect of harming the match to the tidal tails but it improves the match to the main



Table 4.3. Comparison of dynamical models for the Mice

Source	e	r_{peri} (kpc)	NGC 4676A (i, ω)	NGC 4676B (i, ω)	t (Myr)	Self-consistent	3-D Match
Toomre & Toomre (1972)	0.6	...	(15°, 270°)	(60°, 270°)	120	N	Y ¹¹
Mihos et al. (1993)	0.6	23	(15°, 270°)	(60°, 270°)	180	Y	Y
Gilbert & Sellwood (1994)	1	2.25	(20°, 270°)	(40°, 270°)	260	Y	Y
Barnes (2004)	1	8.9	(25°, 330°)	(40°, 60°)	170	Y	Y
This paper	1	14.8	(15°, 325°)	(25°, 200°)	175	Y	Y

Note. — Col 1: Reference for the model. Col 2: Eccentricity of the orbit. Col 3: Pericentric separation in physical units (kpc). Col 4: (i, ω) for NGC 4676A. Col 5: (i, ω) for NGC 4676B. Col 6: Time since first pericenter passage in physical units (Myr). Col 7: Did the simulation include self-consistently modeled massive dark matter halos and stellar distributions? Col 8: Was the model constrained by three dimensional data (α, δ, v_r)? Values in physical units have not been adjusted to reflect differences in cosmology.

bodies of the galaxies. The time since pericenter is 180 Myr for this model.

As part of an effort to test numerical star formation prescriptions using The Mice, Barnes (2004) utilized a dynamical model qualitatively similar to previous efforts. The disk inclination for NGC 4676A is slightly higher (25°) while the inclination for NGC 4676B is somewhat lower (40°). Utilizing an $e = 1$ orbit, the best match to the system comes roughly 170 Myr after pericenter passage. This model reproduces the length of the tails, but the bar in NGC 4676B is misaligned relative to observations. This misalignment is not be a fatal flaw, particularly if the bar was in place before the encounter began (e.g., Barnes 2004).

A parameter space survey of the Mice by Barnes (in prep) using the Identikit 2 technique (Barnes 2011) suggests that physical values such as the time since pericenter passage remain is fairly well constrained, with essentially all acceptable matches consistent with a first passage 150–200 Myr ago, consistent with the model presented here.

In summary, our dynamical model has a similar inclination for NGC 4676A and a somewhat lower inclination for NGC 4676B than has been previously found. The time since pericenter passage (in Myr) is relatively consistent between the various models. Our model reproduces the 3D data for the system, particularly the tidal tails. Tweaks to the mass model may improve discrepancies such as the bar.

4.4.3 Antennae

Consistent with expectations from visual inspection of the tail morphology and with previous dynamical models for the system, we find an encounter geometry of two prograde disks (Figure 4.6). The disk angles are $(i, \omega) = (65^\circ, 345^\circ)$ and $(70^\circ, 95^\circ)$ for NGC 4038 and NGC 4039 respectively. The separation at first pericentric passage



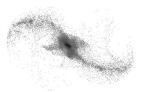
is approximately 5 kpc. The system is viewed around its second passage ($t_{now} = 260$ Myr after first passage) and the main bodies will merge in approximately 70 Myr.

The system has a total dynamical mass of $M_{dyn} \sim 8 \times 10^{11} M_{\odot}$ of which $1.6 \times 10^{11} M_{\odot}$ is baryonic. In our model, the disks of both galaxies have scale lengths of 1.5 kpc and circular velocities of 330 km s^{-1} at 3 disk scale lengths.

The dynamical model reproduces the general morphology and kinematics of both tidal tails. The hook in the Southern tail is partially reproduced, but not entirely satisfactorily. The best fit time is around 2nd pericenter passage, however there is some uncertainty regarding the precise timing (i.e., before or after 2nd passage). In these simulations the tidal tails have minor evolution over this relatively short time range, providing limited constraint on the more rapidly evolving central regions.

The modeled velocity extent in the main bodies of the galaxies is quite large (Figure 4.6), possibly extending beyond the velocity range observed in HI (though this is unclear due to the relatively narrow bandwidth of the observations, Hibbard et al. 2001). If these high velocity components originate as re-accreted tidal material, the gaseous component will likely be shocked upon its return to the disk and we would not see it in HI.

Finally, in contrast with models for the other three systems presented here, the implied circular velocity of the progenitor disks is significantly higher than typically seen in late type galaxies. It appears that this discrepancy can not be satisfactorily addressed using the mass model assumed here (i.e., there is not another region of parameter space which fits the 3D data and has a more reasonable circular velocity for the progenitors). The Antennae may reflect a system in which the actual mass configuration was sufficiently different from our assumed mass model that it has a major effect on the ability to match a dynamical model. A revised mass model may



have more success in producing a match to the data while also providing reasonable progenitor properties.

Comparison with Previous Models

Here we mention the previously published models for the Antennae. For convenience, some of the parameters from these models have been compiled in Table 4.4.

The TT72 model utilizes an encounter between two disks with the same disk orientations relative to the orbital plane $(i, \omega) = (60^\circ, 330^\circ)$. The orbit is $e = 0.5$ and the system is viewed after apocenter. The TT72 model results in equal length tails, in contrast to what is observed. Adjustments to this model by van der Hulst (1979) reduced the inferred masses of the system and the viewing time but maintained the symmetric tails.

Barnes (1988) revisited the Antenna with a simulation that included self-consistently treated dark matter halos. Both Barnes and Mihos et al. (1993) utilized the same parameters as TT72, but employ self-gravitating disks (plus gas in the latter case). The more realistic treatment of the merger results in the much more rapid decay of the orbits when compared with TT72, leading to an earlier viewing time.

Dubinski et al. (1996) modeled the system as part of an exploration of the effect of dark matter halos on the properties of tidal tails. The orbital parameters are similar to Barnes (1988) but the halo:baryonic mass ratio was varied, exploring values of 4:1, 8:1, 15:1, and 30:1. The focus of the exercise was to explore the effect of isothermal dark matter halos on tail formation, so the matches are somewhat poor. In the 4:1 and 8:1 cases sufficiently long tails are formed to be plausible for the Antennae. In the cases of 15:1 and 30:1, the tail length is considerably shorter and the tails even fall back into the progenitors before they merge. Dubinski et al. (1996) conclude the

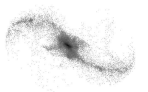


Table 4.4. Comparison of dynamical models for the Antennae

Source	e	r_{peri} (kpc)	NGC 4038 (i,ω)	NGC 4039 (i,ω)	t (Myr)	Self-consistent	3-D Match
Toomre & Toomre (1972)	0.5	...	(60°, 330°)	(60°, 330°)	150	N	N
van der Hulst (1979) ¹²	0.5	...	(60°, 330°)	(60°, 330°)	50	N	N ¹³
Barnes (1988)	1	20	(60°, 330°)	(60°, 330°)	200	N	N
Mihos et al. (1993)	0.5	27	(60°, 330°)	(60°, 330°)	210	Y	N
Dubinski et al. (1996) ¹⁴	1	...	(60°, 330°)	(60°, 330°)	...	Y	N
Hibbard & Barnes ¹⁵	1	...	(60°, 300°)	(30°, 120°)	220	Y	Y
Karl et al. (2010)	≈ 1	10.4	(60°, 30°)	(60°, 60°)	600	Y	Y
This paper	1	5	(65°, 345°)	(70°, 95°)	260	Y	Y

Note. — Col 1: Reference for the model. Col 2: Eccentricity of the orbit. Col 3: Pericentric separation in physical units (kpc). Col 4: (i,ω) for NGC 4038. Col 5: (i,ω) for NGC 4039. Col 6: Time since first pericenter passage in physical units (Myr). Col 7: Did the simulation include self-consistently modeled massive dark matter halos and stellar distributions? Col 8: Was the model constrained by three dimensional data (α,δ,v_r) ? Values in physical units have not been adjusted to reflect differences in cosmology



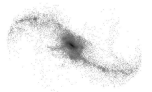
Antennae do not feature such extreme halo masses.

Karl et al. (2010) present a model which differs from previous matches to the kinematics and morphology of the system. This model matches the system at a much later time (after second passage). It has the same disk inclinations as previous matches but different arguments at pericenter. Their model implies more reasonable disk rotation values ($\sim 190 \text{ km s}^{-1}$), likely a result of the mass model adopted.

Our model has disk orientations for NGC 4038 which are consistent with early matches to the system, while the disk orientations for NGC 4039 are closer to those from Karl et al. (2010). The large difference in the time since pericenter compared to our model may be linked to a difference in mass models used; the galaxy mass models used by Karl et al. (2010) are more than twice as dark matter dominated as the models here. This, combined with a wider pericentric separation (as it relates to the disk sizes and the dark matter halo sizes) influences the orbital evolution and thus the duration of the interaction. A “mixed” simulation using the mass models from this work and the dynamical model parameters from Karl et al. (2010) was done in order to compare with their results and the results presented here. As compared with this “mixed” simulation, both the Karl et al. (2010) model and the model presented here more accurately reproduced the morphology and kinematics of the Antennae, consistent with the differing mass models being the source of the disagreement in dynamical model parameters.

4.4.4 NGC 2623

NGC 2623 shows prominent tidal tails on either side of a merger remnant. Our simulation is the first dynamical model for this system (Figures 4.7 and 4.8). The progenitor disks were both on prograde orbits, with the spin axes have a moderate



tilt relative to the orbital plane ($i = 30^\circ$ and 25° respectively). The arguments of the disk spins are $\omega = 330^\circ$ and 110° . The orbital plane itself is close to the plane of the sky and the object is viewed $t_{now} \sim 220$ Myr after first pericenter passage. The initial passage was roughly $r_{peri} = 0.8$ kpc (Figure 4.1).

Our matches require relatively compact progenitor systems, with disk scale lengths less than 1 kpc, circular velocities of 153 km s^{-1} at three scale lengths, and a dynamical mass of $M_{dyn} \sim 6 \times 10^{10} M_\odot$ for the system. Our mass model then implies a baryonic mass of $\sim 10^{10} M_\odot$. Stellar mass estimates from U et al. (2012) range from $0.9 - 2.3 \times 10^{10} M_\odot$, consistent with our estimate. We experimented with merger simulations of a 2:1 mass ratio, but generally found better agreement with the morphology and kinematics using an equal-mass encounter.

This dynamical model has the system being viewed after the nuclei have coalesced. The tidal tails are well reproduced, though the full extent of the SW tail is not reproduced. In the model, this tail does begin to curl around; it is possible that a more extended gas disk would reproduce the more extended HI emission in the tail. The velocity width of the model in the merged body is significantly wider than the HI absorption which may be due to a comparison of non-dissipational particles with a diagnostic which is inherently dissipational.

This system is being viewed after some of the tidal tail material has turned around and begun falling back into the merger remnant, as expected. In particular, a loop of material has formed south of the nucleus (Figure 4.8) from material returning from the NE tidal tail.

Many of the optically visible clusters in NGC 2623 are located just south of the nucleus. Evans et al. (2008) suggested the activity in this region was related to the return of material from the tidal tails. This prediction is consistent with the

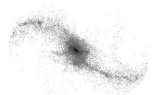


result of our simulations which show that at this point in the merger stage, the more tightly bound material in the tails (i.e., the material near the base of the tails) has already begun falling back into the remnant. While a detailed comparison requires the inclusion of gas, at this point it seems plausible that the infall of tidal material through this region is the trigger of the off-nuclear star formation; as the tails fall in, they loop around the nucleus and the off-nuclear clusters coincide with a turnaround point for the Eastern tail on its path towards the nucleus. The nuclear star formation is likely fueled by a combination of material returning from the tidal tails and gas still present in the main bodies of the galaxies during their final merger, though verification will require tests from simulations incorporating gas dynamics.

4.4.5 Future Work

The four dynamical models presented here provide both a validation of the Identikit method as applied to real data and establish the placement of these objects on a merger timeline (Figure 4.1 and Table 4.2).

Dynamical models are useful for studies of individual systems. Coupling them with a prescription (or accurate physical description) for star formation can allow one to predict the evolution of a system in different tracers of activity. Doing this for a statistically significant sample of systems can establish whether gas-rich mergers in the local Universe all undergo an Ultra Luminous Infrared Galaxy (ULIRG) phase or if such luminous objects require special progenitor properties or encounter geometries. Prescriptions of AGN feedback can potentially be tested as well, to examine the analogous question for quasar activity. The ease of matching galaxy mergers with the Identikit technique should enable the construction of samples of tens of systems with dynamical models to facilitate examination of these questions.

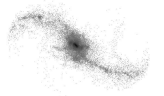


By design the self-consistent simulations presented here do not include a dissipational component. Observationally, all of these systems show elevated levels of star formation; a natural next step is to run N-body+SPH simulations to include the effects of gas. It would be instructive to see if these simulations can replicate the morphology and kinematics as determined from HI and CO observations.

A study including gas should also incorporate star formation. Star formation prescriptions in simulations are uncertain and the details can have an effect on those cosmological simulations which explicitly include gas. An accurate prescription would reproduce the observed properties of star formation in these systems. A number of options are available to compare, including global tests (e.g., the global star formation rate) and resolved tests (e.g., spatial distribution of ongoing star formation via comparison with H α or 8 μ m maps, or properties of observed star clusters).

To date, most numerical studies of star formation in mergers utilize a prescription tuned to match the Schmidt law ($\text{SFR} \propto \rho^n$, Schmidt 1959). Studies of two systems have suggested that the addition of a shock criteria to star formation prescriptions more accurately reproduces observed properties of young star clusters in merging systems (Barnes 2004; Chien & Barnes 2010, for The Mice and NGC 7252, respectively). A detailed numerical treatment of star formation by Hopkins et al. (2011b); Hopkins et al. (2013a) incorporates various feedback mechanisms in high-resolution simulations to recover the observed star formation efficiency of the Schmidt-Kennicutt Law, without tunable parameters.

The duty cycles of LIRGs and ULIRGs remains an open question — i.e., will every massive, gas-rich galaxy merger undergo a ULIRG phase? If not, what properties (orbital or galaxy structure) determine whether a merger will undergo a ULIRG phase? Answering this question is limited by the numerical treatment of star formation.



Comparing the observed star formation properties with those predicted from star formation prescriptions in detailed simulations matched to the systems may constrain these prescriptions and provide guidance for cosmological simulations. The dynamical models present here provide a useful starting point for exploring these questions.

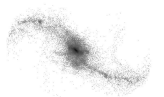
4.5 Summary

Using Identikit's hybrid simulations and visualization tool, we have obtained dynamical models for NGC 5257/8, The Mice, the Antennae, and NGC 2623 which reproduce the observed morphology and kinematics of the tidal features and place them on a merger timeline. Follow-up simulations with self-gravitating disks verify the matches and generally show agreement with self-gravitating features such as spiral arms. The dynamical models are all consistent with these systems being roughly equal mass encounters of disk galaxies involved in prograde interactions.

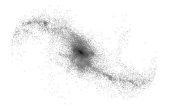
The models presented here are the first to appear in the literature for NGC 5257/58 and NGC 2623, and the new models for the Mice and the Antennae are compared with previously published models. Based on the assumed mass model and initial conditions, the results indicate the four systems are currently being viewed 175-260 Myr after first pericenter passage, and they have estimated times to coalescence of 1200 Myr (NGC 5257/58), 775 Myr (Mice), 70 Myr (Antennae) and -80 Myr (NGC 2623). Future simulations incorporating gas will be used to test numerical prescriptions of star formation.

Acknowledgements

The authors thank Francois Schweizer for helpful comments on the manuscript. The authors also thank the anonymous referee for useful comments. G.C.P. and A.S.E.



were supported by NSF grants AST 1109475 and 02-06262, and by NASA through grants HST-GO10592.01-A and HST-GO11196.01-A from the Space Telescope Science Institute, which is operated by the Association of Universities for Research in Astronomy, Inc., under NASA contract NAS5-26555. This research has made use of the NASA/IPAC Extragalactic Database (NED) which is operated by the Jet Propulsion Laboratory, California Institute of Technology, under contract with the National Aeronautics and Space Administration. This research has made use of NASA's Astrophysics Data System. The National Radio Astronomy Observatory is a facility of the National Science Foundation operated under cooperative agreement by Associated Universities, Inc.



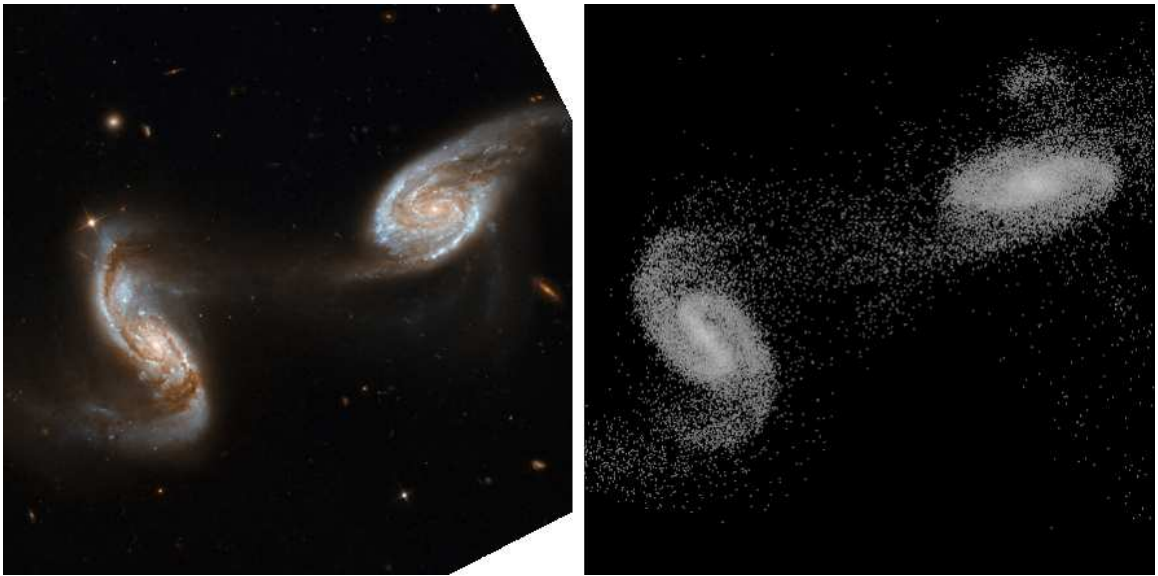
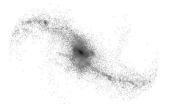


Fig. 4.4.— Left: HST/ACS color image of NGC 5257/8 from Evans et al. (*in prep*). Right: N-body realization of the stellar distribution from the dynamical model presented here. Note the general correspondence between the spiral features in the simulation and the observations.



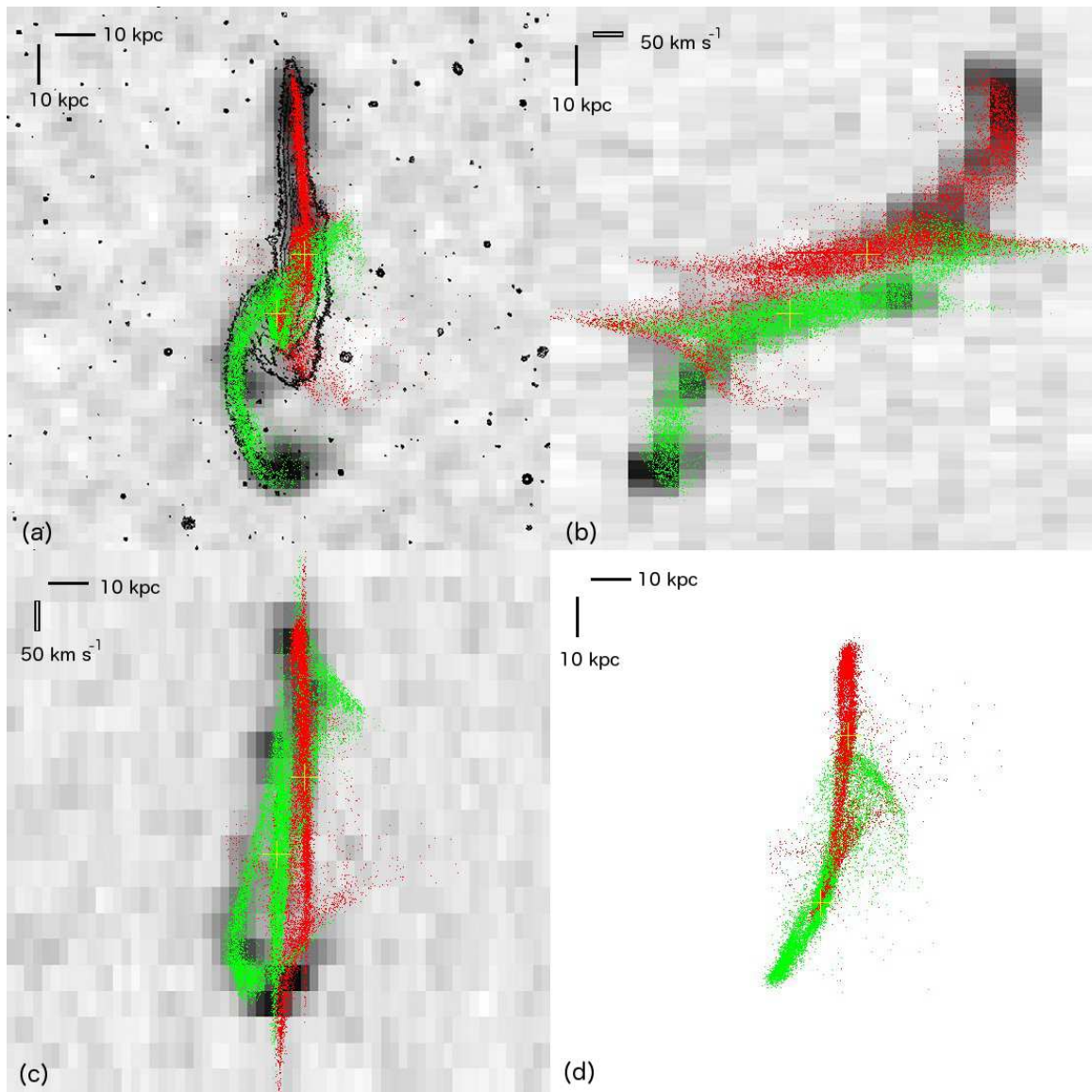
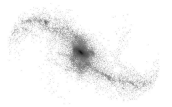


Fig. 4.5.— Identikit visualization of a self-consistent model for The Mice, matched to the system. (a): sky view of the system (α - δ), (b) PV diagram (v - δ), (c): PV diagram (α - v), and (d) “top-down” view (α , z). Here, the sky view is 138 kpc on a side and the velocity width is 903 km s^{-1} . In the relevant panels, the solid bar is 10 kpc and the box is 50 km s^{-1} . In the sky view the contours show the R-band image from Hibbard & van Gorkom (1996). Red and green points correspond to stellar particles from N-body realizations representing NGC 4676A and NGC 4676B, respectively. The yellow crosses denote the nuclei of the N-body realizations.



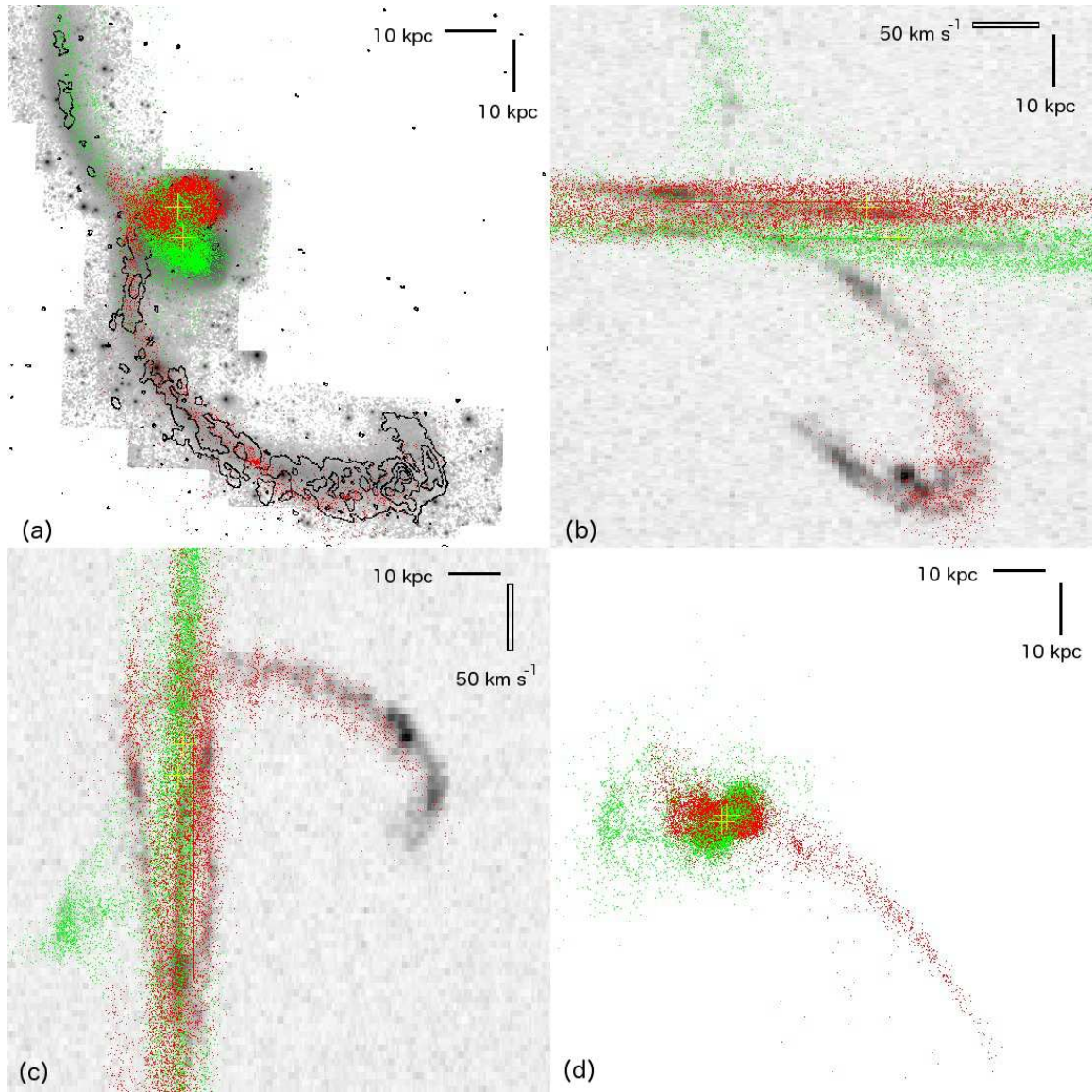
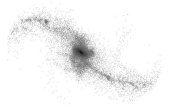


Fig. 4.6.— Identikit visualization of a self-consistent model for the Antennae, matched to the system. (a): sky view of the system (α - δ), (b) PV diagram (v - δ), (c): PV diagram (α - v), and (d) “top-down” view (α , z). The sky view shows HI contours over a V band image, both from Hibbard et al. (2001); it is 105 kpc on a side. The position velocity diagrams are the maximum pixel of the relevant projection of the cube, with darker pixels corresponding to higher peak emission levels. The velocity width is 410 km s^{-1} . In the relevant panels, the solid bar is 10 kpc and the box is 50 km s^{-1} . Red and green dots correspond to stellar particles from N-body realizations of NGC 4038 and NGC 4039, respectively. The yellow crosses denote the nuclear positions of the N-body realizations.



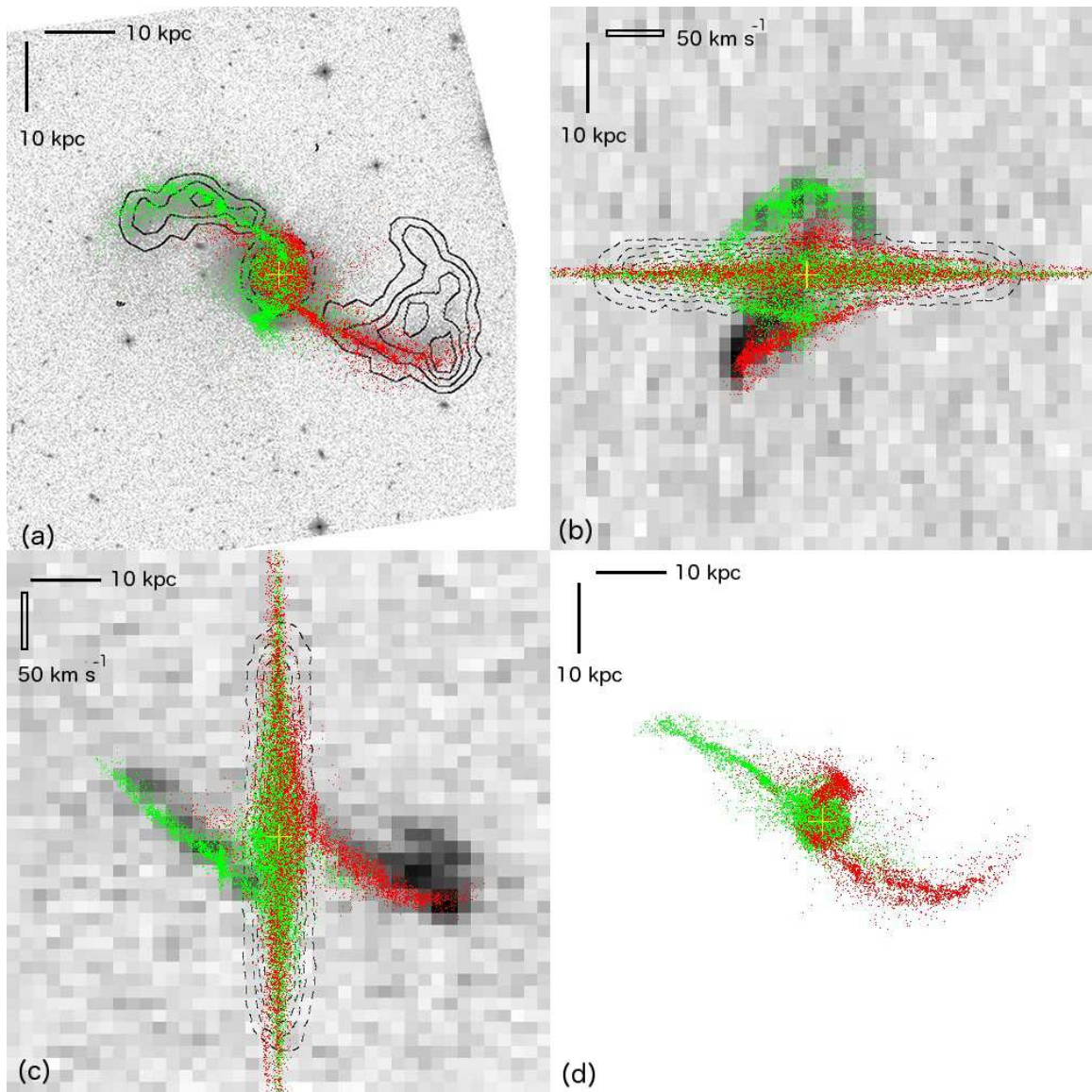


Fig. 4.7.— Identikit visualization of a self-consistent model for NGC 2623, matched to the system. (a): sky view of the system (α - δ), (b) PV diagram (v - δ), (c): PV diagram (α - v), and (d) “top-down” view (α , z). The sky view shows the HST F814W image in grayscale (Evans et al. 2008) and the HI in contours; it covers 77 kpc. The position velocity diagrams show the HI emission in grayscale and the HI absorption is shown as dashed contours. The velocity width is 470 km s^{-1} . In the relevant panels, the solid bar is 10 kpc and the box is 50 km s^{-1} . Red and green points correspond to stellar particles from N-body realizations of the two progenitor systems for NGC 2623 and the yellow cross denotes the nuclei of the N-body realizations.

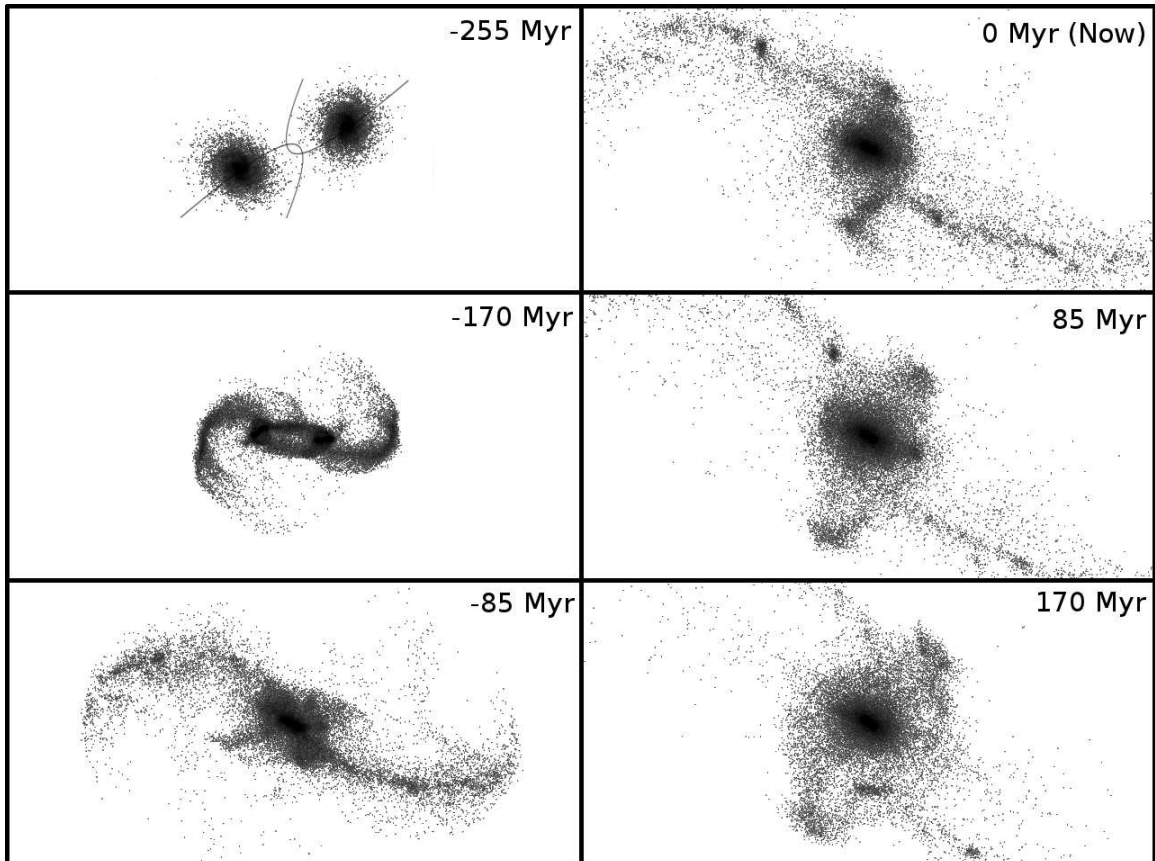


Fig. 4.8.— Snapshots of the evolution of NGC 2623 as a function of time, based on the dynamical model presented here and shown in the sky plane. The stellar distribution is shown in grayscale in 75 kpc by 50 kpc boxes. The grey lines show the initial Keplerian orbits of the galaxies projected onto the plane of the sky. The times shown are relative to now (see Figure 4.1).

Chapter 5

Dynamical Modeling of Galaxy Mergers Using Identikit. II: Star Formation, Active Galactic Nuclei, and Merger Stage Classification

5.1 Introduction

Interactions between galaxies are understood to be an integral aspect of galaxy evolution (e.g. Springel et al. 2005); they drive the transformation of disk galaxies into elliptical galaxies (e.g., Toomre 1977; Barnes 1992). Broad observational and theoretical support are in place for this scenario (e.g., Toomre & Toomre 1972; Sanders et al. 1988; Barnes 1992; Barnes & Hernquist 1996; Hopkins et al. 2008), but uncertainties remain in our understanding of interaction-driven galaxy-scale star formation (e.g., Barnes 2004; Chien & Barnes 2010; Hopkins et al. 2013b) and hence, our understanding of how the stellar mass mass of galaxies is built up. Detailed comparisons between

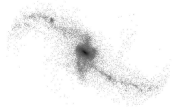
simulations and observations of individual galaxy mergers to place more constraints on models.

Identikit (Barnes & Hibbard 2009, hereafter BH09) has enabled rapid matching of dynamical models to observations of disk-disk mergers. We have previously demonstrated the effectiveness and accuracy of this technique (Chapter 4; Privon et al. 2013, hereafter “Paper I”). Extending the sample of systems with matched dynamical models will provide a useful resource for comparisons with simulations, and it will also allow us to put derived observable quantities (e.g., star formation rates, stellar ages) in the proper temporal context of merger-driven activity.

Dynamical models are presented for one Ultraluminous Infrared Galaxy (ULIRG; $L_{\text{IR}} \geq 10^{12} L_{\odot}$) and two Luminous Infrared Galaxies (LIRG; $10^{11} \leq L_{\text{IR}}/L_{\odot} < 10^{12}$), from the Great Observatories All-Sky LIRG Survey (GOALS, Armus et al. 2009). Partially successful models for two additional systems and prospects for modeling of a further two systems are also discussed. None of the systems have previously published dynamical models. Section 5.2 describes the properties of the sample, Section 5.3 briefly summarizes the matching process, Section 5.4 presents the dynamical models, and Section 5.5 investigates galaxy properties from various GOALS studies as a function of the determined merger stages.

5.2 The Sample and Data

This sample is a subset of U/LIRGs from the GOALS multi-wavelength survey. The ancillary data available through GOALS provides information on star formation rates (Howell et al. 2010; U et al. 2012), star cluster populations (Vavilkin et al. *in prep*), nuclear activity (Iwasawa et al. 2009; Petric et al. 2011; Stierwalt et al. 2013; Inami et al. 2013), gas properties (Stierwalt et al. 2013), and galaxy structural properties



(Haan et al. 2011; Kim et al. 2013), lending significant additional value to obtaining dynamical models for these merging systems.

The limiting factor in producing dynamical models is obtaining wide-field kinematic information for the systems, particularly for tidal features. Typically this information is obtained using HI data cubes under the assumption that tidal features have similar stellar and gas kinematics. Tidal forces have a similar effect on both the stars and gas, so their large-scale evolution will be similar, supporting the validity of this assumption. Thus we select a subset of (U)LIRGs from GOALS which have high-quality interferometric HI observations. The HI data is taken from Fernández et al. (2010, NGC 34), English et al. (2003, NGC 3256), J. Hibbard & A. Evans (*priv. comm.*, NGC 4418), Yun & Hibbard (*priv. comm.*, NGC 6240), or (Hibbard & Yun 1996, Mrk 273, IC 883, and NGC 1614). Properties of the HI data cubes are provided in Table 5.2. Optical images were obtained from the Second Digitized Sky Survey (Red) (Mrk 273 and NGC 3256; McLean et al. 2000), the University of Hawaii 88" (R-band; IC 883 and NGC 1714; J. Hibbard *priv. comm.*), and the Advanced Camera for Surveys on the Hubble Space Telescope (NGC 34 and NGC 6240; A. S. Evans *in prep.*).

5.3 Matching of Dynamical Models

The procedure for constraining dynamical models using Identikit is briefly summarized below, but for full details of the matching process and subsequent self-consistent verification, see Paper I or Chapter 4.

Dynamical models are first constrained using hybrid test particle and N -body simulation (BH09). Simulated test particle distributions were compared with the morphology and position-velocity diagrams obtained from optical and HI observa-

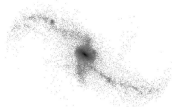


Table 5.1. Dynamical Modeling Sample Description, Pt. II

Source	Other Names	z	D_L (Mpc)	$\log(L_{IR}/L_{\odot})$
Mrk 273	UGC 08696, VV 851, IRAS 13428+5608	0.03778	173	12.21
IC 883	UGC 08387, VV 821, IRAS 13183+3423, ARP 193	0.0233	110	11.73
NGC 1614	IRAS F043150840, ARP 186, Mrk 617	0.0159	67.8	11.65
NGC 34	NGC 17, VV 850, IRAS F000851223, Mrk 938	0.0960	84.1	11.49
NGC 3256	VV 65, IRAS 10257-4338	0.009354	38.9	11.64
NGC 4418	UGC 07545, IRAS 12243-0036	0.007	36.5	11.19
NGC 6240	UGC 10592, VV 617, IRAS 16504+0228	0.024	116	11.93

Note. — Col 1: Source name as adopted this paper. Col 2: Alternate source names. Col 3: redshift obtained from NED. Col 4: Luminosity distance in Mpc from Armus et al. (2009). Col 5: Log of the infrared luminosity in solar luminosities from Armus et al. (2009).



tions, and the encounter parameters were varied until an acceptable match to the large scale kinematic features was found. Where possible, rough parameter values were estimated from the available data (e.g., mass ratios from ratios of integrated galaxy luminosities, sense of disk rotation by the presence/absence and length of tidal tails) prior to attempting to match test particle models.

In order to refine a model, further N -body simulations were run including self-gravitating disks. Sometimes small adjustments to parameters were needed. These simulations were also used to ensure that self-gravitating features (which are not expected to be reproduced in the hybrid simulations) are reproduced by the dynamical model.

The constrained parameters of each dynamical model include orbital parameters (e – orbital ellipticity, μ – mass ratio of the galaxies, p – pericentric separation¹), initial disk orientation parameters (one pair per galaxy; i – disk inclination relative to the orbital plane, ω – longitudinal orientation²), and viewing parameters (t – time of viewing³), $(\theta_X, \theta_Y, \theta_Z)$ – viewing angle to the orbital plane, \mathcal{L} – length scaling, \mathcal{V} – velocity scaling). \mathcal{L} and \mathcal{V} can then be combined to determine time ($\mathcal{T} \propto \mathcal{L}/\mathcal{V}$) and mass scalings ($\mathcal{M} \propto \mathcal{V}^2 \mathcal{L}$). The remaining parameters specify the location of the system’s center of mass (X, Y, v_r) .

5.4 Modeling Results

Dynamical models were satisfactorily matched to three systems: Mrk 273, IC 883, and NGC 3256 (Table 5.3, Figures 5.1–5.5). For these objects, a set of parameters

¹Values quoted here are the pericentric separation for an idealized keplerian orbit for point masses.

²Defined for an idealized Keplerian orbit, where this value is the longitudinal argument relative to the line of nodes at the idealized pericenter separation; see Toomre & Toomre (1972), their Figure 6a.

³As in Paper I (Chapter 4), $t=2.0$ is set as the time of first pericentric passage.

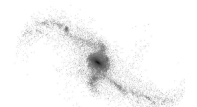


were found which adequately reproduce the observed morphology and kinematics of the system. For two other systems (NGC 34 and NGC 1614), partial models are presented; these match the morphology and kinematics of the system, albeit with some deficiencies (Figures 5.7 and 5.8). Finally, modeling prospects are discussed for two other systems (NGC 4418 and NGC 6240). As described in Paper I (Chapter 4), the matching process is somewhat subjective and uncertainties were determined empirically.

Figures 5.1–5.8 show the dynamical models overlaid on morphological and kinematic constraints in four panels. In all four panels, N-body or test particle points from the progenitor disks are shown as colored points (with each color corresponding to a different progenitor). The four panels display the following projections: (a) sky-plane view of the system, $\alpha - \delta$, (b) position-velocity diagram, $v - \delta$, (c) position velocity diagram $\alpha - v$, and (d) “top down” view of the system, $\alpha - z$. Panels (a)–(c) contain morphological and kinematic constraints from optical imaging and HI observations. The particulars for each system are given in the figure captions. For the three systems with reliable models, the modeled orbital evolution is plotted in Figure 5.10.

5.4.1 Mrk 273

Markarian 273 was produced by an interaction between a disk with a prograde orientation (disk angular momentum vector aligned with the orbital angular momentum vector; $i = 55^\circ$) and one with a slightly retrograde orientation (disk angular momentum vector anti-aligned with the orbital angular momentum vector; $i = 110^\circ$; Figure 5.1). The prograde system forms the prominent southern tail while the retrograde disk gives rise to the NE plume. With our assumed mass model, the system has a dynamical mass of $\sim 3 \times 10^{11} M_\odot$ of which $\sim 6 \times 10^{10} M_\odot$ is baryonic. The disks

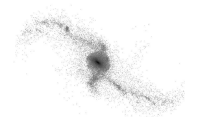


have scale lengths of 0.8 kpc and circular velocities of 280 km/s at $R = 2.4$ kpc (3 disk scale lengths). The first passage of the galaxies occurred at a separation of roughly 2.5 kpc (3 disk scale lengths) approximately 180 Myr ago. Our model was constrained by observations to select a t for which The nuclei have not yet merged; but our model suggests the nuclei will merge in a relatively short amount of time (40 Myr). This model places the southern tidal tail extending towards us from the main body of the galaxy, consistent with the finding of Iwasawa et al. (2011) that this tail is “shadowing” the soft X-ray emission of this system. Figure 5.2 shows the morphological evolution of this system.

The velocity scaling (and hence the mass and time scaling) for this system is somewhat uncertain owing to the lack of velocity information on the northern plume. In the VLA observations, no HI emission is detected coincident with the plume (Hibbard & Yun 1996), possibly due to surface brightness sensitivity limitations. Additionally, the constraints on the systemic recession velocity do not provide tight constraints on the nuclei. Thus the velocity scale factor is uncertain by 30%, resulting in an uncertainty in the mass scaling factor of 70%. The velocity scale factor quoted in Table 5.3 was determined by requiring the kinematics of the Southern tail to be well-matched by the model and by requiring the velocity width of the main body of the system did not significantly exceed the width of the observed HI absorption (see Figure 5.1). Kinematic constraints on the Northeast plume from stellar absorption lines could improve the determination of these scale factors.

5.4.2 IC 883

The dual-tail morphology of IC 883 results from the interaction of two disk galaxies with prograde orientations ($i = 65^\circ$ and $i = 60^\circ$; Figure 5.3). The system is viewed



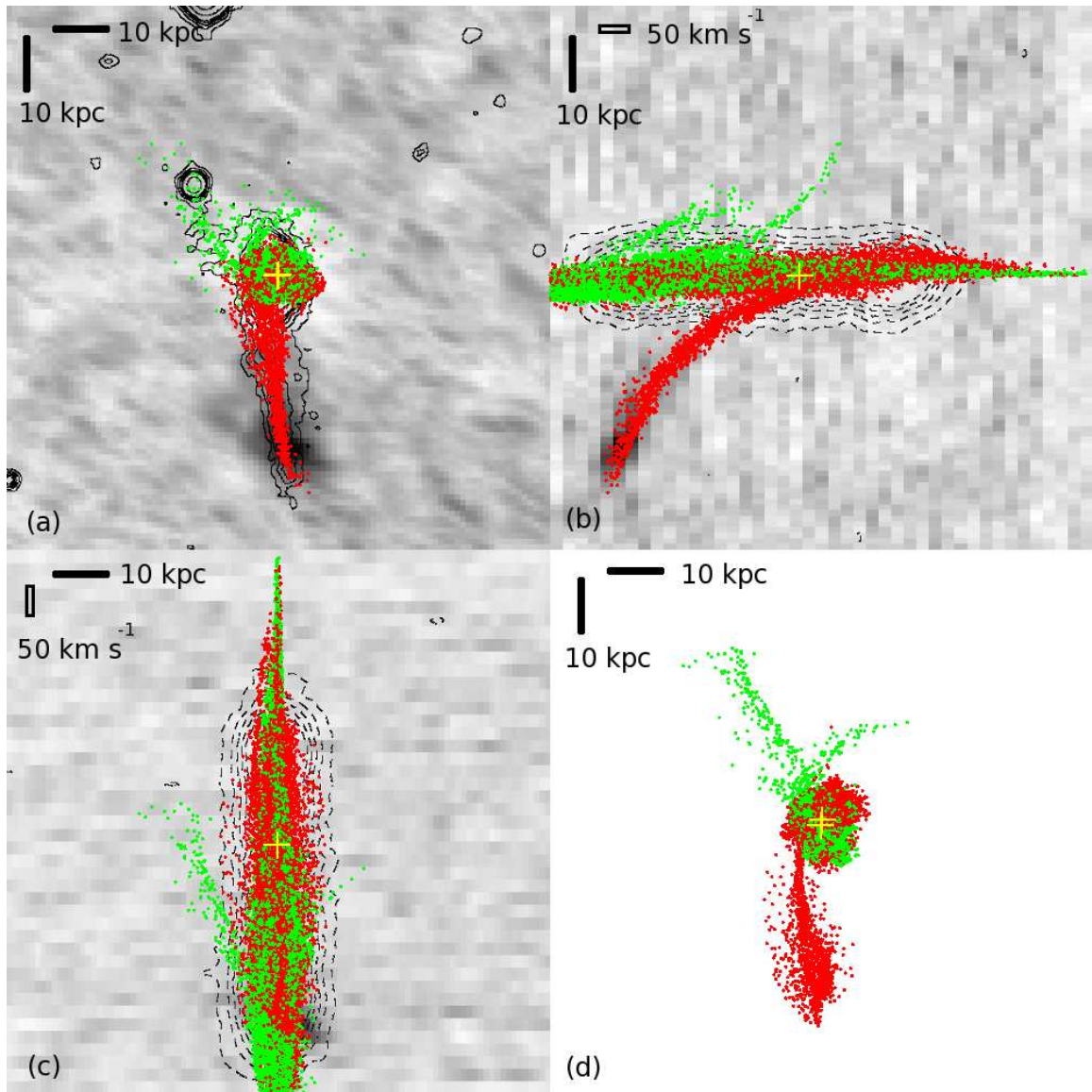


Fig. 5.1.— Identikit visualization of a self-consistent model for Mrk 273, matched to the system. (a): sky view of the system ($\alpha - \delta$), (b) PV diagram ($v - \delta$), (c): PV diagram ($\alpha - v$), and (d) “top-down” view ($\alpha - z$). The sky view covers 105.6 kpc on a side and the velocity range is 920 km s^{-1} . In the relevant panels, the solid bar is 10 kpc and the box is 50 km s^{-1} . In all panels the HI data is shown in grayscale, with the darker pixels corresponding to higher peak values along a vector through the data cube. In panel (a), a DSS2 Red image is overlaid in contours. Red and green points show collisionless baryonic particles from N-body realizations representing the two progenitor galaxies. The yellow crosses represent the nuclei of each N-body realization.

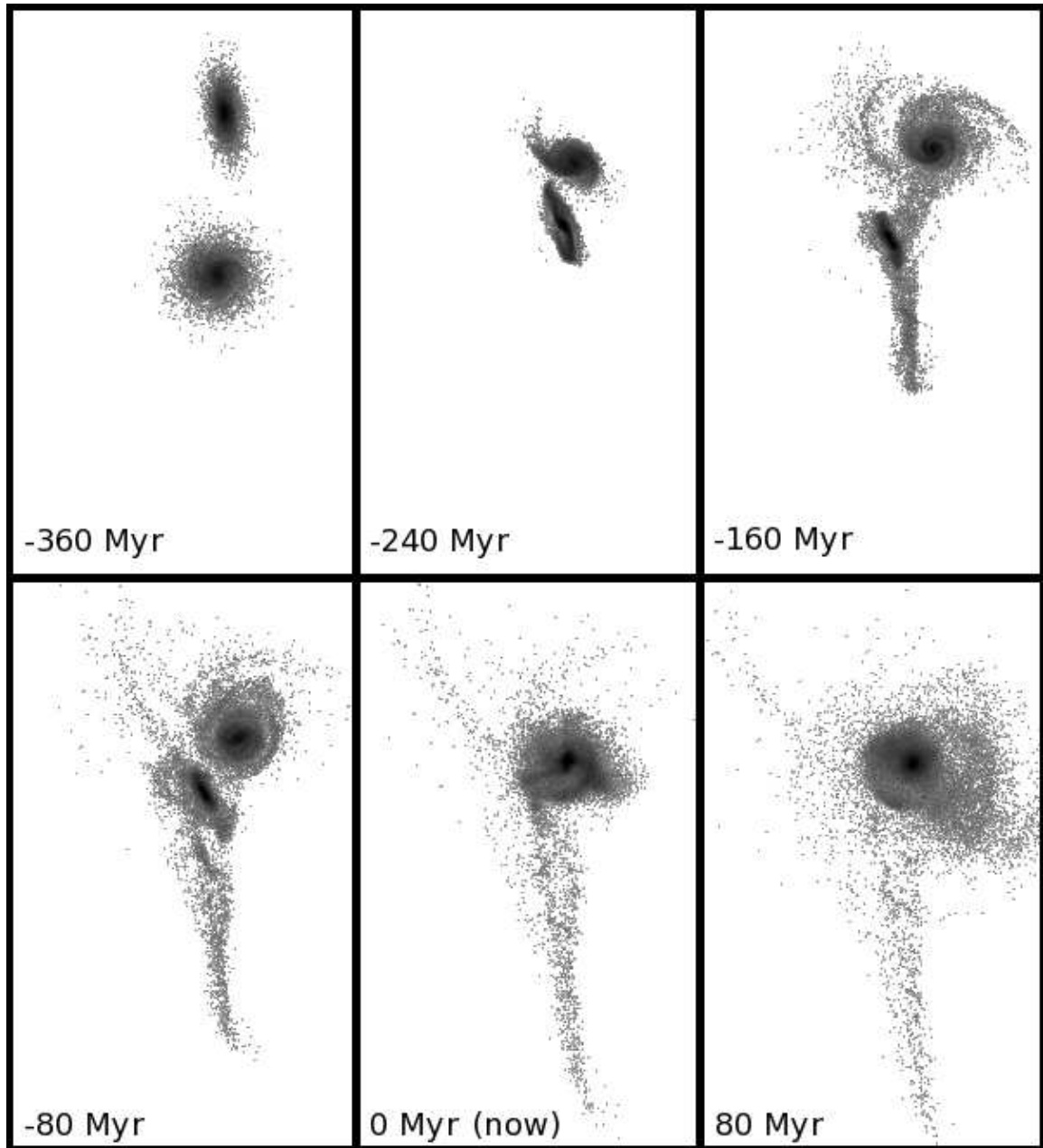


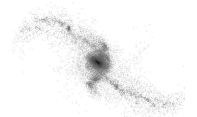
Fig. 5.2.— Snapshots of the evolution of Mrk 273 as a function of time, based on the dynamical model presented here, and shown in the sky plane. The stellar distribution is shown in grayscale. The times are shown relative to now (see Figure 5.10).

280 Myr after the first pericenter passage of 2.5 kpc (4.5 disk scale lengths). The progenitor galaxies were relatively low mass and the system has a total dynamical mass of $7 \times 10^{10} M_{\odot}$ and a baryonic mass of $\sim 1.4 \times 10^{10} M_{\odot}$. Figure 5.4 shows the morphological evolution of the system.

This dynamical model reproduces the overall morphology and kinematics of the system. The SW tail loops around the main body of the remnant and results in the slight NE extension seen at low surface brightness. The model has two small mismatches, having to do with each end of the tidal tails. The modeled SE tail is not as straight as is seen in optical imaging, while the model does not quite reproduce the hook at the end of the SW tail. Reproducing these features depends quite sensitively on the disk inclinations and the viewing direction – the small tweaks that would be needed to refine these are likely not reliable in light of the uncertainties due to the assumed mass model.

5.4.3 NGC 3256

This system has no previously published dynamical models, but a study of the HI data suggested the system is roughly an equal-mass encounter (English et al. 2003). The presence of dual tails is consistent with both progenitor galaxies having prograde disk orientations. The presented dynamical model (Figure 5.5) is consistent with these earlier suggestions, featuring the encounter of two roughly equal-mass galaxies with prograde disk orientations ($i = 60^{\circ}$ disk resulting in the east tail, $i = 5^{\circ}$ disk leading to the western tail). The system is near second passage and has not yet merged, consistent with evidence from radio observations that the system has two nuclei (Norris & Forbes 1995). Based on the model, the system has a total mass of $10^{11} M_{\odot}$ and a baryonic mass of $2 \times 10^{10} M_{\odot}$. Figure 5.6 shows the morphological



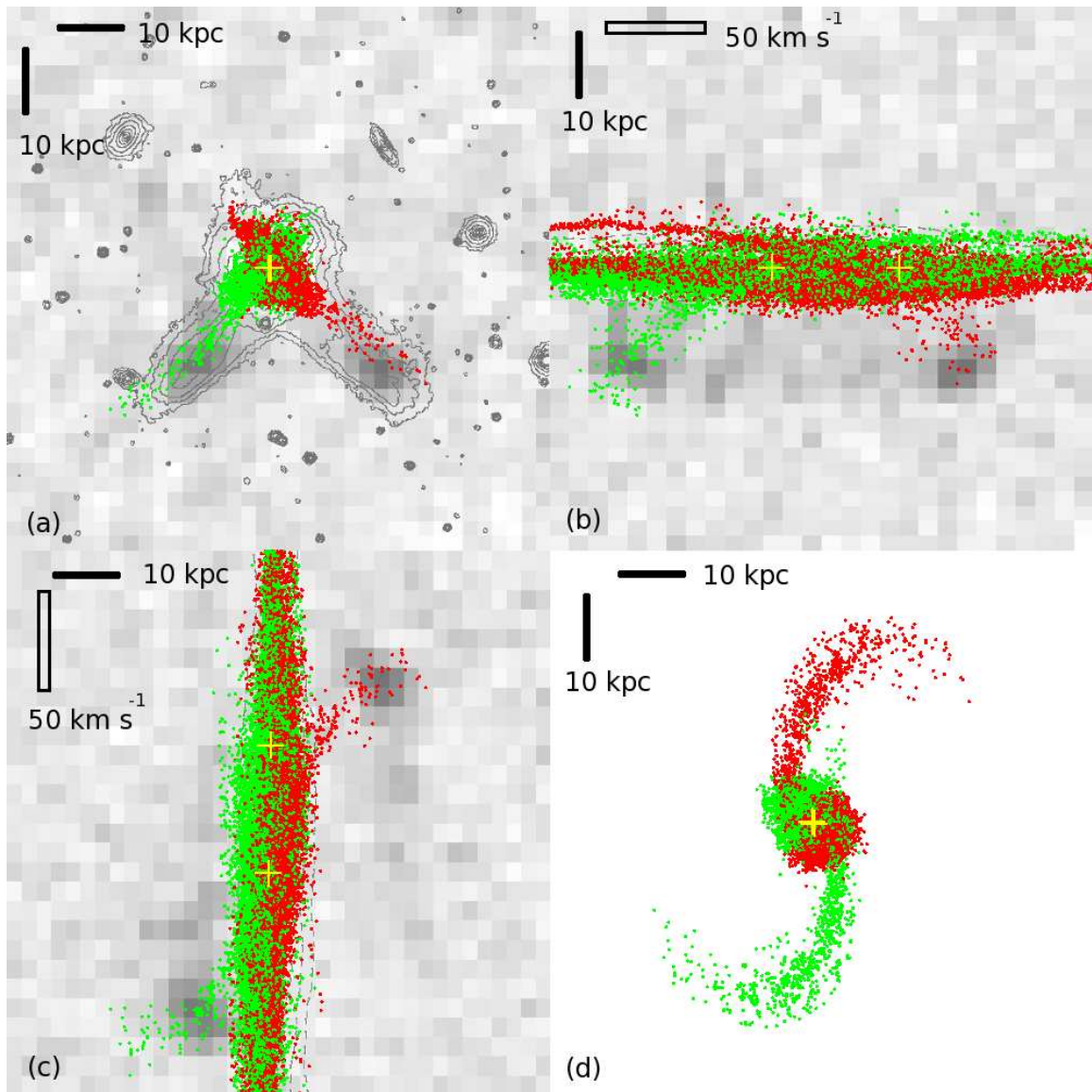


Fig. 5.3.— Identikit visualization of a self-consistent model for IC 883, matched to the system. (a): sky view of the system ($\alpha - \delta$), (b) PV diagram ($v - \delta$), (c): PV diagram ($\alpha - v$), and (d) “top-down” view ($\alpha - z$). The sky view covers 86 kpc on a side and the velocity range is 295 km s^{-1} . In the relevant panels, the solid bar is 10 kpc and the box is 50 km s^{-1} . In all panels the HI data is shown in grayscale, with the darker pixels corresponding to higher peak values along a vector through the data cube. In panel (a), a DSS2 Red image is overlaid in contours. Red and green points show collisionless baryonic particles from N-body realizations representing the two progenitor galaxies. The yellow crosses represent the nuclei of each N-body realization.

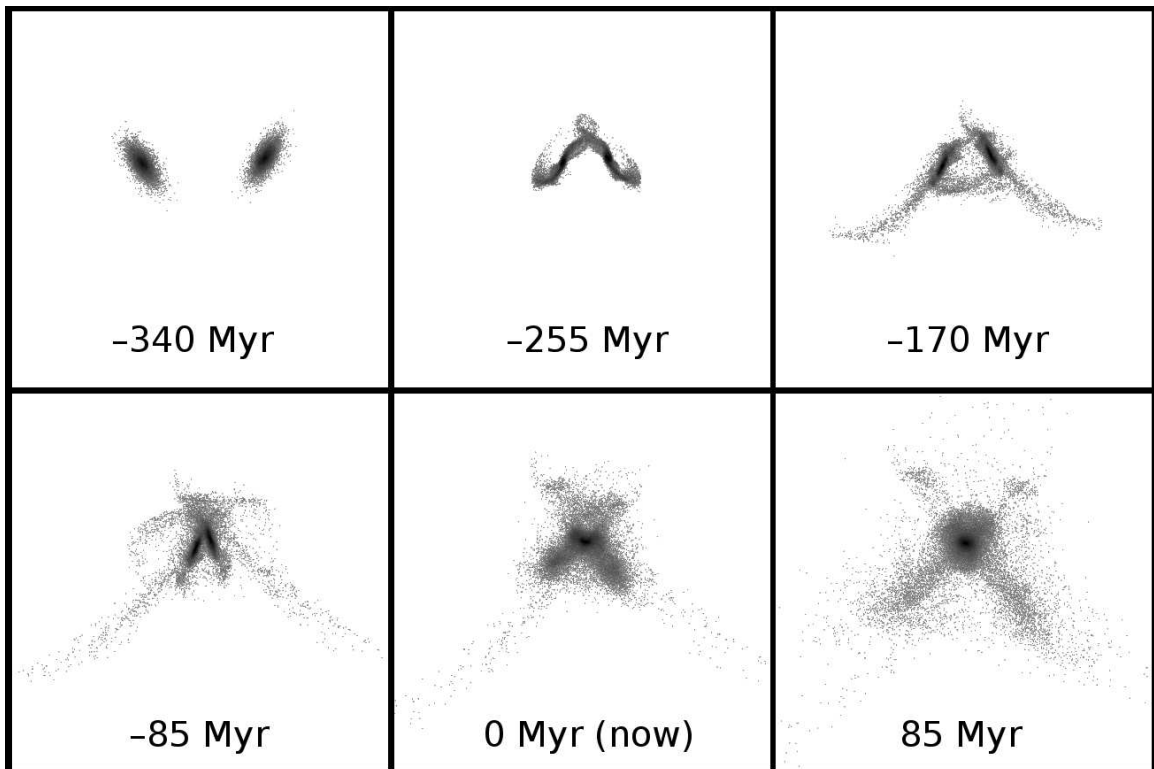
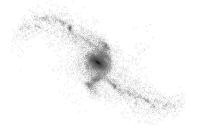


Fig. 5.4.— Snapshots of the evolution of IC 883 as a function of time, based on the dynamical model presented here, and shown in the sky plane. The stellar distribution is shown in grayscale. The times are shown relative to now (see Figure 5.10).



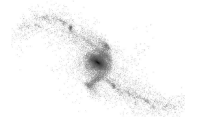
evolution of the system.

The model reproduces the most well-defined aspects of the tidal material (the prominent tails) but does not explain the more extended low column H I emission seen in maps of the system (English et al. 2003). The origin of these clumps is unclear, but it does not seem that a simple galaxy encounter model can explain their origin. This model also has a slight discrepancy in the velocity structure of the eastern tail, with an offset of $\sim 50 \text{ km s}^{-1}$ between the H I velocities and the model predictions and a steeper velocity gradient in the modeled tail, compared to the data.

5.4.4 NGC 34

This merger remnant (Schweizer & Seitzer 2007) appears to be the product of an encounter between a prograde disk ($i = 70^\circ$, giving rise to the prominent NE tail) and a disk with a prograde spin ($i = 80^\circ$, resulting in the fainter southern stellar tail). The initial passage for this system was 1.5 disk scale lengths and occurred roughly 185 Myr ago. The close passage resulted in the system merging very recently (in a time range shorter than our estimated uncertainties on the system age).

While this model reproduces the morphology of both tails and the kinematics of the northern tail, there are two issues to note. First, the H I “halo” around the remnant is not populated by particles from the simulations. It is possible this halo is the result of an extended H I disk, but this might require more extended northern H I emission relative to the extent of the stars (see Arp 240, Paper I); however this scenario would not be consistent with the observations. This halo also gives rise to the velocity component which is not matched by this dynamical model. As this H I halo is not directly associated with the observed stellar tail, the associated kinematic is not used as a constraint on the model. Additionally, the main body of the modeled remnant



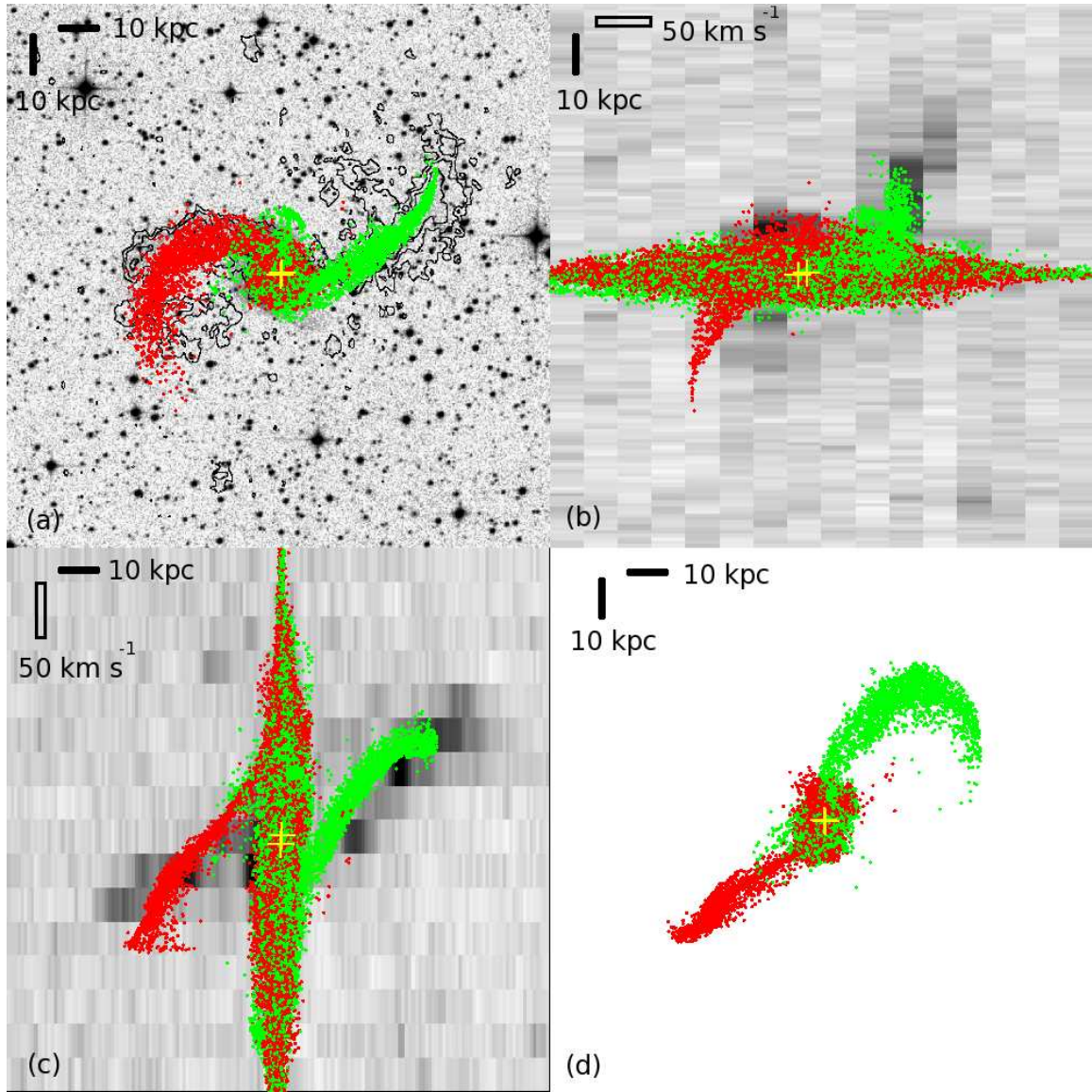


Fig. 5.5.— Identikit visualization of a self-consistent model for NGC 3256, matched to the system. (a): sky view of the system ($\alpha - \delta$), (b) PV diagram ($v - \delta$), (c): PV diagram ($\alpha - v$), and (d) “top-down” view ($\alpha - z$). The sky view covers 145.8 kpc on a side and the velocity range is 495.4 km s^{-1} . In the relevant panels, the solid bar is 10 kpc and the box is 50 km s^{-1} . In all panels the HI data is shown in grayscale, with the darker pixels corresponding to higher peak values along a vector through the data cube. In panel (a), a DSS2 Red image is overlaid in contours. Red and green points show collisionless baryonic particles from N-body realizations representing the two progenitor galaxies. The yellow crosses represent the nuclei of each N-body realization.

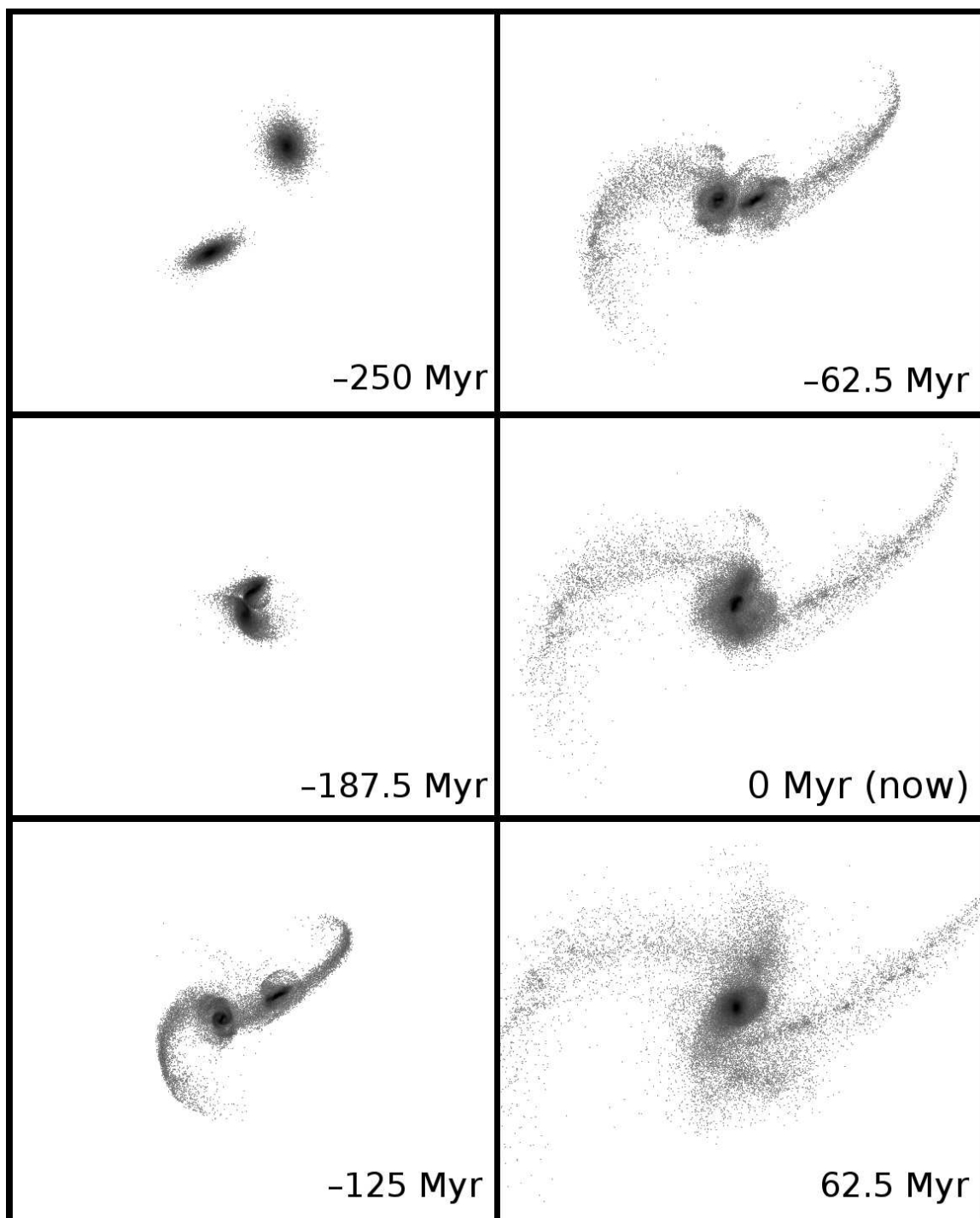


Fig. 5.6.— Snapshots of the evolution of NGC 3256 as a function of time, based on the dynamical model presented here, and shown in the sky plane. The stellar distribution is shown in grayscale. The times are shown relative to now (see Figure 5.10).

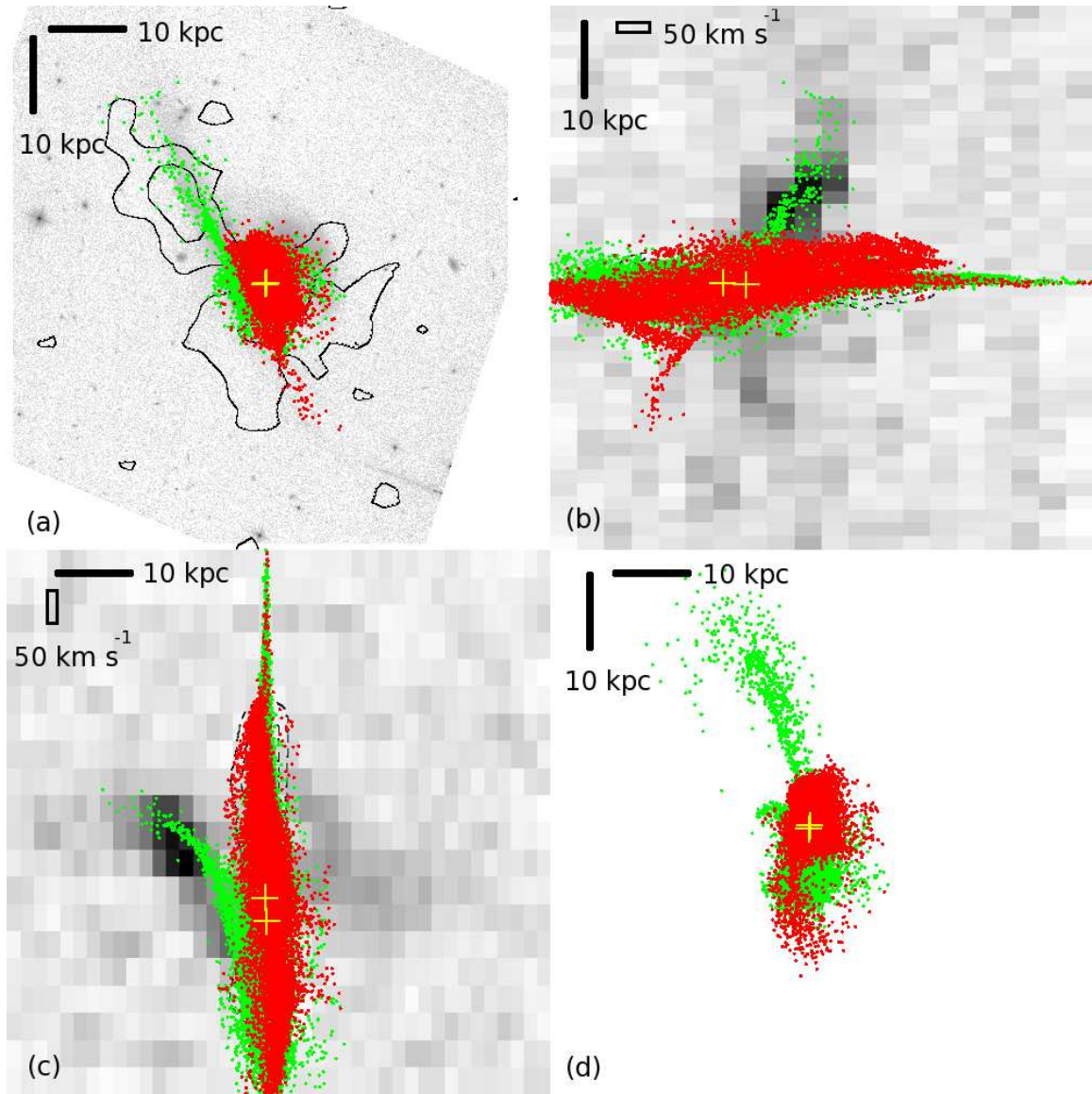
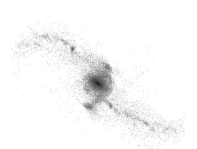


Fig. 5.7.— Identikit visualization of a self-consistent model for NGC 34, matched to the system. (a): sky view of the system ($\alpha - \delta$), (b) PV diagram ($v - \delta$), (c): PV diagram ($\alpha - v$), and (d) “top-down” view ($\alpha - z$). The sky view covers 76.6 kpc on a side and the velocity range is 839 km s^{-1} . In the relevant panels, the solid bar is 10 kpc and the box is 50 km s^{-1} . Panel (a) shows HI contours overlaid on a HST/ACS F814W image. In panels (b) and (c) the HI data is shown in grayscale, with the darker pixels corresponding to higher peak values along a vector through the data cube. Red and green points show collisionless baryonic particles from N-body realizations representing the two progenitor galaxies. The yellow crosses represent the nuclei of each N-body realization.



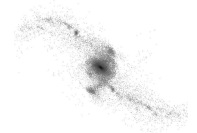
appears to be a bit too edge-on, when compared to the optical images. However, the simulations trace the baryonic mass directly, while the optical morphology can be affected by the ongoing or recent star formation. Given these two discrepancies, the dynamical model presented here is considered “in progress”.

Previous Dynamical Constraints

NGC 34 has a large stellar disk with an age of 400 Myr (Schweizer & Seitzer 2007), which accounts for roughly $2\text{--}3 \times 10^9 M_{\odot}$ of the total system mass of $3 \times 10^{10} M_{\odot}$ (U et al. 2012). As the K-band morphology shows no evidence for a disk, this suggests the merger event was a major merger, leading to the destruction of the progenitor disks and the 400 Myr disk is a new disk built up during the encounter (see Barnes 2002). Schweizer & Seitzer (2007) argue the asymmetry in the integrated brightness of the tidal tails precludes this merger being equal-mass, so they estimate a mass ratio between 1:3 and 2:3. The balance of evidence appears to be in favor of this system being a merger remnant, where the two nuclei have already coalesced. The system’s high rotational support and disk-like isophotal shape (Rothberg & Joseph 2006) are consistent with results from simulations that major but not equal-mass mergers should result in this type of merger remnant (Naab & Trujillo 2006).

5.4.5 NGC 1614

Figure 5.8 shows a test particle approximation to NGC 1614, consisting an equal-mass encounter between two disks, the first with a retrograde spin ($i = 105^{\circ}$) and the second with a prograde spin ($i = 20^{\circ}$). The latter disk gives rise to both the long northern tail and to the shorter linear feature to the southwest of the main system. The first pass of this encounter was approximately 7.5 disk scale lengths and occurred



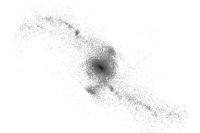
500 Myr ago. This model generally reproduces the northeastern tail and the linear feature to the southwest, though the latter is spatially offset in the model from its position in NGC 1614.

The dynamical model presented here is a qualitatively good match to the system, but does not match it in detail. In particular, it appears that $\mu = 1$ or 2 models are unable to adequately match the system, consistent with previous observational suggestions about the nature of this encounter (e.g., Rothberg & Joseph 2006; Väisänen et al. 2012, ; see below for more discussion). The presented model is likely *not* the encounter parameters for this system, but is presented to demonstrate the practical difficulties in matching systems with only one prominent tail (see Section 5.5.4 for further discussion).

The model shows its deficiencies in the position–velocity plots, where a significant amount of the particles show velocities not seen in the data. In particular, the retrograde system (red points in Figure 5.8) shows a considerable scatter of points within the physical extent of the system, but at somewhat lower velocities than observed. This is despite the plume morphologically matching the arm seen in HST imaging (see Väisänen et al. 2012).

Previous Dynamical Constraints

While this system has no previously published dynamical models, there have been multiple studies attempting to ascertain the nature of the encounter. Based on a comparison of the dynamical support and isophotoal shapes with dissipationless and dissipational mergers, Rothberg & Joseph (2006) suggest this system may be the product of a relatively high mass ratio encounter. An earlier study by Neff et al. (1990) also argues for a relatively high mass ratio encounter (essentially an accretion



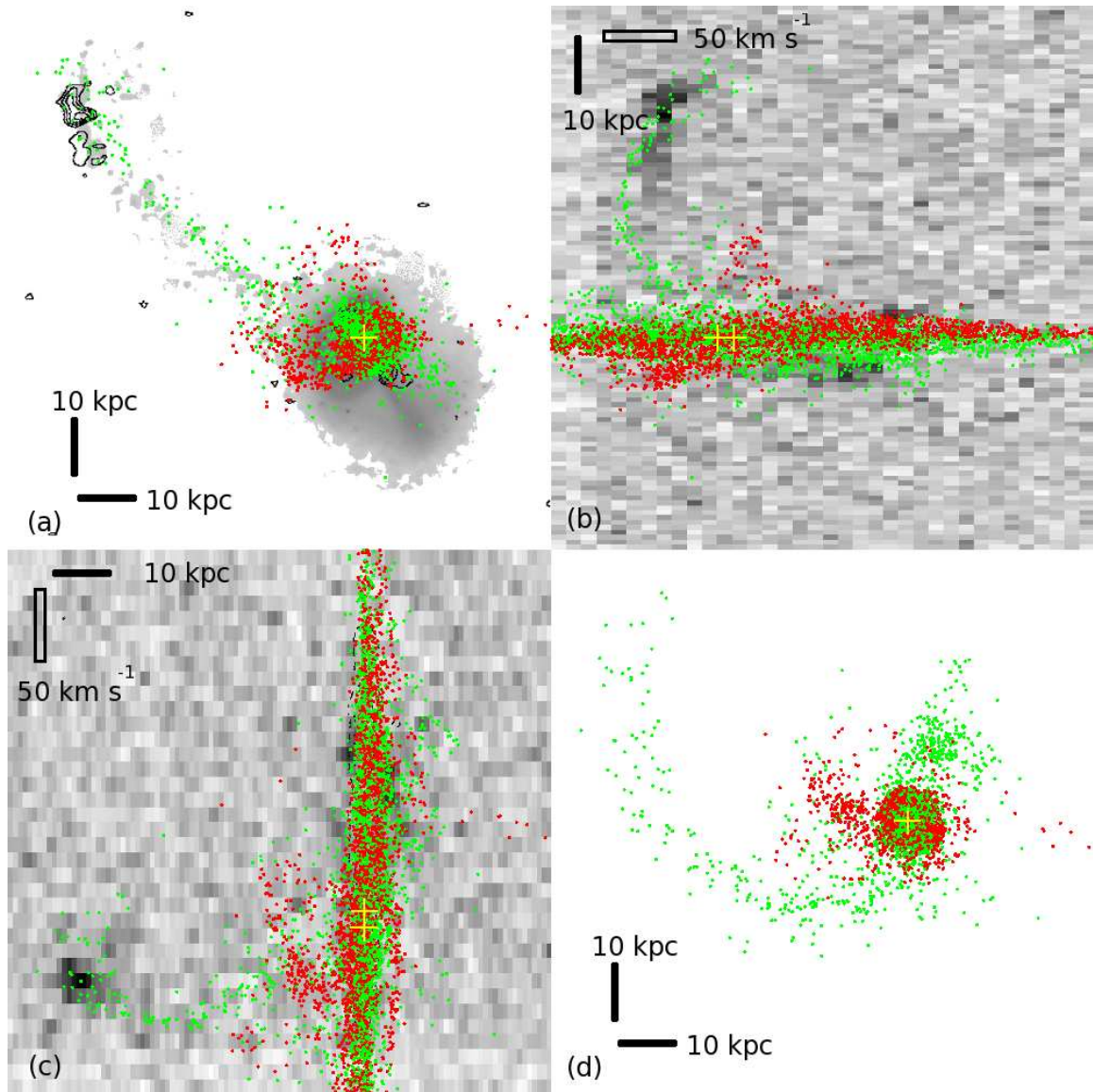
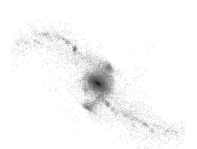


Fig. 5.8.— Identikit visualization of a preliminary test-particle model for NGC 1614, matched to the system. (a): sky view of the system ($\alpha - \delta$), (b) PV diagram ($v - \delta$), (c): PV diagram ($\alpha - v$), and (d) “top-down” view ($\alpha - z$). The sky view covers 102.4 kpc on a side and the velocity range is 376.3 km s^{-1} . In the relevant panels, the solid bar is 10 kpc and the box is 50 km s^{-1} . Panel (a) shows HI contours overlaid on a R-band image from the UH 88”. In panels (b) and (c) the HI data is shown in grayscale, with the darker pixels corresponding to higher peak values along a vector through the data cube. Red and green points show collisionless baryonic particles from N-body realizations representing the two progenitor galaxies. The yellow crosses represent the nuclei of each N-body realization.



event rather than a merger) but their HI observations do not reveal the long NE tail seen in newer observations (Hibbard & Yun 1996).

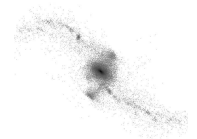
In contrast, Väisänen et al. (2012) argue the interaction is still ongoing and the linear feature to the South of the main body is the interacting companion, viewed essentially edge on (see Väisänen et al. (2012), their Figure 1). However, in the F814W HST image this region appears to be the superposition of the southern tail and the eastern spiral arm wrapping towards the south. Väisänen et al. (2012) also investigate previous claims of the detection of a secondary nucleus (Keto et al. 1992; Alonso-Herrero et al. 2001) but find these secondary point sources to likely be PAH emission in the starbursting ring or a young unextincted cluster.

5.4.6 Non-modeled systems

Not all of the systems in the sample were satisfactorily matched with dynamical models. These systems were not amenable to modeling for different reasons, including technical issues. Below is a discussion of the issues encountered attempting to model NGC 4418 and NGC 6240, and future prospects for modeling these and similar systems.

NGC 4418

This system appears to be the ongoing interaction between an early-type galaxy and a far less massive irregular galaxy (VV 665), showing an obvious HI bridge between the two systems (G. C. Privon *in prep*). An optical tidal tail from VV 665 is also visible. We use the H-band magnitude for each system, and with the assumption of the same M/L ratio, to estimate that the encounter is a $\sim 60:1$ mass ratio encounter (based solely on the stellar mass). Under the additional assumptions that all of the



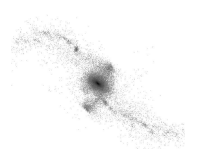
HI originated with VV 655 and that $(M/L)_H \approx 1 M_\odot/L_\odot$ for both systems, the baryonic mass ratio is then estimated as 15:1. Such an extreme mass ratio presents some issues for dynamical modeling. A high mass ratio encounter has a smaller effect on the more massive system, such that the test particle approximation breaks down and accurately representing the dynamical effects on the baryons requires properly treating the self-gravity of the disk.

However, it might be possible to model most of the system, leaving the encounter orientation of NGC 4418 uncertain, by using Identikit to constrain the orbit and encounter geometry (i, ω) of VV 655. This would at least constrain the parameter space, making a search of (i, ω) values for NGC 4418 more achievable. This would necessitate the generation of $\mu = 16$ models for Identikit. In light of the frequency and importance of minor mergers (e.g., Naab et al. 2009; Lotz et al. 2011; Kaviraj 2014) and the number of detailed studies of individual minor merger systems (e.g., Alonso-Herrero et al. 2012; Knierman et al. 2012; Beaton et al. 2013; Duc et al. 2013; Miralles-Caballero et al. 2014), the application of Identikit to these systems might provide interesting tests for scenarios of minor merger activity.

NGC 6240

NGC 6240 has a complicated optical and HI morphology (e.g., Gerssen et al. 2004, Yun & Hibbard *priv comm*), with no obvious correlation between the two (Figure 5.9). The system shows several stellar arms and multiple disconnected regions of HI. Kinematic information on the central region is fairly limited, due to significant HI absorption against the background continuum⁴. To further complicate matters,

⁴In principle, this could be leveraged to constrain models as it is known that the HI absorption must be occurring between us and the nuclear starburst, so we have better z information on the location of the offending HI. However, in practice, the HI absorption is unresolved at the resolution of typical observations—providing no positional information—and the simulation particles generally occupy the entire velocity range of the absorption (see Figure 5.1). “Ground truthing” a hydrody-



HI is detected coincident with an optical galaxy (GALEXASC J165300.71+022112.5; $cz \approx 7125 \text{ km s}^{-1}$, as determined from the HI emission). This system, at a similar redshift to NGC 6240 and at a projected separation of 88 kpc, could potentially have a dynamical influence on the tidal material from the main encounter. If such disturbances are significant, the model of a binary encounter would no longer apply, complicating the matching of a dynamical model to this system.

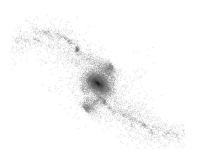
5.5 Discussion

Combining the models from this work and Paper I (Chapter 4) results in a sample of seven systems with reliable dynamical models, plus two more systems with reasonably established merger stages. This constitutes the largest homogeneously derived sample of merger models matched to morphological and kinematic data. The following Subsections discuss the general properties of the mergers by combining the results from these models with the multiwavelength data from GOALS and other sources.

5.5.1 Merger Stage Classification

As the evolution of these systems is driven by their ongoing dynamical encounters, many properties will be considered as a function of the merger stage as derived from these dynamical models. A parameter in the dynamical models is the time since first passage (e.g., Table 5.3). However, the time elapsed between first pass and merger, is different for each system varying by up to a factor of five between systems (see Figure 5.10), making a comparison of systems by the time elapsed since first pass problematic. This requires a different classification of merger stages.

dynamic simulation to a well matched system (e.g., a system from Privon et al. 2013, Chapter 4) and comparing the HI velocities on the near side of the nuclear starburst with the extent of the observed HI absorption may provide guidance on using the absorption as a constraint.



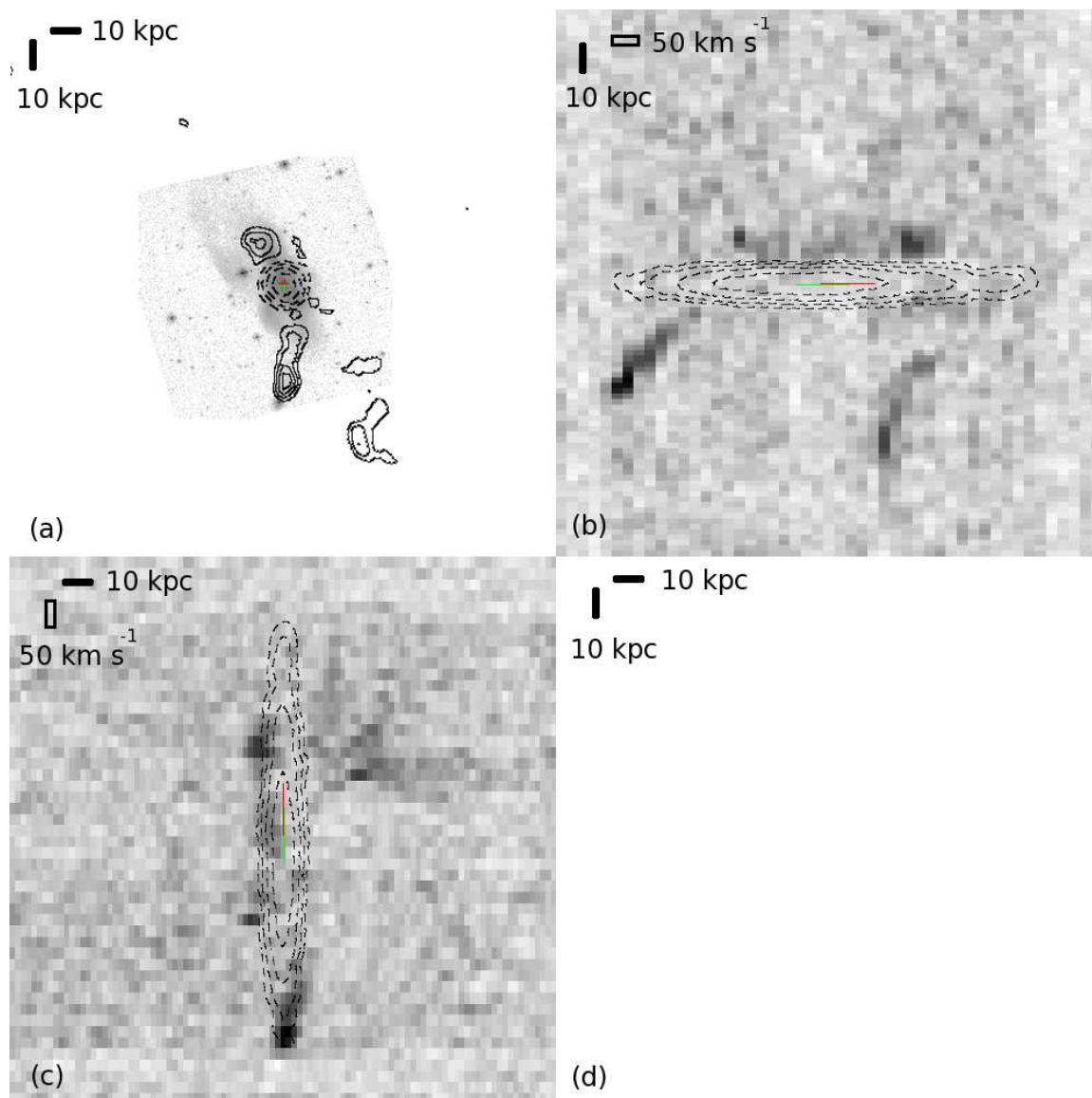


Fig. 5.9.— Visualization of the morphological and kinematic information for NGC 6240. (a): sky view of the system ($\alpha - \delta$), (b) PV diagram ($v - \delta$), (c): PV diagram ($\alpha - v$), and (d) “top-down” view ($\alpha - z$). The sky view covers 76.6 kpc on a side and the velocity range is 839 km s^{-1} . In the relevant panels, the solid bar is 10 kpc and the box is 50 km s^{-1} . In panel (a), the HI is shown as contours over a greyscale HST/ACS F814W image. In panels (b) and (c), the HI data is shown in grayscale, with the darker pixels corresponding to higher peak values along a vector through the data cube. Colored crosses and bars represent the positions of the nuclei and the range of measured recession velocities for the nuclei, respectively.

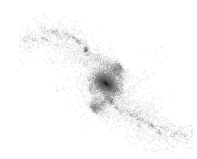


Table 5.2. HI Data Used in Modeling

Source	HI beam (arcsec [, ° PA])	HI vel. res. km s ⁻¹
Mrk 273	16.06 × 14.29, 68.81	22.3
IC 883	16.99 × 15.81, -62.58	10.82
NGC 1614	15. × 10., 83	10.64
NGC 34	16.23 × 13.64, -87.59	42.85
NGC 3256	25.68 × 19.32	16.8
NGC 4418	60. × 52, 6.	12.3
NGC 6240	21.66 × 20.53, 24.76	21.67

Note. — Col 2: Synthesized beam size and position angle; Col 3: Velocity resolution (channel width) of the HI data cube.

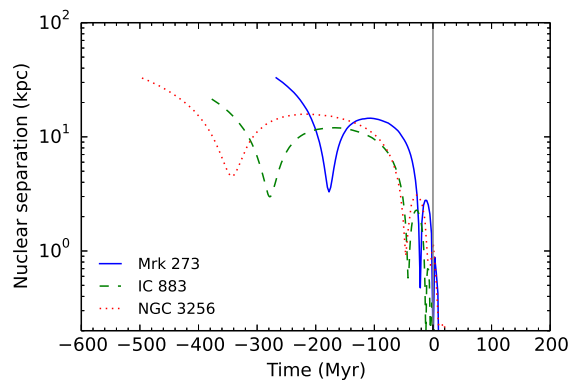


Fig. 5.10.— True nuclear separation as a function of time for Mrk 273 (blue solid line), IC 883 (green dashed line), and NGC 3256 (red dotted line) (see Table 5.3).

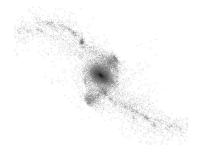
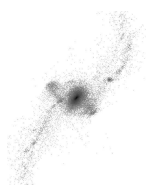


Table 5.3. Dynamical models derived from Identikit matching, Pt. II

System	e	p	μ	(i_1, ω_1) ($^\circ, ^\circ$)	(i_2, ω_2) ($^\circ, ^\circ$)	t	$(\theta_X, \theta_Y, \theta_Z)$ ($^\circ, ^\circ, ^\circ$)	\mathcal{L} (kpc)	\mathcal{V} (km s $^{-1}$)	M_{dyn} ($\times 10^{11} M_\odot$)
Mkn 273	1	0.25	1	(55, 210)	(110, 235)	6.12	(-41, 43, 30)	9.90	224.8	2.9
IC 883	1	0.375	1	(65, 155)	(60, 325)	7.75	(-300, 255, -103)	6.65	134	0.7
NGC 3256	1	0.375	1	(40, 85)	(30, 300)	6.62	(-36.5, -319.9, 65.3)	10.18	132.7	1.0
NGC 1614 ^a	1	0.625	1	(105, 45)	(20, 0)	8.62	(-18.9, 242.3, -40.1)	12.20	159	1.7
NGC 34 ^a	1	0.125	2	(70, 305)	(80, 295)	7.38	(-40.0, -317.9, -45.9)	7.63	216.6	2.1

^aPreliminary model; see text for details.

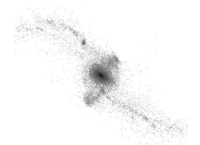
Note. — Model parameters: e – orbital eccentricity, p – pericentric separation (simulation units), μ – mass ratio, (i_1, ω_1) (i_2, ω_2) – disk orientations (see text for description), t – time of best match (simulation units, see text for description), $(\theta_X, \theta_Y, \theta_Z)$ – viewing angle relative to the orbit plane, \mathcal{L} – length scaling factor, \mathcal{V} – velocity scaling factor, M_{dyn} – estimate of the dynamical mass.



To address this, a dynamical merger stage classification scheme has been developed which re-scales the time evolution of each individual system by counting off the number of passes the system has experienced and linearly interpolating between passes to determine the merger stage. In this scheme, a merger stage of 1 is the first passage and 2 is the second passage. A system a quarter of the way between first and second pass would then be a merger stage 1.25 system. For an example of how this maps onto the evolution of the 3D nuclear separation see Figure 5.11. This scheme can be extended to an arbitrary number of successive passes of the nuclei, limited only by the ability to model them (and by the number of passes which can occur before dynamical friction results in the merger of the nuclei).

Post-merger, placing all systems on a common scale is somewhat more challenging due to the lack of well-defined dynamical signposts. With the results of a dynamical model and the corresponding estimation of the time since the nuclei merged (see Tables 4.2 and 5.3), the time in Myr can be rescaled using an appropriate dynamical time. The post-merger stage is denoted using a numeral followed by the letter 'm', with "0m" denoting the time of merger. A system being viewed 2.5 dynamical times after the merger would then be a "2.5m" system. Generically, a merger remnant would be classified as ">0m".

The problem then becomes one of selecting an appropriate dynamical time ($\propto (G\rho)^{-1/2}$) by which to scale the models. One option is the dynamical time within the virial radius; however, this would not serve to set all systems on a common scale, as this dynamical time is (by definition) the same for all systems. A dynamical time at a smaller scale, tied to each individual system is likely a better choice. Two options are to: 1) tie the dynamical time to the models, via the use of some scale length and velocity scaling, or to 2) estimate the dynamical time using observations. It is un-

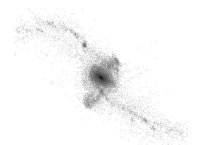


clear, a priori, which is preferable. Tying the post-merger classification to the model makes for a simpler evaluation of the dynamical time as it can be done entirely within the dynamical model. In contrast, tying it to observations potentially strengthens the opportunity to compare with observations, though perhaps with the risk of exacerbating any issues relating to mass-model discrepancies between the simulations and the true mass distribution of the systems. A useful compromise may be the galaxy’s effective radius (R_e), at an observing frequency which isn’t strongly affected by recent star formation. R_e can be measured from observations (e.g., H-band imaging) and used directly in the simulations to compute the dynamical time within that volume, using that dynamical time to scale the post-merger timescale.

We apply this classification to the models presented here and in Paper I, the results of which are included with Table 5.4. Pending tests on the choice of scaling for post-merger systems, these systems are assigned a merger stage of “>0m”.

Comparison with Morphological Merger Stage Classifications

In investigating merger-driven activity in the GOALS sample, previous papers have utilized morphological classifications of the merger stage (e.g., Haan et al. 2011; Lotz et al. 2011; Kim et al. 2013; Stierwalt et al. 2013). These systems diagnose the merger stage by looking at the visual symmetry of the galaxy or galaxies in a system, the separation of the galaxies involved, and the nuclear separation (if there are two distinct nuclei). Stierwalt et al. (2013) describe their classification scheme as: “‘N’ for non-mergers (no sign of merger activity or massive neighbors), ‘a’ for pre-mergers (galaxy pairs prior to a first encounter), ‘b’ for early-stage mergers (post-first-encounter with galaxy disks still symmetric and in tact but with signs of tidal tails), ‘c’ for mid-stage mergers (showing amorphous disks, tidal tails, and other signs



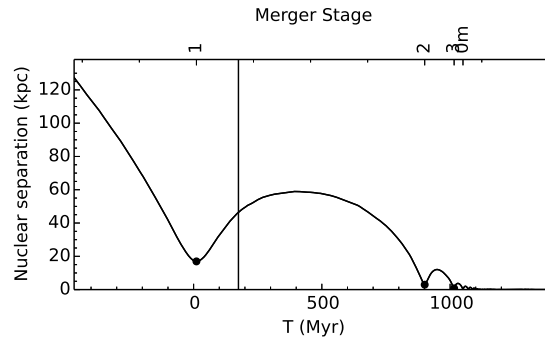
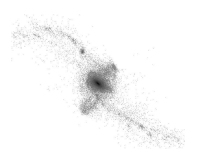


Fig. 5.11.— Example of the mapping from simulation/physical time units (lower abscissa) to our merger stage categorization (upper abscissa) for The Mice. The ordinate shows the true nuclear separation as a function of time. This system would be classified as having a merger stage of ~ 1.25 .

Table 5.4. Merger Stages of Modeled Systems

System	t_{now} (Myr)	Δt_{merge} (Myr)	Stage
Mkn 273	180	40	3
IC 883	280	0	0m
NGC 3256	345	20	2.5
NGC 1614	500	-20	>0m
NGC 34	185	0	>0m
Arp 240	230	1200	1.25
The Mice	175	775	1.25
Antennae	260	70	2
NGC 2623	220	-80	>0m

Note. — Merger stage information for the systems from this work and Paper I: t_{now} – time elapsed since first pericenter passage, Δt_{merge} – time remaining until coalescence based on the assumed dynamical model and input galaxy mass model, Stage – dynamical merger stage determined as described in the text (see Section 5.5.1).

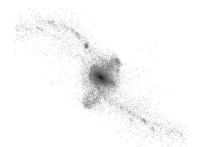


of merger activity), or ‘d’ for late-stage mergers (two nuclei in a common envelope)”. Such classification is as advanced as is possible in the absence of kinematic data and a dynamical model, but is unfortunately subject to projection and opacity effects.

For the seven systems with well-matched dynamical models, we compare our dynamical merger stages with single-waveband morphologically-determined merger stages from other studies (Figure 5.12). Generally, the single-band morphological merger stage and the dynamical merger stage track each other, in the sense that a given system is generally identified as late or early stage in both methods of classification. The dynamical merger stage classification has the advantage of being able to more finely categorize the progress of individual interactions (prior to a merger); of the three systems noted as Spitzer/IRAC merger stage “b”, the dynamical modeling is able to establish that two of these systems are being viewed shortly after first pass while the third is being viewed around the time of second pass.

Similarly, NGC 3256 was identified as a “single-nucleus + tail” system based on HST imaging and a merger stage “d” based on Spitzer/IRAC imaging but the dynamical modeling finds this system to be a merger stage 2.5. This diagnosis is due to the use of multi-band imaging in establishing prior knowledge for the model and so not directly attributable to the modeling itself, but it does demonstrate a potential pitfall for single-band morphological classification.

As morphological classification generally considers the nuclear separation, it is interesting to compare the current true nuclear separation (determined from the models) with the observed projected separation as in Figure 5.13. Here we omit two systems, Mrk 273 and the Antennae. Mrk 273 is a late-stage merger which has not yet finished merging (U et al. 2013); the dynamical evolution of the system center proceeds much more rapidly than for the tails. Given the uncertainties in the age-dating of the

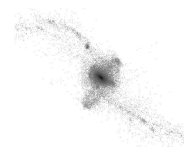


system (estimated in Paper I to be 50 Myr), the model presented here has a slightly smaller nuclear separation than implied by observations, but this is not an issue with the model, which is intended to match the large-scale evolution of the system. The Antennae is omitted as the model presented in Paper I has some deficiencies – among them being the nuclear separation, which is smaller than the observed separation.

For the purposes of assessing the limitations of morphological merger separation—as applied to distinguishing between “common envelope” and widely separated systems—Figure 5.14 shows the cumulative probability distribution of viewing a system with true separation r at a projected separation R , assuming random viewing directions. This demonstrates that a system has a 75% probability of being viewed with $R/r > 0.65$ and a 50% probability of being viewed with $R/r > 0.86$. This demonstrates that, as long as r is greater than approximately twice the diameter of the system, systems have a relatively high probability of being viewed with projected separations that are close to the true value. This suggests that morphological merger classifications of large samples will be fairly robust in differentiating between these two systems. When r begins to approach twice the diameter of the galaxies involved, even identifying two nuclei can become difficult (see NGC 3256). In practice, since most encounters do not involve galaxies with perfectly prograde ($i = 0^\circ$) or retrograde ($i = 180^\circ$) encounters, a nucleus can remain unobscured by the companion galaxy until much closer separations than a few disk scale lengths.

5.5.2 General Properties of the Encounters

The encounter geometry of the systems presented here and in Paper I is relatively homogeneous in the sense that most of the disks are experiencing a prograde encounter. This is primarily a selection effect based on the requirement of extended HI



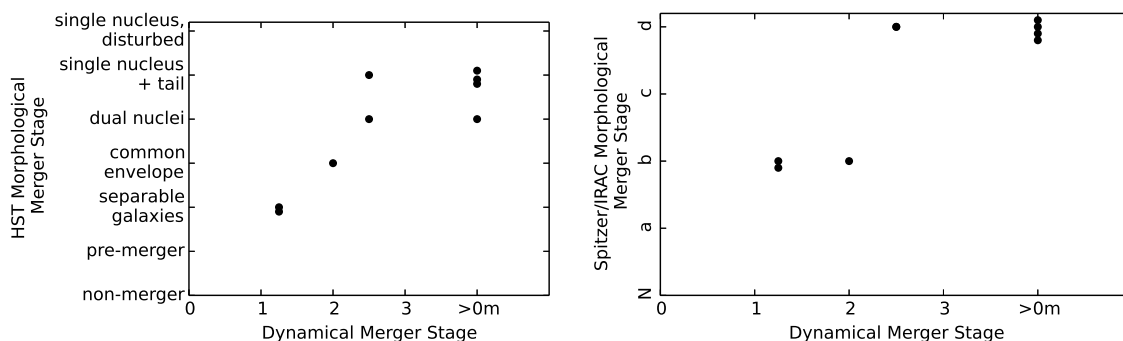


Fig. 5.12.— A comparison of the dynamical merger stages from the modeling with morphological merger stages determined using single-band imaging. Top: A comparison with the merger stages determined by Howell et al. (2010) using HST H-band imaging. Bottom: A comparison with the merger stages determined by Stierwalt et al. (2013) using Spitzer IRAC $3.6 \mu m$ imaging. The two methods generally track each other, however the dynamical modeling provides more precise determinations of the merger stage. Additionally, due to the use of multi-band imaging to determine priors such as the existence and location of dual nuclei, the dynamical merger stage classification correctly classifies systems with dual nuclei where one nucleus is obscured or where the separation is smaller than the resolution of the instrument. To assist visibility, points have slight vertical shifts to avoid overlap.

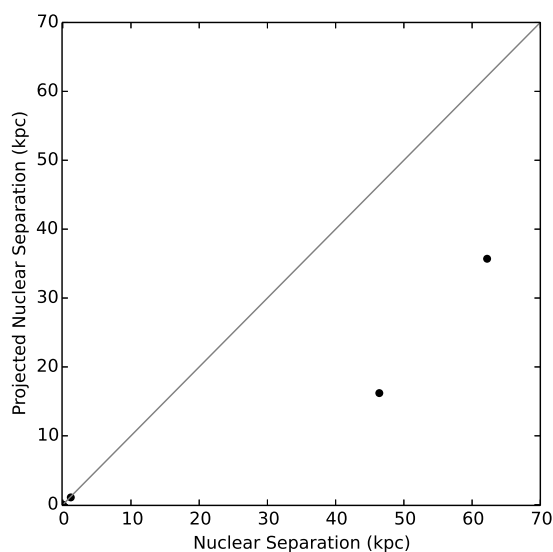
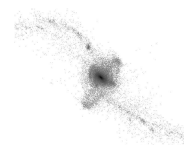


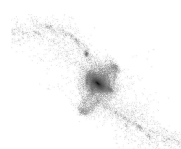
Fig. 5.13.— Comparison of the 3D nuclear separation from the best-fit dynamical model (y-axis) with the observed projected separation (y-axis). The line denotes agreement between the two. Note that two systems (IC 883 and NGC 2623) are both at (0,0).



tidal features in order to constrain the dynamical models. Prograde encounters give rise to spatially and kinematically well-defined tidal tails while retrograde encounters generate more diffuse plumes (e.g., Toomre & Toomre 1972). All else being equal, observations of prograde systems are more likely to result in detectable HI emission in tidal features, providing the critical kinematic information for modelings. Thus, the over-representation of prograde encounters is a selection effect.

While the sample size is still relatively small, there appears to be a dearth of systems with merger stages of $\lesssim 1$ and $1.5 - 1.75$. This likely has its origins in the parent samples—GOALS and the RBGS—and the L_{IR} selection; if the merger-induced star formation lags first pass and returns to the levels of a quiescent galaxy before subsequent passes, systems at these merger stages would not be IR bright and this would not be selected by the parent GOALS sample. This could be ameliorated by matching dynamical models to a morphologically selected sample. The KPAIRS sample may provide such a starting point (Xu et al. 2010).

The distribution of mass ratios for encounters which lead to U/LIRG activity is an interesting question (e.g., Mihos et al. 1992; Mihos & Hernquist 1994a) – at what point is the mass ratio too high to trigger such a high starburst? Unfortunately we are unable to address this with the present sample; the models presented here and in Paper I are all $\mu = 1$ or 2 ; Identikit does not presently have the capability of modeling higher mass ratio encounters. The modeling bias in μ is also due to the relative ease of matching systems—the more massive system in high μ encounters responds more subtly to the encounter making the inclusion of self-gravity more important, negating the applicability of test particles (to the matching of the more massive system).

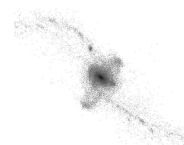


5.5.3 Activity as a Function of Merger Stage

Star Formation

A well-known prediction of merger-driven activity is enhanced star formation (Toomre & Toomre 1972), particularly during close passes and final coalescence (e.g., Barnes & Hernquist 1991; Mihos & Hernquist 1994b). Early studies of U/LIRGs noted that their optical morphology was consistent with mergers and interactions (Armus et al. 1987)—providing evidence for merger-induced star formation, assuming L_{IR} is due in large part to star formation. Studies of the star formation rates in close pairs of galaxies as a function of separation (e.g., Bushouse 1986; Ellison et al. 2010) and as a function of morphological merger stage (e.g., Stierwalt et al. 2013) have shown evidence for enhanced star formation for close pairs and late-stage interactions, respectively. These studies are broadly consistent with theoretical predictions regarding the influence of mergers on galactic star formation.

With the merger stages provided by dynamical models we can—for the first time—construct an observationally constrained picture of the evolution of star formation rates as a function of time. Figure 5.15 is a plot of the specific star formation (values from Howell et al. 2010) as a function of the dynamical merger stage obtained as part of the modeling presented here. The shaded region denotes the “main sequence” of star formation from Elbaz et al. (2011). Though based on a small number of objects, this is consistent with previous work suggesting mergers should enhance star formation rates above those in quiescent galaxies (e.g., Toomre & Toomre 1972; Barnes & Hernquist 1991; Mihos & Hernquist 1994b).



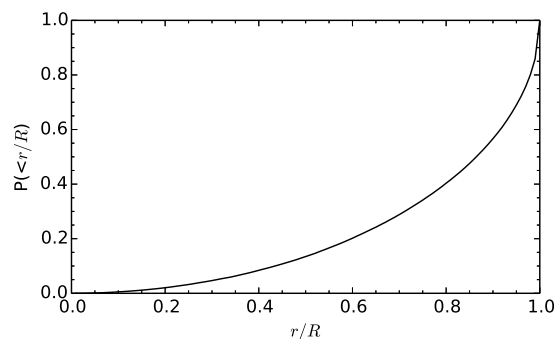


Fig. 5.14.— Cumulative probability distribution of viewing a galaxy pair with a true separation of r at a projected separation of R , assuming random viewing directions. A system has a 75% probability of being viewed with its projected separation being $> 65\%$ of the true value and a 50% probability of its projected separation being $> 86\%$ of the true value.

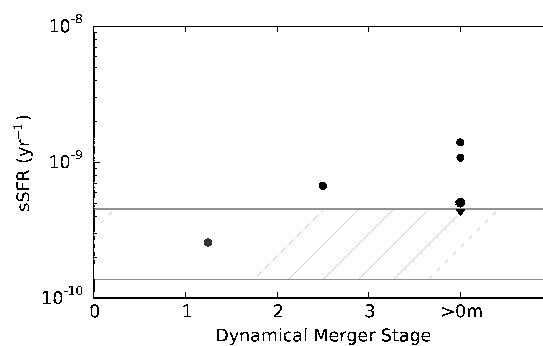
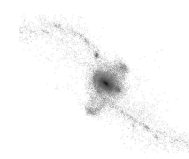


Fig. 5.15.— Specific star formation rate (sSFR) as a function of dynamical merger stage. The sSFR is taken from Howell et al. (2010) and the area between the grey lines marks the “main sequence” of star formation from Elbaz et al. (2011). One source is shown as an upper limit due to AGN contamination of the infrared luminosity.

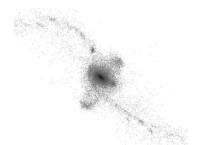


AGN Activity

Active galactic nuclei have long been linked with galaxy mergers (e.g., Sanders et al. 1988) though the causal relationship is somewhat disputed (e.g., Cisternas et al. 2010) and is likely dependent on the luminosity of the AGN (Treister et al. 2012). Mid-infrared observations of the systems in our sample were used by Stierwalt et al. (2013) to estimate what fraction of the infrared luminosity is due to the starburst and what fraction is due to the AGN. Specifically, the $6.2 \mu\text{m}$ PAH equivalent widths are considered from Stierwalt et al. (2013); lower values indicate the mid-infrared is dominated by an AGN while high EQW values are consistent with a starburst origin for the mid-infrared emission. Figure 5.16 shows the equivalent width of the $6.2 \mu\text{m}$ PAH feature as a function of the dynamical merger stage, with the average EQW for starbursts from Brandl et al. (2006) marked. Though the smaller number of systems in this sample with energetically important AGN makes precludes commenting directly on the triggering of AGN by interactions, Figure 5.16 is consistent with a scenario in which the AGN contributes strongly to the infrared luminosity. The systems with lower EQW tend to be later stage systems, consistent with a scenario in which the rapid dynamical evolution leading up to and during coalescence may result in AGN activity (Toomre & Toomre 1972; Hernquist 1989).

5.5.4 Comments on the Matching Process

In Paper I the assertion was made that the matching of dynamical models was greatly simplified using Identikit, at least for mergers where both disks were prograde. The systems modeled here expand the sample to include an encounter in which one disk has a retrograde spin. As expected, the retrograde disks are somewhat more difficult to match, owing to the less prominent tidal response. This affects both the



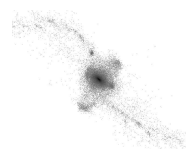
observations—tidal features are more diffuse and therefore more difficult to obtain kinematic information—and the hybrid simulations—the tidal features aren't as well defined and have poorer sampling of test particles. Fortunately this does not preclude the matching of dynamical models to these systems, however in practice, obtaining a confident dynamical match requires more iteration between hybrid and self-consistent simulations.

Retrograde encounters and $\mu > 1$ encounters can sometimes produce qualitatively similar morphologies in the hybrid Identikit simulations. In the $\mu > 1$ encounter, the more massive galaxy will exhibit a suppressed tidal response so that the weak tidal tail may not be lifted significantly from the disk and it may resemble the less well defined plumes of a retrograde encounter. Fortunately this degeneracy is quickly broken by running self-consistent simulations. This creates an increase in the number of iterative steps to reach an accurate model, but seems to successfully discriminate between these two scenarios.

5.6 Summary

Robust dynamical models are presented for three interacting systems and potential models for two more; none of these galaxies have previously published models. These new models, combined with the models presented in Paper I, cover a range of merger stage and interaction geometries. A dynamically motivated merger stage classification scheme is introduced and described which facilitates the comparison of systems with different characteristic timescales during their interactions. Possibilities are discussed for extending this scheme to post-merger systems.

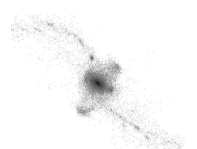
Through the use of this new merger stage classification observations of AGN and star formation activity are placed in the the context of the ongoing mergers. The



results are consistent with previous numerical predictions and observational results that star formation is enhanced above the “main sequence” during late stages of encounters. AGN activity is found to be associated with later-stage encounters, which is consistent with previous results.

Acknowledgements

G.C.P. was supported by NSF grants AST 1109475 and 02-06262, and by a Visiting Graduate Research Fellowship at the Infrared Processing and Analysis Center / Caltech. This work was supported in part by National Science Foundation Grant No. PHYS-1066293 and the hospitality of the Aspen Center for Physics. G.C.P thanks A. Medling and V. U for helpful discussions on NGC 6240 as well as for providing data in advance of publication.



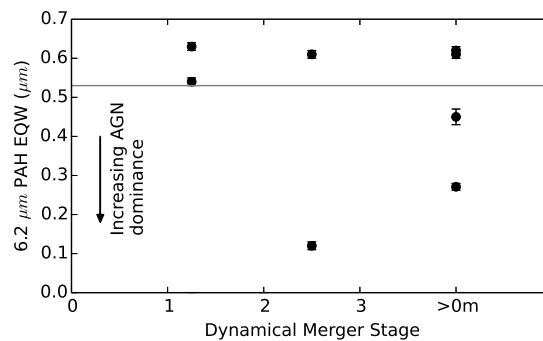
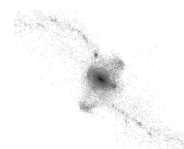


Fig. 5.16.— $6.2 \mu\text{m}$ EQW as a function of the dynamical merger stage. The EQW measurements are taken from Stierwalt et al. (2013); high values denote systems dominated by star formation. The two galaxies in Arp 240 are plotted separately as they have individual PAH measurements. The horizontal line marks the average $6.2 \mu\text{m}$ PAH EQW for starbursts from (Brandl et al. 2006).



Chapter 6

The Utility of HCN (1–0) and HCO⁺ (1–0) as tracers of high-density gas in Local Luminous Infrared Galaxies¹

6.1 Introduction

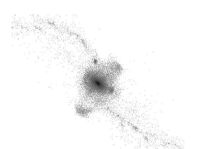
Molecular gas is observationally linked to ongoing star formation (e.g., Bigiel et al. 2008; Leroy et al. 2012). The rotational transitions of HCN (1–0) and HCO⁺ (1–0) have relatively high critical densities ($n_{crit} \approx 3 \times 10^6 \text{ cm}^{-3}$ and $2 \times 10^5 \text{ cm}^{-3}$, respectively, at 30 K) and so trace higher density molecular hydrogen gas in star-forming regions than CO (1–0) ($n_{crit} \approx 2 \times 10^3 \text{ cm}^{-3}$), which traces the bulk of

¹To be submitted to the Astrophysical Journal Letters as “The Utility of HCN (1–0) and HCO⁺ (1–0) as tracers of high-density gas in Local Luminous Infrared Galaxies”, with authors: G. Privon, R. Herrero-Illana, A. Evans, K. Iwasawa, M. Perez-Torres, S. Stierwalt, L. Armus, E. Murphy, and J. Mazzarella.

the molecular gas, even that which is not directly associated with star formation. The correlation between HCN (1–0) and the infrared luminosity, $L_{\text{IR}}[8 - 1000 \mu\text{m}]$, of galaxies is observed to be tighter than the CO (1–0) to L_{IR} correlation (Gao & Solomon 2004); this is most likely due to the fact that massive star formation (which heats the dust and gives rise to L_{IR}) occurs in the dense regions of molecular clouds.

Recent studies have found global (Graciá-Carpio et al. 2006) and spatially-varying enhancements (Kohno et al. 2003; Imanishi et al. 2006, 2007, 2009; Davies et al. 2012) in the ratio of HCN (1–0)-to-CO (1–0) emission (compared to HCO^+ (1–0)-to-CO (1–0) ratio) for systems hosting active galactic nuclei (AGN). Similar results have been found for higher-J transitions, HCN (4–3) and HCO^+ (4–3) (Imanishi & Nakanishi 2013, 2014). These results, if correct, suggest that in the presence of AGN, HCN emission is enhanced relative to the HCO^+ and CO emission, and would invalidate the use of HCN as a tracer of the dense molecular gas involved in star formation. However it is notable that some systems with a known AGN do not show this enhanced ratio (Arp 299, Imanishi & Nakanishi 2006; I Zw 1, Evans et al. 2006). Modeling by various authors suggests the HCN and HCO^+ emission are affected by density, radiative, and abundance/ionization effects which potentially complicates interpretation of the line ratios in both photon dominated and X-ray dominated regions (PDR and XDR, respectively; e.g., Aalto et al. 1995; Lepp & Dalgarno 1996; Meijerink et al. 2007). These scenarios will be further investigated in the discussion.

IRAM 30m EMIR observations of the HCN (1–0) and HCO^+ (1–0) lines for a sample of luminous and ultraluminous infrared galaxies (U/LIRGs; $L_{\text{IR}}[8 - 1000 \mu\text{m}] \geq 10^{11} L_{\odot}$; Section 6.2) are used in combination with calibrated AGN strengths from mid-infrared spectroscopy to assess the effects of an AGN on the global HCN (1–0) and HCO^+ (1–0) emission (Section 6.3), and their utility as a tracer of dense gas



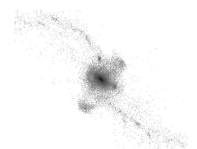
associated with star formation (Section 6.4). The power of this study comes from the increased sample size of U/LIRGs with measurements of these lines (a $\sim 200\%$ increase) and from the inclusion of mid-infrared diagnostics of the relative importance of AGN and star formation to the infrared luminosity of each system. This enables a direct investigation of the integrated line ratio as a function of the contribution of the AGN to the bolometric luminosity, L_{bol} .

6.2 Data

The data used here are taken from a survey of U/LIRGs selected from the Great Observatories All-Sky LIRG Survey (GOALS; Armus et al. 2009). The GOALS sample as a whole consists of all the U/LIRGs from the Revised Bright Galaxy Sample (i.e., $60 \mu\text{m}$ flux density greater than 5.24 Jy ; Sanders et al. 2003). The IRAM 30m Telescope ² was used with the EMIR receiver to observe an 8 GHz instantaneous bandwidth, tuned to capture HCN (1–0), HCO⁺ (1–0), CCH, and HNC (1–0) simultaneously, thus reducing systematic uncertainties when comparing the fluxes of these lines. The beam size for these measurements is $\sim 28''$. Full results of the survey will be presented in future work (G. C. Privon *in prep*), along with CO (1–0) observations of the same sample (R. Herrero-Illana *in prep*). For the analysis we also include HCN (1–0) and HCO⁺ (1–0) measurements of LIRGs in GOALS from studies by Graciá-Carpio et al. (2006) and Costagliola et al. (2011).

Diagnostics of AGN activity were obtained from mid-infrared observations with Spitzer; the $6.2 \mu\text{m}$ PAH equivalent width is taken from IRS low-resolution observations (Stierwalt et al. 2013), while observations of high and low ionization lines ([Ne

²Based on observations carried out with the IRAM 30m Telescope. IRAM is supported by INSU/CNRS (France), MPG (Germany) and IGN (Spain).

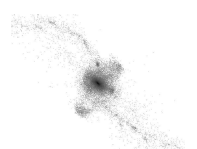


v], [O IV], and [Ne II]) were taken from IRS high-resolution observations (Petric et al. 2011; Inami et al. 2013). These mid-infrared fluxes were measured from smaller apertures, compared to the millimeter lines. However these measurements are intended to assess the relative dominance of the AGN to the mid-infrared emission, and the AGN emission is expected to be compact, suggesting any aperture effects would serve to overemphasize the importance of the AGN. Assuming the star formation is more extended than the AGN’s radiative sphere of influence, a large aperture would include more star formation driven flux in any of the diagnostics, relative to a constant flux from the AGN. Thus, a smaller aperture would likely overestimate the importance of the AGN. As will be shown, the excitation of these molecular transitions does not appear to be solely a function of the AGN strength, thus we conclude our results are not being significantly biased by the mis-match in aperture between the millimeter and mid-infrared datasets.

6.3 HCN (1–0) as a Tracer of AGN Activity

Figure 6.1 shows the $L'_{\text{HCN (1-0)}}/L'_{\text{HCO}^+ (1-0)}$ ratio versus L_{IR} . The behavior with L_{IR} shows the same general trend at high luminosities as seen in Graciá-Carpio et al. (2006), but shows increased scatter at lower IR luminosities. It does appear that there is a dearth of ULIRGs with low values of $L'_{\text{HCN (1-0)}}/L'_{\text{HCO}^+ (1-0)}$, however the increased sample size also shows a number of LIRGs with lower L_{IR} values having $L'_{\text{HCN (1-0)}}/L'_{\text{HCO}^+ (1-0)}$ values as high as the ULIRGs.

In Figure 6.2, we plot $L'_{\text{HCN (1-0)}}/L'_{\text{HCO}^+ (1-0)}$ against several mid-infrared diagnostics of the relative dominance of AGN and star formation. Previous works (e.g. Graciá-Carpio et al. 2006) independently studied the $L'_{\text{HCN (1-0)}}/L'_{\text{CO (1-0)}}$ and $L'_{\text{HCO}^+ (1-0)}/L'_{\text{CO (1-0)}}$ ratios; here we do not compare with CO (1–0) as CO (1–0) traces less dense molecular



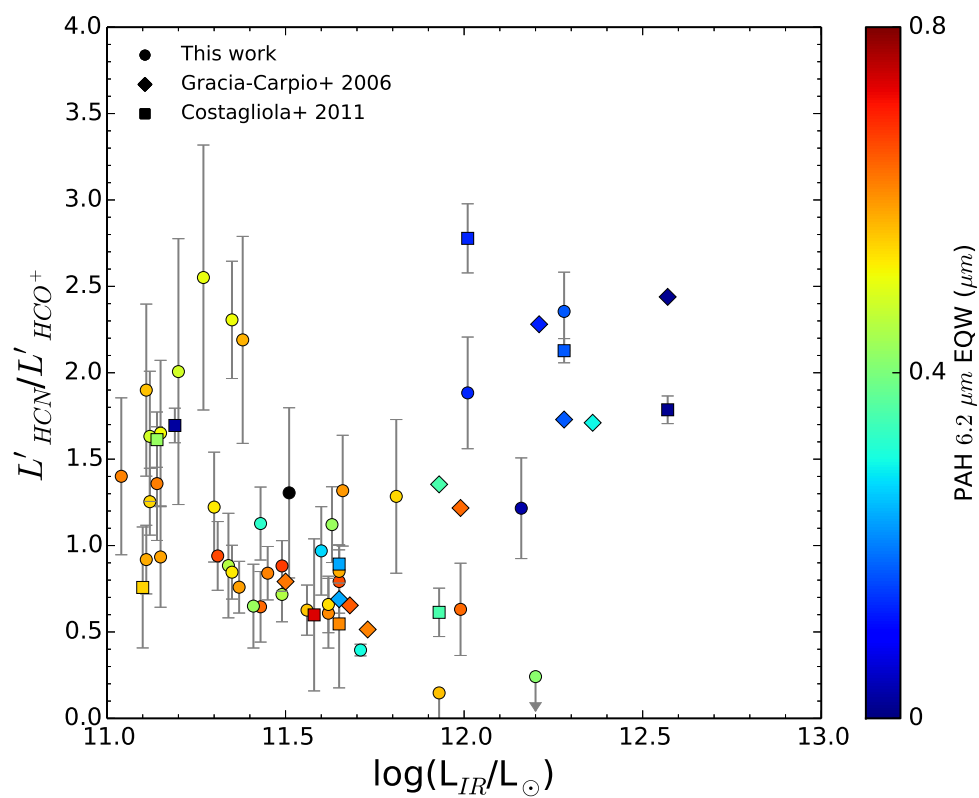
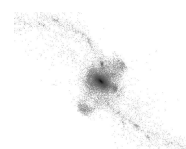


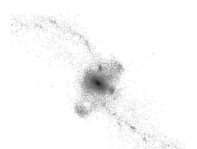
Fig. 6.1.— Ratio of the $L'_{\text{HCO}^+ (1-0)}$ -to- $L'_{\text{HCO}^+ (1-0)}$ luminosities versus the total infrared luminosity. The infrared luminosities are from Armus et al. (2009).



gas, potentially including molecular gas which is not physically associated with the regions emitting in HCN (1–0) and HCO⁺ (1–0). The diagnostics plotted trace the relative contribution of AGN and star formation to the infrared luminosity, where lower (higher) values of the PAH EQW ([Ne v]/[Ne II] or [O IV]/[Ne II] ratio) denote more dominant AGN. In all cases, we find no unique trend in the $L'_{\text{HCN (1-0)}}/L'_{\text{HCO}^+ (1-0)}$ ratio as a function of AGN strength.

For systems with > 50% AGN contribution to the mid-infrared luminosity (PAH EQW $\lesssim 2.5 \times 10^{-1} \mu\text{m}$; [Ne v]/[Ne II] $\gtrsim 7 \times 10^{-1}$ Petric et al. 2011), the $L'_{\text{HCN (1-0)}}$ -to- $L'_{\text{HCO}^+ (1-0)}$ ratio is in the range 1–2.5, with lower values absent. In contrast, for systems which appear to be star formation dominated, this ratio exhibits no clear trend and a very large scatter—they have ratios within the range of AGN dominated systems (1–2.5) as well as smaller ratios. Previous work by Costagliola et al. (2011) on a smaller sample noted this effect, though using only the PAH EQW diagnostic.

The origin of high $L'_{\text{HCN (1-0)}}$ -to- $L'_{\text{HCO}^+ (1-0)}$ ratio for starbursts systems has been explained by the presence of dense, high column molecular gas (Meijerink et al. 2007). In this case, the large range in this ratio for star formation dominated systems (PAH EQW $\gtrsim 2.5 \times 10^{-1} \mu\text{m}$; [Ne v]/[Ne II] $\lesssim 7 \times 10^{-1}$), suggests these systems have a range of molecular gas densities, with some featuring dense nuclear starbursts and others exhibiting a more “disky” mode of star formation (e.g., Bryant & Scoville 1999). Based on the lack of a unique trend with the relative contribution of AGN and star formation to L_{IR} , it appears the global HCN (1–0)-to-HCO⁺ (1–0) ratio has a complex dependence on the physical conditions in the gas as well as the radiation field.



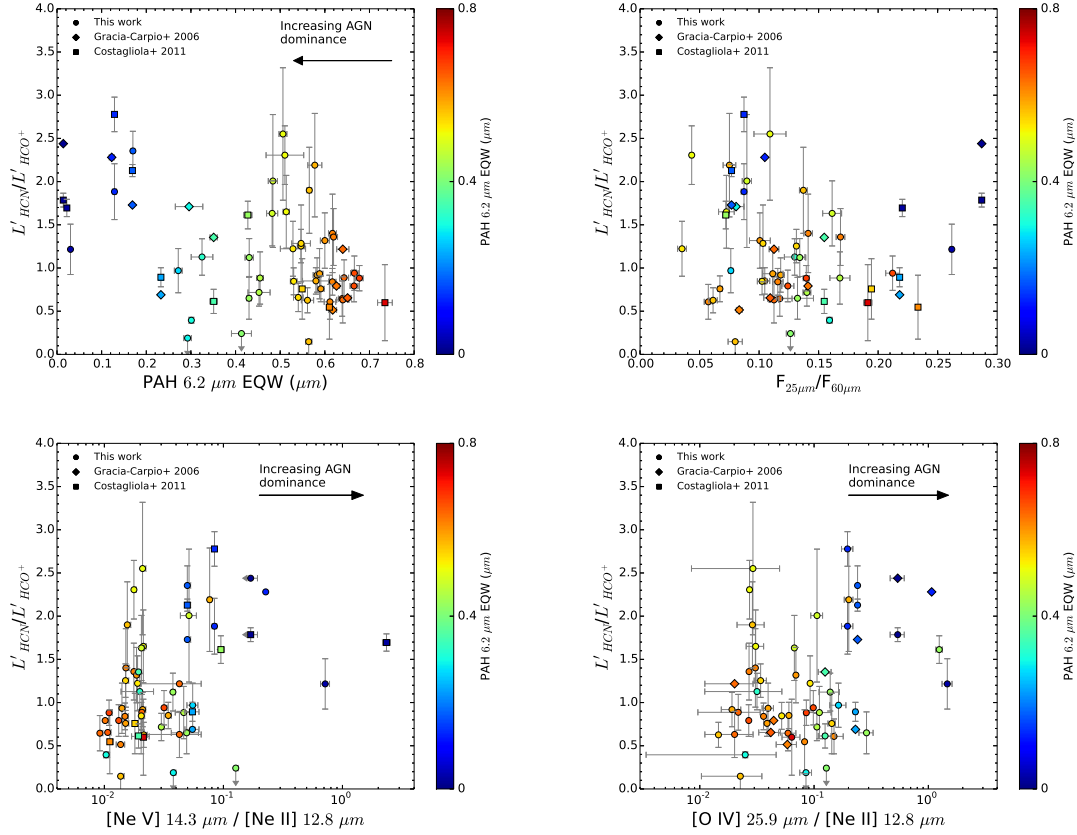
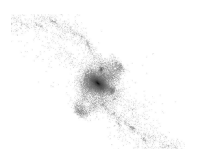


Fig. 6.2.— $L'_{\text{HCN}}/L'_{\text{HCO}^+}$ to L'_{HCO^+} as a function of various mid-infrared tracers of AGN dominance. In all panels, the points are colored by their PAH EQW as measured by Stierwalt et al. (2013). The symbol shape notes the origin of the millimeter line measurements; circles are new data, triangles are from Graciá-Carpio et al. (2006) and squares are from Costagliola et al. (2011). Clockwise from upper left: the ratio versus $6.2 \mu\text{m}$ PAH EQW from Stierwalt et al. (2013), the ratio versus IRAS $F_{25 \mu\text{m}}/F_{60 \mu\text{m}}$ from Sanders et al. (2003), the ratio versus $[\text{O IV}]/[\text{Ne II}]$ from Inami et al. (2013), and the ratio versus $[\text{Ne v}]/[\text{Ne II}]$ from Inami et al. (2013).



6.3.1 Potential Distance Effects

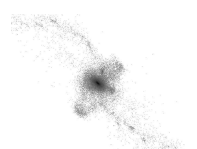
The sample spans a factor of ~ 6 in distance, leading to possible concerns about the effects of beam size on the results. Considering a hypothetical system with a centralized, ~ 100 pc scale enhancement in the $L'_{\text{HCN}(1-0)}$ -to- $L'_{\text{HCO}^+(1-0)}$ ratio (see Davies et al. 2012) but otherwise “normal” $L'_{\text{HCN}(1-0)}$ -to- $L'_{\text{HCO}^+(1-0)}$ ratio – the same galaxy, viewed at different distances would have different ratios, depending on how much of the galaxy was included in the single-pointing. Given the more IR luminous sources tend to be found at larger distances, distance could potentially bias our results. To check this, the $L'_{\text{HCN}(1-0)}$ -to- $L'_{\text{HCO}^+(1-0)}$ ratio is shown as a function of distance (Figure 6.3); there is no obvious trend of the ratio with distance, either for the entire sample or for AGN-dominated systems, suggesting these results are not being driven by distance effects.

6.4 A SFR – $L'_{\text{HCN}(1-0)}$ Relation for U/LIRGs

Given no evidence for unique signature of the AGN on the HCN (1–0)-to-HCO⁺ (1–0) line ratio, it is worth investigating the relationship between the HCN (1–0) and the star formation rates in these systems. Figure 6.4 shows $L'_{\text{HCN}(1-0)}$ versus L_{IR} for the systems in our analysis, in addition to data from Gao & Solomon (2004). As in previous studies, a strong correlation is seen between these two quantities. In contrast to Gao & Solomon (2004) a fit to the data shows a sub-linear relationship between L_{IR} and $L'_{\text{HCN}(1-0)}$ (when L_{IR} is considered the independent quantity):

$$\log_{10}(L'_{\text{HCN}}) = 0.78 \log_{10}(L_{\text{IR}}/L_{\odot}) - 0.59 \quad (6.1)$$

Cast with $L'_{\text{HCN}(1-0)}$ as the independent quantity, the star formation (as traced by L_{IR})



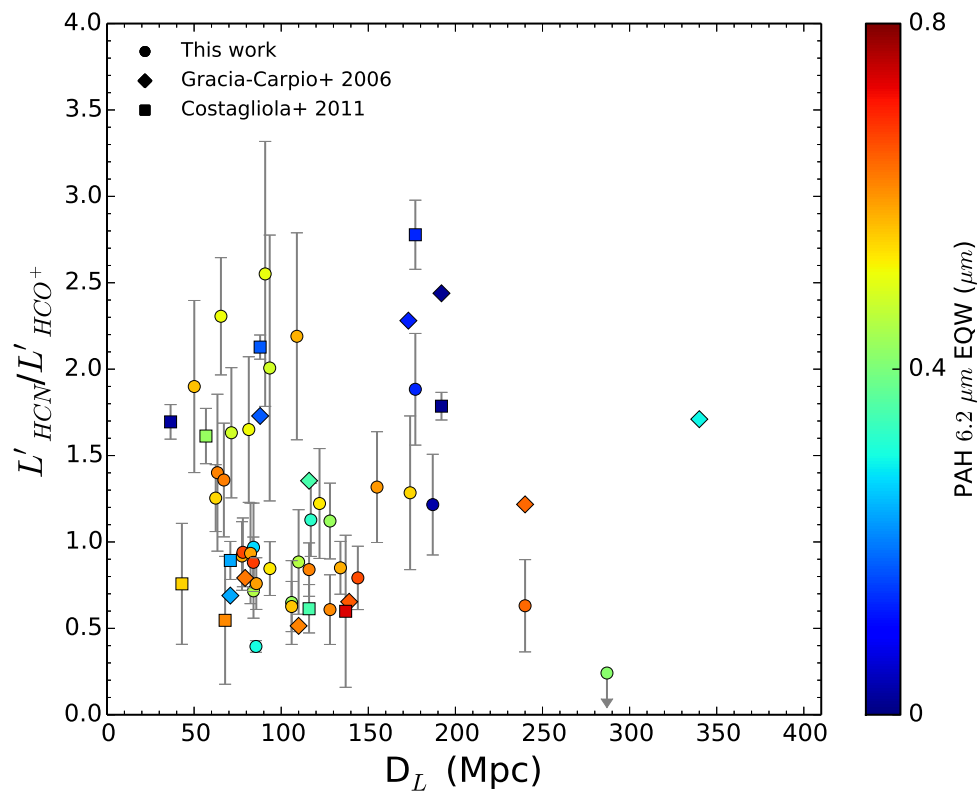
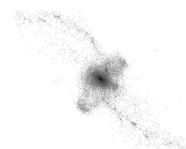


Fig. 6.3.— Ratio of the $L'_{\text{HCN}}(1-0)$ and $L'_{\text{HCO}^+}(1-0)$ luminosities versus luminosity distance. The lack of a significant correlation suggests our results are not being affected by the distances to each system.



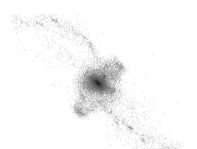
is super-linearly related to the emission from this putative dense gas tracer. This, in conjunction with the lack of a single mechanism leading to HCN (1–0) enhancement (Section 6.3), suggests the relationship between HCN (1–0) and L_{IR} is determined by the star formation rate, radiation field, and the local gas density.

In star formation dominated systems, $L'_{\text{HCN (1-0)}}/L'_{\text{HCO}^+ \text{(1-0)}}$ spans a factor of ~ 5 for a given PAH EQW value. If this ratio can be high in dense, high column gas (e.g., Meijerink et al. 2007), this spread may simply reflect a range in star formation rate surface densities in U/LIRGs. At lower values of L_{IR} , the LIRG population shifts towards a more normal, “disky” mode of star formation. While mid-infrared observations of these systems are typically not able to resolve the starburst (e.g., J. Mazarella et al. *in prep*), interferometric radio and dust continuum observations with ALMA and the VLA can be used to measure the sizes. These size measurements may assist in interpreting the range of $L'_{\text{HCN (1-0)}}/L'_{\text{HCO}^+ \text{(1-0)}}$ seen in systems dominated by star formation.

6.4.1 Future Observations

This study shows starburst-dominated systems can show $L'_{\text{HCN (1-0)}}/L'_{\text{HCO}^+ \text{(1-0)}}$ ratios in excess of one, however there are comparatively fewer AGN-dominated systems in the present sample. More single-dish observations of AGN-dominated ULIRGs would be useful to study the dense-gas tracers in that population.

While a spatially resolved comparison has been undertaken for systems known to host an AGN (e.g., Kohno et al. 2003; Imanishi et al. 2006, 2007, 2009; Davies et al. 2012), it would be instructive to perform the same exercise on systems with little to no evidence for an AGN but which still have a high $L'_{\text{HCN (1-0)}}/L'_{\text{HCO}^+ \text{(1-0)}}$ ratio. Combining such observations with a high-resolution tracer of the ongoing star formation (e.g.,



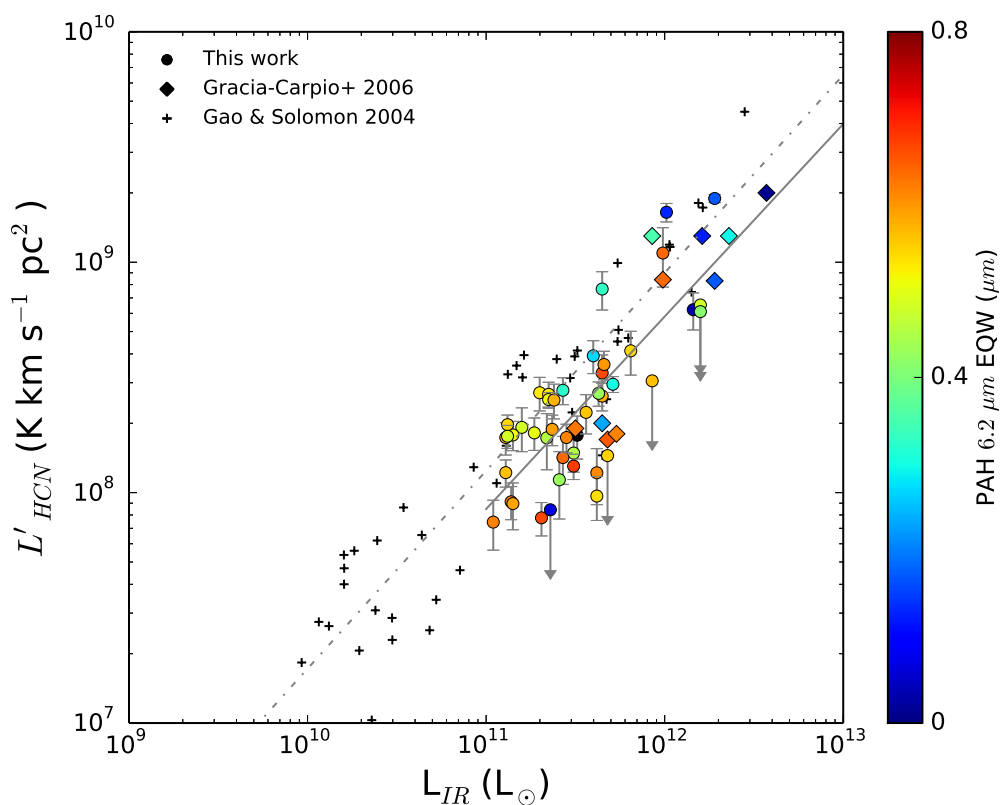
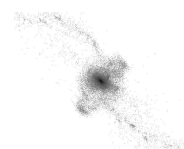


Fig. 6.4.— $L'_{\text{HCN}(1-0)}$ versus L_{IR} , showing HCN linearly increases with L_{IR} for a range of L_{IR} values. As our sample features relatively few AGN dominated system (see Figure 6.2), we find a result similar to previous studies— $L'_{\text{HCN}(1-0)}$ traces the ongoing star formation in these systems. The grey dashed line marks the best fit relation (Eq 6.1). The Gao & Solomon (2004) points have been corrected to the cosmology assumed here.



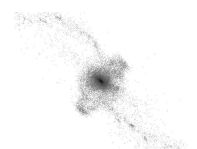
radio continuum) and mapping the dense gas locations implied by the star formation may provide a stronger test of the scenario where a high $L'_{\text{HCN}(1-0)}/L'_{\text{HCO}^+(1-0)}$ ratio correlates with high column, high density gas. Certainly this should be easily testable with Atacama Large Millimeter/sub-millimeter Array and the Karl G. Jansky Very Large Array.

6.5 Conclusions

Using measurements of the putative high density gas tracers HCN (1–0) and HCO⁺ (1–0) in a sample of local U/LIRGs, a comparison with mid-infrared AGN indicators suggests any enhancement in the global HCN (1–0) emission (relative to HCO⁺ (1–0)) does not uniquely trace the presence of an AGN. While we find the AGN can enhance the HCN (1–0) emission relative to HCO⁺ (1–0), the same magnitude of enhancement is also present for many systems which are dominated by star formation. These results are consistent with modeling predictions (Meijerink et al. 2007) and an earlier study (Costagliola et al. 2011) that the global HCN (1–0) emission can also be enhanced by the presence of dense gas. The HCN (1–0) and HCO⁺ (1–0) emission is determined by the interplay of radiation field, gas column, and gas density, making a simple interpretation of the line ratio difficult.

Acknowledgements

G.C.P. was supported by NSF grants AST 1109475 and 02-06262, and by a Visiting Graduate Research Fellowship at the Infrared Processing and Analysis Center / Caltech. This work was supported in part by National Science Foundation Grant No. PHYS-1066293 and the hospitality of the Aspen Center for Physics.



Chapter 7

Summary

This dissertation focused on the neutral and dense portions of the ISM in starbursting galaxies as well as the dynamics and interaction in galaxy mergers.

7.1 Galaxy Interactions

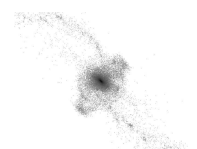
A survey of HI in non-merger and pre-merger LIRG systems has suggested the enhanced star formation in these systems is due to ongoing interactions. In the case of non-mergers, their HI morphology was consistent with minor merger events. The morphologically classified “pre-merger” systems were found to show evidence for tidal interaction in their HI. This suggests these systems are being viewed shortly after first pass, when the extended HI has had time to respond, while the stars, deeper in the potential well, have not yet had time to form tails. Follow-up dynamical modeling will provide a test of this hypothesis.

Chapter 4 demonstrated the first application of Identikit to modeling ongoing mergers, showing the effectiveness of Identikit in rapidly and accurately matching the morphology and kinematics of observed mergers. Together, Chapters 4 and 5 consti-

tute the largest sample of systems with dynamical models matched in a consistent manner. Along with the presentation of new models, a dynamical merger stage classification is proposed for systems between first passage and coalescence of the nuclei. This scheme was used to place observations of star formation and AGN diagnostics in the context of the ongoing galaxy mergers and an extension was discussed for an analogous classification of post-merger systems.

Dynamical modeling, coupled with the dynamical classification scheme, offers more precise determinations of merger stage, particularly for systems at the earlier stages of their interactions (where a system experiences a wide range of tidal field strengths over a long range in time). It is possible that such a classification will more precisely elucidate the change in star formation rate as a function of time during an interaction (based on observations, rather than numerical models), modulo the decreased sample size compared with morphological classification. The case for improving the understanding triggering of AGN using this classification scheme is less tenable, as SMBH accretion is likely more dependent on the pc-scale physics and may not be directly linked to the large-scale tidal field experienced by a galaxy, but see Hopkins et al. (2011a).

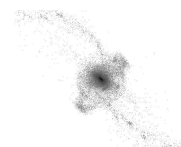
The models presented here, constraining the initial conditions of simulated encounters which match the observed morphology and kinematics of observed systems, provide a starting point to run detailed hydrodynamic simulations to test galaxy-scale star formation models. Such simulations will enable a detailed comparison of model predictions with the observed star formation properties of these merging systems, hopefully providing improved constraints on star formation models (e.g., Barnes 2004; Chien & Barnes 2010).



7.2 Tracers of Dense Gas

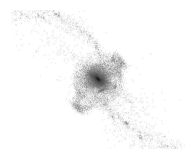
A single-dish study of the $1-0$ rotational transitions of HCN and HCO^+ was combined with mid-infrared diagnostics of the AGN strength to assess the potential influence of the radiation field resulting from the AGN. This was performed in light of claims in the literature that AGN can significantly influence molecular gas and enhance the HCN ($1-0$) emission. It was demonstrated that the ratio of HCN ($1-0$)-to-HCN ($1-0$) is not a simple function of (mid-infrared) AGN strength. Based on modeling work in the literature, it is found that elevated HCN ($1-0$)-to-HCN ($1-0$) ratios can reflect high density gas (consistent with predictions Meijerink et al. 2007) and that a high ratio doesn't uniquely trace the presence of an AGN. Further work on these line ratios (likely incorporating other molecular transitions and species) will be necessary to disentangle radiative and density effects and properly interpret these line ratios.

These observations of high n_{crit} gas tracers diagnose the conditions in the high-density gas most closely associated with star formation. These observations may also provide constraints on galaxy-scale star formation models—a successful model should reproduce the properties of the multi-phase ISM, including commonly observed tracers such as HCN and HCO^+ .

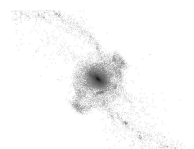


References

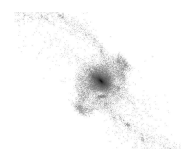
- Aalto, S., Booth, R. S., Black, J. H., & Johansson, L. E. B. 1995, *A&A*, 300, 369
- Aalto, S., Garcia-Burillo, S., Muller, S., Winters, J. M., van der Werf, P. P., Henkel, C., Costagliola, F., & Neri, R. 2012, *Astronomy & Astrophysics*, 537, A44
- Alonso-Herrero, A., Engelbracht, C. W., Rieke, M. J., Rieke, G. H., & Quillen, A. C. 2001, *ApJ*, 546, 952
- Alonso-Herrero, A., Rosales-Ortega, F. F., Sánchez, S. F., Kennicutt, R. C., Pereira-Santaella, M., & Díaz, Á. I. 2012, *MNRAS*, 425, L46
- Angulo, R. E., Springel, V., White, S. D. M., Jenkins, A., Baugh, C. M., & Frenk, C. S. 2012, *MNRAS*, 426, 2046
- Armus, L., Heckman, T., & Miley, G. 1987, *AJ*, 94, 831
- Armus, L., Mazzarella, J. M., Evans, A. S., Surace, J. A., Sanders, D. B., Iwasawa, K., Frayer, D. T., Howell, J. H., Chan, B., Petric, A., Vavilkin, T., Kim, D. C., Haan, S., Inami, H., Murphy, E. J., Appleton, P. N., Barnes, J. E., Bothun, G. D., Bridge, C. R., Charmandaris, V., Jensen, J. B., Kewley, L. J., Lord, S., Madore, B. F., Marshall, J. A., Melbourne, J. E., Rich, J. A., Satyapal, S., Schulz, B., Spoon, H. W. W., Sturm, E., U, V., Veilleux, S., & Xu, K. 2009, *PASP*, 121, 559



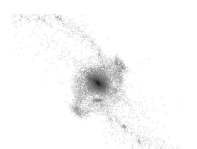
- Arp, H. 1966, *ApJS*, 14, 1
- Bahcall, J. N., Kirhakos, S., & Schneider, D. P. 1995, *ApJ*, 447, L1
- Barnes, J. E. 1988, *ApJ*, 331, 699
- Barnes, J. E. 1992, *ApJ*, 393, 484
- Barnes, J. E. 2002, *MNRAS*, 333, 481
- . 2004, *MNRAS*, 350, 798
- . 2011, *MNRAS*, 413, 2860
- Barnes, J. E. & Hernquist, L. 1996, *ApJ*, 471, 115
- Barnes, J. E. & Hernquist, L. E. 1991, *ApJ*, 370, L65
- Barnes, J. E. & Hibbard, J. E. 2009, *AJ*, 137, 3071
- Barnes, J. E. & Hut, P. 1986, *Nature*, 324, 446
- Beaton, R. L., Martinez-Delgado, D., D'Onghia, E., Zibetti, S., Gabany, R. J., Johnson, K. E., Majewski, S. R., Blanton, M., & Verbiscer, A. 2013, *ArXiv e-prints*
- Bethe, H. A. 1939, *Physical Review*, 55, 434
- Bigiel, F., Leroy, a., Walter, F., Brinks, E., de Blok, W. J. G., Madore, B., & Thornley, M. D. 2008, *AJ*, 136, 2846
- Bosma, A. 1981, *AJ*, 86, 1791
- Boylan-Kolchin, M., Springel, V., White, S. D. M., Jenkins, A., & Lemson, G. 2009, *MNRAS*, 398, 1150



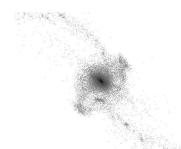
- Brandl, B. R., Bernard-Salas, J., Spoon, H. W. W., Devost, D., Sloan, G. C., Guilles, S., Wu, Y., Houck, J. R., Weedman, D. W., Armus, L., Appleton, P. N., Soifer, B. T., Charmandaris, V., Hao, L., Higdon, J. A., Marshall, S. J., & Herter, T. L. 2006, *ApJ*, 653, 1129
- Bryant, P. M. & Scoville, N. Z. 1999, *AJ*, 117, 2632
- Bushouse, H. A. 1986, *AJ*, 91, 255
- Bussmann, R. S., Dey, A., Armus, L., Brown, M. J. I., Desai, V., Gonzalez, A. H., Jannuzi, B. T., Melbourne, J., & Soifer, B. T. 2012, *ApJ*, 744, 150
- Catinella, B., Schiminovich, D., Kauffmann, G., Fabello, S., Wang, J., Hummels, C., Lemonias, J., Moran, S. M., Wu, R., Giovanelli, R., Haynes, M. P., Heckman, T. M., Basu-Zych, A. R., Blanton, M. R., Brinchmann, J., Budavári, T., Gonçalves, T., Johnson, B. D., Kennicutt, R. C., Madore, B. F., Martin, C. D., Rich, M. R., Tacconi, L. J., Thilker, D. A., Wild, V., & Wyder, T. K. 2010, *MNRAS*, 403, 683
- Chien, L.-H. 2009, PhD thesis, University of Hawai'i at Manoa
- Chien, L.-H. & Barnes, J. E. 2010, *MNRAS*, 407, 43
- Chien, L.-H., Barnes, J. E., Kewley, L. J., & Chambers, K. C. 2007, *ApJ*, 660, L105
- Cisternas, M., Jahnke, K., Inskip, K. J., Kartaltepe, J., Koekemoer, A. M., Lisker, T., Robaina, A. R., Scodreggio, M., Sheth, K., Trump, J. R., Andrae, R. R., Miyaji, T., Lusso, E., Brusa, M., Capak, P., Cappelluti, N., Civano, F., Ilbert, O., Impey, C. D., Leauthaud, A., Lilly, S. J., Salvato, M., Scoville, N. Z., & Taniguchi, Y. 2010, *ApJ*, 726, 57



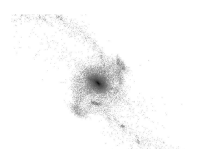
- Condon, J. J., Cotton, W. D., Greisen, E. W., Yin, Q. F., Perley, R. A., Taylor, G. B., & Broderick, J. J. 1998, *AJ*, 115, 1693
- Costagliola, F., Aalto, S., Rodriguez, M. I., Muller, S., Spoon, H. W. W., Martín, S., Pérez-Torres, M. A., Alberdi, A., Lindberg, J. E., Batejat, F., Jütte, E., van Der Werf, P., & Lahuis, F. 2011, *Astronomy & Astrophysics*
- Cowie, L. L., Barger, A. J., Fomalont, E. B., & Capak, P. 2004, *ApJ*, 603, L69
- Davies, R. I., Mark, D., & Sternberg, A. 2012, *Astronomy & Astrophysics*, 537, A133
- de Grijs, R., Lee, J. T., Mora Herrera, M. C., Fritze-v. Alvensleben, U., & Anders, P. 2003, *New Astronomy*, 8, 155
- de Vaucouleurs, G., de Vaucouleurs, A., Corwin, Jr., H. G., Buta, R. J., Paturel, G., & Fouqué, P. 1991, *Third Reference Catalogue of Bright Galaxies. Volume I: Explanations and references. Volume II: Data for galaxies between 0^h and 12^h. Volume III: Data for galaxies between 12^h and 24^h.*
- Di Matteo, T., Springel, V., & Hernquist, L. 2005, *Nature*, 433, 604
- D'Onghia, E., Vogelsberger, M., Faucher-Giguere, C. A., & Hernquist, L. 2010, *ApJ*, 725, 353
- Draper, A. R. & Ballantyne, D. R. 2012, *ApJ*, 753, L37
- Dubinski, J., Mihos, J. C., & Hernquist, L. 1996, *ApJ*, 462, 576
- Duc, P.-A., Cuillandre, J.-C., Alatalo, K., Blitz, L., Bois, M., Bournaud, F., Bureau, M., Cappellari, M., Côté, P., Davies, R. L., Davis, T. A., de Zeeuw, P. T., Emsellem, E., Ferrarese, L., Ferriere, E., Gwyn, S., Khochfar, S., Krajnovic, D., Kuntschner, H., Lablanche, P.-Y., McDermid, R. M., Michel-Dansac, L., Morganti, R., Naab,



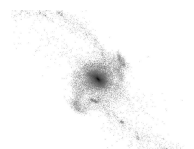
- T., Oosterloo, T., Sarzi, M., Scott, N., Serra, P., Weijmans, A., & Young, L. M. 2013, in IAU Symposium, Vol. 295, IAU Symposium, ed. D. Thomas, A. Pasquali, & I. Ferreras, 358–361
- Duncan, J. C. 1923, ApJ, 57, 137
- Elbaz, D., Dickinson, M., Hwang, H. S., Díaz-Santos, T., Magdis, G., Magnelli, B., Le Borgne, D., Galliano, F., Pannella, M., Chanial, P., Armus, L., Charmandaris, V., Daddi, E., Aussel, H., Popesso, P., Kartaltepe, J., Altieri, B., Valtchanov, I., Coia, D., Dannerbauer, H., Dasyra, K., Leiton, R., Mazzarella, J., Alexander, D. M., Buat, V., Burgarella, D., Chary, R.-R., Gilli, R., Ivison, R. J., Juneau, S., Le Floc'h, E., Lutz, D., Morrison, G. E., Mullaney, J. R., Murphy, E., Pope, A., Scott, D., Brodwin, M., Calzetti, D., Cesarsky, C., Charlot, S., Dole, H., Eisenhardt, P., Ferguson, H. C., Förster Schreiber, N., Frayer, D., Giavalisco, M., Huynh, M., Koekemoer, A. M., Papovich, C., Reddy, N., Surace, C., Teplitz, H., Yun, M. S., & Wilson, G. 2011, A&A, 533, A119
- Ellison, S. L., Patton, D. R., Simard, L., McConnachie, A. W., Baldry, I. K., & Mendel, J. T. 2010, MNRAS, 407, 1514
- Engel, H., Tacconi, L. J., Davies, R. I., Neri, R., Smail, I., Chapman, S. C., Genzel, R., Cox, P., Greve, T. R., Ivison, R. J., Blain, A. W., Bertoldi, F., & Omont, A. 2010, ApJ, 724, 233
- English, J., Norris, R. P., Freeman, K. C., & Booth, R. S. 2003, AJ, 125, 1134
- Evans, A. S., Solomon, P. M., Tacconi, L. J., Vavilkin, T., & Downes, D. 2006, AJ, 132, 2398



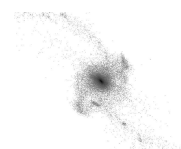
- Evans, A. S., Vavilkin, T., Pizagno, J., Modica, F., Mazzarella, J. M., Iwasawa, K., Howell, J. H., Surace, J. A., Armus, L., Petric, A. O., Spoon, H. W. W., Barnes, J. E., Suer, T. A., Sanders, D. B., Chan, B., & Lord, S. 2008, *ApJ*, 675, L69
- Fernández, X., van Gorkom, J. H., Schweizer, F., & Barnes, J. E. 2010, *AJ*, 140, 1965
- Ferrarese, L. & Merritt, D. 2000, *ApJ*, 539, L9
- Gao, Y. & Solomon, P. M. 2004, *ApJS*, 152, 63
- Gebhardt, K., Bender, R., Bower, G., Dressler, A., Faber, S. M., Filippenko, A. V., Green, R., Grillmair, C., Ho, L. C., Kormendy, J., Lauer, T. R., Magorrian, J., Pinkney, J., Richstone, D., & Tremaine, S. 2000, *ApJ*, 539, L13
- Gerssen, J., van der Marel, R. P., Axon, D. J., Mihos, J. C., Hernquist, L., & Barnes, J. E. 2004, *AJ*, 127, 75
- Gilbert, S. J. & Sellwood, J. A. 1994, in *Numerical Simulations in Astrophysics*, 131–143
- González-Alfonso, E., Fischer, J., Graciá-Carpio, J., Falstad, N., Sturm, E., Meléndez, M., Spoon, H. W. W., Verma, A., Davies, R. I., Lutz, D., Aalto, S., Polisensky, E., Poglitsch, A., Veilleux, S., & Contursi, A. 2014, *A&A*, 561, A27
- Graciá-Carpio, J., García-Burillo, S., Planesas, P., & Colina, L. 2006, *ApJ*, 640, L135
- Gültekin, K., Richstone, D. O., Gebhardt, K., Lauer, T. R., Tremaine, S., Aller, M. C., Bender, R., Dressler, A., Faber, S. M., Filippenko, A. V., Green, R., Ho, L. C., Kormendy, J., Magorrian, J., Pinkney, J., & Siopis, C. 2009, *ApJ*, 698, 198
- Haan, S., Surace, J. A., Armus, L., Evans, A. S., Howell, J. H., Mazzarella, J. M., Kim, D. C., Vavilkin, T., Inami, H., Sanders, D. B., Petric, A., Bridge, C. R., Melbourne,



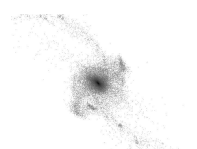
- J. L., Charmandaris, V., Díaz-Santos, T., Murphy, E. J., U, V., Stierwalt, S., & Marshall, J. A. 2011, *AJ*, 141, 100
- Haehnelt, M. G., Natarajan, P., & Rees, M. J. 1998, *MNRAS*, 300, 817
- Hernquist, L. 1989, *Nature*, 340, 687
- Hernquist, L. 1990, *ApJ*, 356, 359
- Hibbard, J. E. & Mihos, J. C. 1995, *AJ*, 110, 140
- Hibbard, J. E., van der Hulst, J. M., Barnes, J. E., & Rich, R. M. 2001, *AJ*, 122, 2969
- Hibbard, J. E. & van Gorkom, J. H. 1996, *AJ*, 111, 655
- Hibbard, J. E. & Yun, M. S. 1996, in *Cold Gas at High Redshift, Proceedings of a workshop celebrating the 25th anniversary of the Westerbork Synthesis Radio Telescope*, ed. M. Bremer & N. Malcolm (Dordrecht: Kluwer Academic Publishers), 47
- Hibbard, J. E. & Yun, M. S. 1999, *AJ*, 118, 162
- Hill, M. J. & Zakamska, N. L. 2014, *MNRAS*, 439, 2701
- Hopkins, P. F., Cox, T. J., Hernquist, L., Narayanan, D., Hayward, C. C., & Murray, N. 2013a, *MNRAS*, 430, 1901
- Hopkins, P. F., Hayward, C. C., Narayanan, D., & Hernquist, L. 2011a, *MNRAS*, no
- Hopkins, P. F., Hernquist, L., Cox, T. J., & Kereš, D. 2008, *ApJS*, 175, 356
- Hopkins, P. F., Narayanan, D., & Murray, N. 2013b, *MNRAS*, 432, 2647



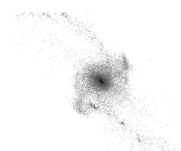
- Hopkins, P. F. & Quataert, E. 2010, *Distribution*, 000, 5
- Hopkins, P. F., Quataert, E., & Murray, N. 2011b, *MNRAS*, 417, 950
- Howell, J. H., Armus, L., Mazzarella, J. M., Evans, A. S., Surace, J. A., Sanders, D. B., Petric, A., Appleton, P. N., Bothun, G. D., Bridge, C., Chan, B. H. P., Charmandaris, V., Frayer, D. T., Haan, S., Inami, H., Kim, D.-C., Lord, S., Madore, B. F., Melbourne, J., Schulz, B., U, V., Vavilkin, T., Veilleux, S., & Xu, K. 2010, *ApJ*, 715, 572
- Imanishi, M. & Nakanishi, K. 2006, *PASJ*, 58, 813
- . 2013, *AJ*, 146, 91
- . 2014, ArXiv e-prints
- Imanishi, M., Nakanishi, K., & Kohno, K. 2006, *AJ*, 131, 2888
- Imanishi, M., Nakanishi, K., Tamura, Y., Oi, N., & Kohno, K. 2007, *AJ*, 134, 2366
- Imanishi, M., Nakanishi, K., Tamura, Y., & Peng, C.-H. 2009, *AJ*, 137, 3581
- Inami, H., Armus, L., Charmandaris, V., Groves, B., Kewley, L., Petric, A., Stierwalt, S., Daz-Santos, T., Surace, J., Rich, J., Haan, S., Howell, J., Evans, A. S., Mazzarella, J., Marshall, J., Appleton, P., Lord, S., Spoon, H., Frayer, D., Matsuhara, H., & Veilleux, S. 2013, *The Astrophysical Journal*, 777, 156
- Iono, D., Yun, M. S., & Ho, P. T. P. 2005, *ApJS*, 158, 1
- Iwasawa, K., Mazzarella, J. M., Surace, J. A., Sanders, D. B., Armus, L., Evans, A. S., Howell, J. H., Komossa, S., Petric, A. O., Teng, S. H., U, V., & Veilleux, S. 2011, *Astronomy & Astrophysics*, 528, A137



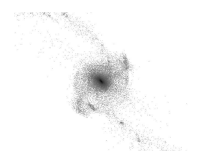
- Iwasawa, K., Sanders, D. B., Evans, A. S., Mazzarella, J. M., Armus, L., & Surace, J. A. 2009, *ApJ*, 695, L103
- Karl, S. J., Lunttila, T., Naab, T., Johansson, P. H., Klaas, U., & Juvela, M. 2013, ArXiv e-prints
- Karl, S. J., Naab, T., Johansson, P. H., Kotarba, H., Boily, C. M., Renaud, F., & Theis, C. 2010, *ApJ*, 715, L88
- Kaviraj, S. 2014, *MNRAS*, 440, 2944
- Kennicutt, R. C. 1998, *ARA&A*, 36, 189
- Keto, E., Ball, R., Arens, J., Jernigan, G., & Meixner, M. 1992, *ApJ*, 389, 223
- Kim, D.-C., Evans, A. S., Vavilkin, T., Armus, L., Mazzarella, J. M., Sheth, K., Surace, J. A., Haan, S., Howell, J. H., Díaz-Santos, T., Petric, A., Iwasawa, K., Privon, G. C., & Sanders, D. B. 2013, *ApJ*, 768, 102
- Kim, D.-C., Sanders, D. B., Veilleux, S., Mazzarella, J. M., & Soifer, B. T. 1995, *ApJS*, 98, 129
- Knierman, K., Knezek, P. M., Scowen, P., Jansen, R. A., & Wehner, E. 2012, *ApJ*, 749, L1
- Kohno, K., Ishizuki, S., Matsushita, S., Vila-Vilaró, B., & Kawabe, R. 2003, *PASJ*, 55, L1
- Kormendy, J. & Sanders, D. B. 1992, *ApJ*, 390, L53
- Laine, S., van der Marel, R. P., Rossa, J., Hibbard, J. E., Mihos, J. C., Bker, T., & Zabludoff, A. I. 2003, *AJ*, 126, 2717



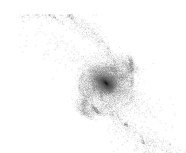
- Lepp, S. & Dalgarno, A. 1996, *A&A*, 306, L21
- Leroy, A. K., Bigiel, F., de Blok, W. J. G., Boissier, S., Bolatto, A., Brinks, E., Madore, B., Munoz-Mateos, J.-C., Murphy, E., Sandstrom, K., Schruba, A., & Walter, F. 2012, *AJ*, 144, 3
- Lonsdale, C. J., Smith, H. J., & Lonsdale, C. J. 1993, *ApJ*, 405, L9
- Lotz, J. M., Jonsson, P., Cox, T. J., Croton, D., Primack, J. R., Somerville, R. S., & Stewart, K. 2011, *ApJ*, 742, 103
- Mahoney, J. M., Burke, B. F., & van der Hulst, J. M. 1987, in *Dark Matter in the Universe. Proceedings of the 117th. Symposium of the International Astronomical Union*, ed. J. K. G. Knapp (Princeton, New Jersey, U.S.A.: D. Reidel Publishing Company, Dordrecht, Holland), 94
- Maiolino, R., Comastri, A., Gilli, R., Nagar, N. M., Bianchi, S., Boker, T., Colbert, E., Krabbe, A., Marconi, A., Matt, G., & Salvati, M. 2003, *MNRAS*, 344, L59
- Martinsson, T. P. K., Verheijen, M. A. W., Westfall, K. B., Bershadsky, M. A., Andersen, D. R., & Swaters, R. A. 2013, *A&A*, 557, A131
- Mazzarella, J. M., Iwasawa, K., Vavilkin, T., Armus, L., Kim, D.-C., Bothun, G., Evans, A. S., Spoon, H. W. W., Haan, S., Howell, J. H., Lord, S., Marshall, J. A., Ishida, C. M., Xu, C. K., Petric, A., Sanders, D. B., Surace, J. A., Appleton, P., Chan, B. H. P., Frayer, D. T., Inami, H., Khachikian, E. Y., Madore, B. F., Privon, G. C., Sturm, E., U, V., & Veilleux, S. 2012, *AJ*, 144, 125
- McLean, B. J., Greene, G. R., Lattanzi, M. G., & Pirenne, B. 2000, in *Astronomical Society of the Pacific Conference Series, Vol. 216, Astronomical Data Analysis Software and Systems IX*, ed. N. Manset, C. Veillet, & D. Crabtree, 145



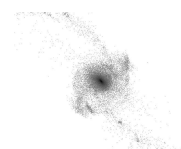
- McMullin, J. P., Waters, B., Schiebel, D., Young, W., & Golap, K. 2007, in *Astronomical Society of the Pacific Conference Series*, Vol. 376, *Astronomical Data Analysis Software and Systems XVI*, ed. R. A. Shaw, F. Hill, & D. J. Bell, 127
- Meijerink, R., Spaans, M., & Israel, F. P. 2007, *A&A*, 461, 793
- Mihos, J. C. 2001, *ApJ*, 550, 94
- Mihos, J. C., Bothun, G. D., & Richstone, D. O. 1993, *ApJ*, 418, 82
- Mihos, J. C. & Hernquist, L. 1994a, *ApJ*, 425, L13
- . 1994b, *ApJ*, 431, L9
- Mihos, J. C., Richstone, D. O., & Bothun, G. D. 1992, *ApJ*, 400, 153
- Mirabel, I. F., Vigroux, L., Charmandaris, V., Sauvage, M., Gallais, P., Tran, D., Cesarsky, C., Madden, S. C., & Duc, P.-A. 1998, *A&A*, 333, L1
- Miralles-Caballero, D., Díaz, A. I., Rosales-Ortega, F. F., Pérez-Montero, E., & Sánchez, S. F. 2014, *MNRAS*, 440, 2265
- Mould, J. R., Huchra, J. P., Freedman, W. L., Kennicutt, Jr., R. C., Ferrarese, L., Ford, H. C., Gibson, B. K., Graham, J. A., Hughes, S. M. G., Illingworth, G. D., Kelson, D. D., Macri, L. M., Madore, B. F., Sakai, S., Sebo, K. M., Silbermann, N. A., & Stetson, P. B. 2000, *ApJ*, 529, 786
- Naab, T., Johansson, P. H., & Ostriker, J. P. 2009, *ApJ*, 699, L178
- Naab, T. & Trujillo, I. 2006, *MNRAS*, 369, 625
- Navarro, J. F., Frenk, C. S., & White, S. D. M. 1996, *ApJ*, 462, 563



- Neff, S. G., Hutchings, J. B., Standord, S. A., & Unger, S. W. 1990, *AJ*, 99, 1088
- Nelan, J. E., Smith, R. J., Hudson, M. J., Wegner, G. A., Lucey, J. R., Moore, S. A. W., Quinney, S. J., & Suntzeff, N. B. 2005, *ApJ*, 632, 137
- Neugebauer, G., Habing, H. J., van Duinen, R., Aumann, H. H., Baud, B., Beichman, C. A., Beintema, D. A., Boggess, N., Clegg, P. E., de Jong, T., Emerson, J. P., Gautier, T. N., Gillett, F. C., Harris, S., Hauser, M. G., Houck, J. R., Jennings, R. E., Low, F. J., Marsden, P. L., Miley, G., Olton, F. M., Pottasch, S. R., Raimond, E., Rowan-Robinson, M., Soifer, B. T., Walker, R. G., Wesselius, P. R., & Young, E. 1984, *ApJ*, 278, L1
- Noordam, J. E. 2004, in *Society of Photo-Optical Instrumentation Engineers (SPIE) Conference Series*, Vol. 5489, *Ground-based Telescopes*, ed. J. M. Oschmann, Jr., 817–825
- Norris, R. P. & Forbes, D. A. 1995, *ApJ*, 446, 594
- Petric, A. O., Armus, L., Howell, J., Chan, B., Mazzarella, J. M., Evans, A. S., Surace, J. A., Sanders, D., Appleton, P. N., Charmandaris, V., Díaz-Santos, T., Frayer, D. T., Haan, S., Inami, H., Iwasawa, K., Kim, D., Madore, B., Marshall, J., Spoon, H., Stierwalt, S., Sturm, E., U, V., Vavilkin, T., Veilleux, S., Santos, T. D., & Lord, S. 2011, *ApJ*, 730, 28
- Privon, G. C., Barnes, J. E., Evans, A. S., Hibbard, J. E., Yun, M. S., Mazzarella, J. M., Armus, L., & Surace, J. 2013, *ApJ*, 771, 120
- Roberts, M. S. 1976, *Comments on Astrophysics*, 6, 105
- Roberts, M. S. & Haynes, M. P. 1994, *ARA&A*, 32, 115



- Rossa, J., Laine, S., van der Marel, R. P., Mihos, J. C., Hibbard, J. E., Böker, T., & Zabludoff, A. I. 2007, *AJ*, 134, 2124
- Rothberg, B. & Joseph, R. D. 2006, *AJ*, 132, 976
- Rothberg, B., Whitmore, B., Schweizer, F., Chandar, R., van der Marel, R. P., Rossa, J., Blair, W. P., Mengel, S., & Rieke, M. 2007, *Proceedings of the International Astronomical Union*, 2, 240
- Rubin, V. C., Thonnard, N., & Ford, Jr., W. K. 1978, *ApJ*, 225, L107
- Rupke, D. S. N. & Veilleux, S. 2011, *ApJ*, 729, L27
- . 2013, *ApJ*, 768, 75
- Sanders, D. B., Mazzarella, J. M., Kim, D.-C., Surace, J. A., & Soifer, B. T. 2003, *AJ*, 126, 1607
- Sanders, D. B. & Mirabel, I. F. 1985, *ApJ*, 298, L31
- . 1996, *ARA&A*, 34, 749
- Sanders, D. B., Soifer, B. T., Elias, J. H., Madore, B. F., Matthews, K., Neugebauer, G., & Scoville, N. Z. 1988, *ApJ*, 325, 74
- Schmidt, M. 1959, *ApJ*, 129, 243
- Schweizer, F. 1982, *ApJ*, 252, 455
- Schweizer, F. & Seitzer, P. 2007, *AJ*, 133, 2132
- Silk, J. & Rees, M. J. 1998, *A&A*, 331, L1



Skrutskie, M. F., Cutri, R. M., Stiening, R., Weinberg, M. D., Schneider, S., Carpenter, J. M., Beichman, C., Capps, R., Chester, T., Elias, J., Huchra, J., Liebert, J., Lonsdale, C., Monet, D. G., Price, S., Seitzer, P., Jarrett, T., Kirkpatrick, J. D., Gizis, J. E., Howard, E., Evans, T., Fowler, J., Fullmer, L., Hurt, R., Light, R., Kopan, E. L., Marsh, K. A., McCallon, H. L., Tam, R., Van Dyk, S., & Wheelock, S. 2006, *AJ*, 131, 1163

Soifer, B. T., Sanders, D. B., Neugebauer, G., Danielson, G. E., Lonsdale, C. J., Madore, B. F., & Persson, S. E. 1986, *ApJ*, 303, L41

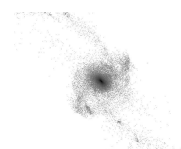
Sotnikova, N. Y. & Reshetnikov, V. P. 1998, *Astronomy Letters*, 24, 73

Spergel, D. N., Bean, R., Doré, O., Nolta, M. R., Bennett, C. L., Dunkley, J., Hinshaw, G., Jarosik, N., Komatsu, E., Page, L., Peiris, H. V., Verde, L., Halpern, M., Hill, R. S., Kogut, A., Limon, M., Meyer, S. S., Odegard, N., Tucker, G. S., Weiland, J. L., Wollack, E., & Wright, E. L. 2007, *ApJS*, 170, 377

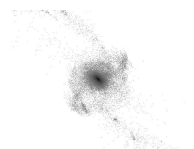
Spergel, D. N., Verde, L., Peiris, H. V., Komatsu, E., Nolta, M. R., Bennett, C. L., Halpern, M., Hinshaw, G., Jarosik, N., Kogut, A., Limon, M., Meyer, S. S., Page, L., Tucker, G. S., Weiland, J. L., Wollack, E., & Wright, E. L. 2003, *ApJS*, 148, 175

Springel, V., Di Matteo, T., & Hernquist, L. 2005, *MNRAS*, 361, 776

Stierwalt, S., Armus, L., Surace, J. A., Inami, H., Petric, A. O., Díaz-Santos, T., Haan, S., Charmandaris, V., Howell, J., Kim, D. C., Marshall, J., Mazzarella, J. M., Spoon, H. W. W., Veilleux, S., Evans, A. S., Sanders, D. B., Appleton, P. N., Bothun, G. D., Bridge, C. R., Chan, B., Frayer, D. T., Iwasawa, K., Kewley,



- L. J., Lord, S., Madore, B. F., Melbourne, J. E., Murphy, E. J., Rich, J. A., Schulz, B., Sturm, E., U, V., Vavilkin, T., & Xu, K. 2013, *ApJ*, 206, 1
- Stockton, A. 1974, *ApJ*, 187, 219
- Taylor, G. B., Carilli, C. L., & Perley, R. A., eds. 1999, *Astronomical Society of the Pacific Conference Series*, Vol. 180, *Synthesis Imaging in Radio Astronomy II*
- Tinney, C. G., Scoville, N. Z., Sanders, D. B., & Soifer, B. T. 1990, *ApJ*, 362, 473
- Toomre, A. 1977, *ARA&A*, 15, 437
- Toomre, A. & Toomre, J. 1972, *ApJ*, 178, 623
- Treister, E., Schawinski, K., Urry, C. M., & Simmons, B. D. 2012, *ApJ*, 758, L39
- U, V., Medling, A., Sanders, D., Max, C., Armus, L., Iwasawa, K., Evans, A., Kewley, L., & Fazio, G. 2013, *ApJ*, 775, 115
- U, V., Sanders, D. B., Mazzarella, J. M., Evans, A. S., Howell, J. H., Surace, J. A., Armus, L., Iwasawa, K., Kim, D.-C., Casey, C. M., Vavilkin, T., Dufault, M., Larson, K. L., Barnes, J. E., Chan, B. H. P., Frayer, D. T., Haan, S., Inami, H., Ishida, C. M., Kartaltepe, J. S., Melbourne, J. L., & Petric, A. O. 2012, *ApJS*, 203, 9
- Väisänen, P., Rajpaul, V., Zijlstra, A. A., Reunanen, J., & Kotilainen, J. 2012, *MNRAS*, 420, 2209
- van der Hulst, J. M. 1979, *A&A*, 71, 131
- Vorontsov-Vel'iaminov, B. A. 1958, *Soviet Astronomy*, 2, 805



- Westmoquette, M. S., Clements, D. L., Bendo, G. J., & Khan, S. A. 2012, *MNRAS*, 424, 416
- Wilson, C. D., Scoville, N., Madden, S. C., & Charmandaris, V. 2000, *ApJ*, 542, 120
- Xu, C., Gao, Y., Mazzarella, J., Lu, N., Sulentic, J. W., & Domingue, D. L. 2000, *ApJ*, 541, 644
- Xu, C. K., Domingue, D., Cheng, Y.-W., Lu, N., Huang, J., Gao, Y., Mazzarella, J. M., Cutri, R., Sun, W.-H., & Surace, J. A. 2010, *ApJ*, 713, 73
- Yun, M. S., Ho, P. T. P., & Lo, K. Y. 1994, *Nature*, 372, 530

